Vehicle Safety Institute

Thomas Kobald, BSc

Predicting Boundary Conditions for Occupant Simulation Models under Lateral Loading using Real-World Accident Data

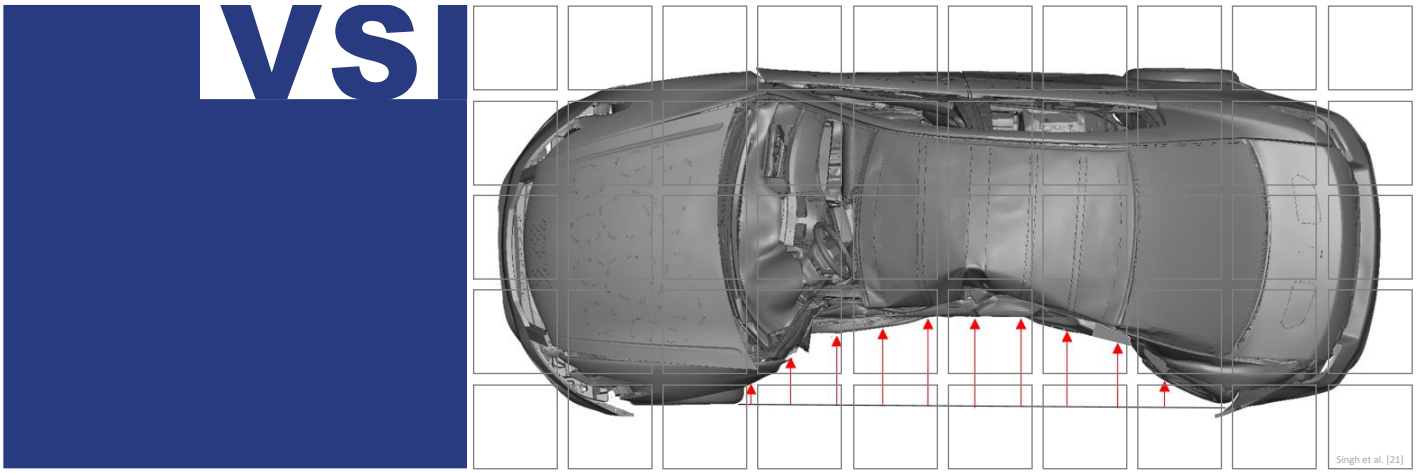

MASTER'S THESIS to achieve the university degree of

Master of Science

Master's Degree Program:

Mechanical Engineering and Business Economics

Submitted to

Graz University of Technology

Supervisor:	Assoc.Prof. Dipl.-Ing. Dr.techn. Wolfgang Sinz
Co-Supervisor:	Dipl.-Ing. Stefan Smit, BSc
Head of Institute:	Univ.-Prof. Dipl.-Ing. Dr.techn. Hermann Steffan

Vehicle Safety Institute

Graz, March 2021

AFFIDATIV

I declare that I have authored this thesis independently, that I have not used other than the declared sources/resources, and that I have explicitly marked all material which has been quoted either literally or by content from the used sources. The text document uploaded to TUGRAZonline is identical to the present master thesis.

Graz, _____ _____

Signature

ABSTRACT

The complement of vehicle crash tests with increasingly detailed simulation models increases the demand for computational resources, particularly when several iterations are performed. Meta-models have become a popular approach to deal with this issue. Hence, this technique was used in this thesis to predict the boundary conditions (lateral door intrusion, velocity) for an occupant simulation model for lateral load cases. The door intrusion was approximated by intruding rigid planes. By varying the input parameters of a full vehicle Finite Element Analysis (FEA) model, training points for meta-modeling were gathered. Three different training sets were used to analyze the influences of the number of training points and their distribution within the experimental space on prediction quality. A fourth-order polynomial was used to approximate intrusion and velocity curves. Therefore, five boundary conditions representing the meta-models' output parameters were chosen.

Five meta-model types (GPML, Kriging, LSSVM, Rational, RBF) were fitted by applying a Genetic Algorithm. The best-performing model was selected using a validation set. The RBF model performed best, followed closely by GPML and LSSVM, while Kriging and Rational models did not perform well. The RBF models' prediction quality was assessed by comparing it to the FEA result. The NRMSE (Normalized Root Mean Square Error, one is a perfect fit) of the prediction was calculated. Average NRMSE was 0.518, 0.620, and 0.583 for the different training sets. The prediction showed a high dependency on impact angle and impact position. The best prediction (NRMSE=0.910) was achieved for an impact angle and impact position close to their nominal value. Impact velocity and weight ratio were less sensitive and did not impair prediction quality. Overall, prediction quality was not satisfying since the intrusion in lateral impacts depends on various parameters, like material properties, wall thicknesses, etcetera.

TABLE OF CONTENTS

LIST OF FIGURES

LIST OF TABLES

LIST OF EQUATIONS

1 INTRODUCTION

According to the World Health Organization, the leading cause of death in Europe are diseases of the circulatory system (44%), followed by malignant neoplasms (21%) and external causes (7%). The external causes can be subdivided as shown in Figure 1-1. While suicide is the leading cause in this category, traffic accidents are the second most frequent external cause of death. The frequency of fatal traffic accidents has constantly decreased since 2000. Yet since 2012, the number is almost stagnating. [1]

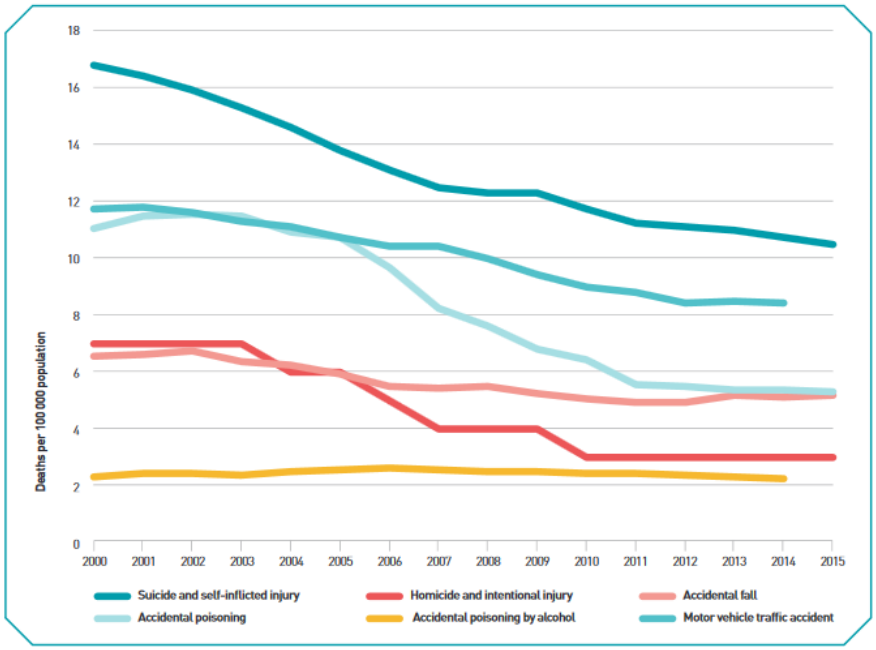

Figure 1-1 External causes of death per 100 000 inhabitants in Europe. [1]

From 2010 to 2019 different countermeasures resulted in reducing road fatalities in the EU (European Union) by 23.66%. However, the European Commission's target to halve the number of road fatalities from 2010 to 2020 is unlikely to be met. For the next period, from 2020 to 2030, the medium-term targets are to halve the number of road fatalities as well as the number of people seriously injured in traffic accidents. The long-term target (*Vision Zero*) is to have no deaths and no seriously injured people on European roads by 2050. [2]

1.1 Side Crash

In 2013, car occupants accounted for 45% of all fatally injured road users in the EU [3]. Thomas et al. analyzed data from IGLAD (Initiative for the global harmonization of accident data) and found that for car occupants suffering from severe injuries, the most common crash opponent was another car (34% to 45%). These car-to-car crashes are mainly frontal impacts (61% to 69%), followed by side impacts (22% to 29%). [4]

Similar distributions are observed for the United States of America (US). Analyzing data from NASS CDS (National Automotive Sampling System Crashworthiness Data System, case years 2001-2015) indicates that vehicle damage resulting from the most harmful accident event most frequently occurs at the front (55%), followed by the left (14%) and right (11%) side of the vehicle. A smaller share of vehicles is damaged at the rear (10%) and other locations (10%, including 'top' and 'other', Figure 1-2). [5]

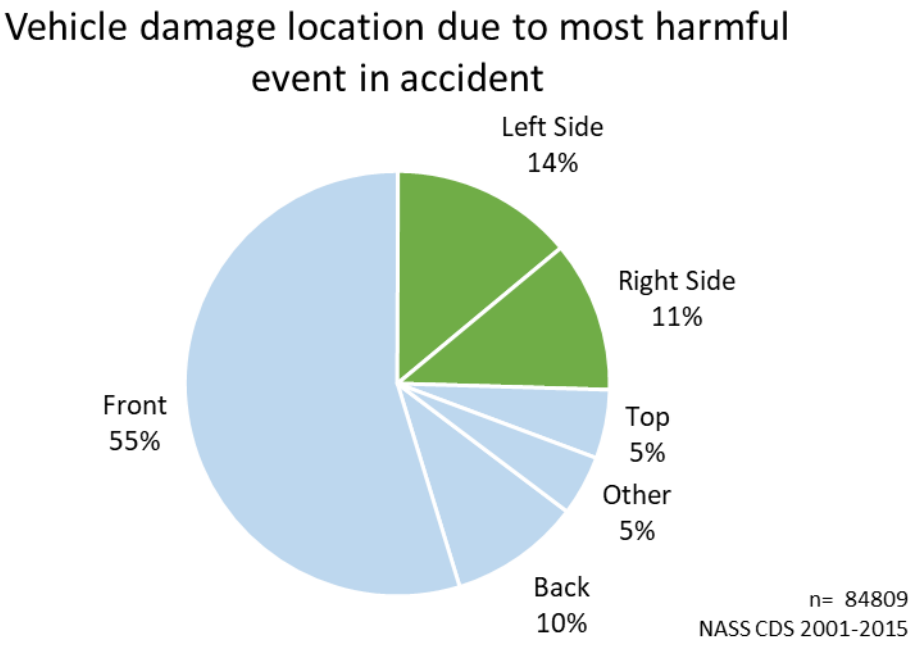

Figure 1-2 Composition of the vehicle damage location due to most harmful event in accidents in the US.

Figure 1-3 shows the Injury Severity Score (ISS, classified according to Stevenson et al. [6]) versus the vehicle's main damage location. For lower ISS scores (0-15), the share of occupants involved in side-crashes corresponds to the share of vehicles damaged at the side from Figure 1-2. However, side crashes are overrepresented if occupants suffer from severe (35.2%) and critical (40.6%) injuries. Therefore, a higher risk of sustaining a severe or critical injury in side-crashes is observed compared to other crash modes (e.g., frontal crash). Hence, improving safety measures for side crashes are required to meet the EC's midterm and long-term targets.

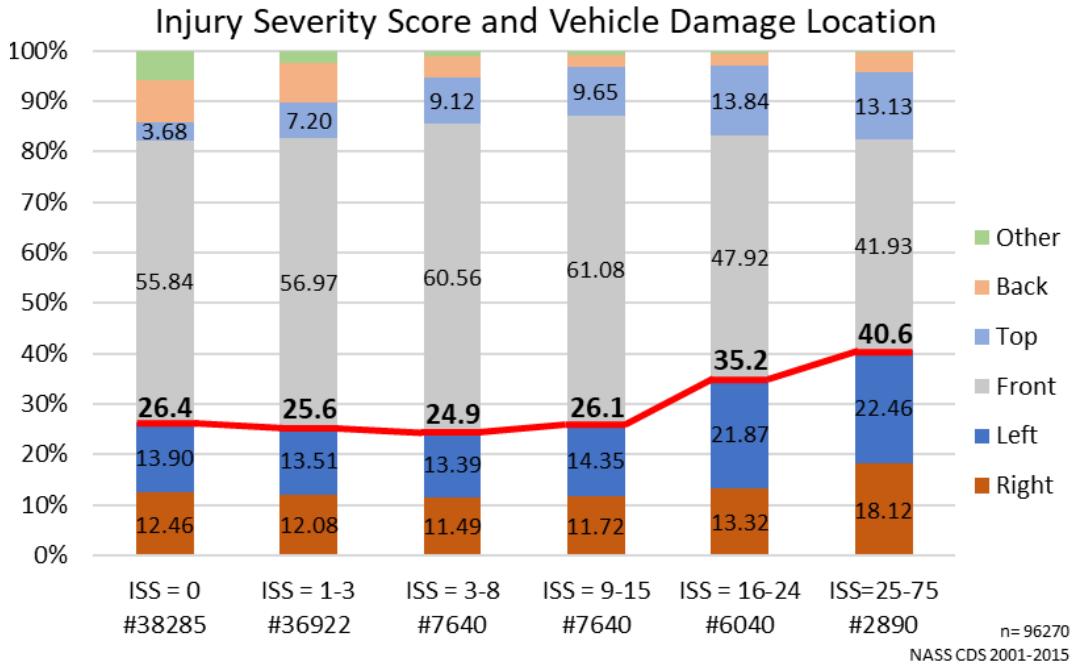

Figure 1-3 Distribution of the ISS for occupants categorized with the vehicle damage location due to most harmful event in accident.

Using detailed simulation models is popular among vehicle safety development, yet they tend to be computationally expensive. The use of occupant simulation models can decrease this effort. They are already used for some accident types [7]. In frontal crashes, occupant simulation models have already shown their potential to contribute towards improving occupant safety [8, 9]. Also, side-crashes occupant simulation models have been developed and assessed [10]. As injuries in side-crash are frequently related to the intruding vehicle structure (door, B-pillar) [11], it is crucial to derive valid intrusion and acceleration input for occupant models simulating lateral impacts.

2 STATE OF THE ART

Most commonly, the passive safety of vehicles is assessed using crash tests (e.g., Euro NCAP) or simulation methods. Standard crash test configurations and their relation to Real-World accidents are discussed in the following section. Additionally, simulation methods are described.

2.1.1 **Real Crash Test**

Various crash tests evaluate the passive safety of vehicles. So-called consumer tests should give an overview of different vehicles' safety performance by deriving a simple rating, which can be considered by the consumer when purchasing a new vehicle. These tests are different in different geographic areas (e.g., US, EU). As an example, one test type from two different assessment programs are briefly discussed in this thesis: The Insurance Institute for Highway Safety (IIHS), which carries out assessments for vehicles in the US, and the European New Car Assessment Programme (Euro NCAP), which carries out reviews of vehicles sold in the EU. Here two different side impact tests with a Movable Deformable Barrier (MDB) are compared against each other. Their main parameters are listed in Table 1. Both the Euro NCAP MDB and the IIHS MDB got updated recently. The MDB position is defined relative to the struck vehicles' front axle, called the Impact Reference Distance (IRD). For the IIHS test, the IRD depends on the struck vehicles' wheelbase. The IRD for the Euro NCAP Side impact MDB is measured relative to the R-Point, a point relative to some part of the vehicle structure which the manufacturer provides. Another difference between the two MDBs is their shape. While the IIHS MDB 2.0 is based on the US vehicle fleet, the Euro NCAP MDB is based on the vehicle fleet in the EU. [12, 13]

Table 1 Boundary conditions for the IIHS MDB 2.0 and the Euro NCAP Side impact MDB.

	IIHS MDB 2.0 [13]	Euro NCAP MDB 2020 [12]
Impact Velocity [kph]	60	60
Mass [kg]	1900	1400
Impact Reference Distance (IRD) [mm]	wheelbase/2 + 198*	R-Point** + 250
Impact Angle	perpendicular	perpendicular

* for vehicles with wheelbase between 2500-2900 mm; if wheelbase > 2900 then IRD = 1648 mm; if wheelbase < 2500 then IRD = 1448 mm. Relative to front axe. PoI is measured relative to front axle (to rear).

** the R-Point is provided by the manufacturer.

As these tests can influence consumers' purchasing decisions, an excellent passive safety performance for this crash configuration is mandatory for OEMs (Original Equipment Manufacturers). However, it is not well understood how vehicles with a good rating in those tests will perform in various Real-World crash scenarios. Arbelaez et al. analyzed side crash accidents recorded in the NASS CDS from 1998 to 2003. They found out that 30% to 55% of side crashes with seriously injured near-side occupants (MAIS3+) and 10% to 25% of the crashes with fatally injured near-side occupants were less severe than the previously used IIHS MDB 1.0 side impact test, although this test was less severe (impact velocity 50 kph, weight 1500kg) than the current version of the test (v2.0). The MAIS (Maximum Abbreviated Injury Scale) is the maximum score of the AIS (Abbreviated Injury Scale) of all injuries a person sustained in a crash. MAIS3+ indicates that the occupant has suffered at least one injury ranked AIS three or higher [14]. Bareiss and Gabler evaluated the injury risk for near-side occupants of best-performing vehicles. Therefore, the rating of the US New Car Assessment Program (US NCAP) side impact test was compared against side crashes with MAIS2+ injured near-side occupants, recorded in the NASS CDS for the years 2010 to 2015. Correlations between injury risk and the US NCAP MDB performance, the delta-v, the occupant age, sex, and BMI were found. [15] Notable is that higher injury rates can be expected for sideswipes in the opposite direction than for sideswipes in the same direction. Furthermore, the initial point of impact relative to the occupant seating position influences the injury severity. [16]

Notable is that higher injury rates can be expected for sideswipes in the opposite direction than for sideswipes in the same direction. Furthermore, the initial point of impact relative to the occupant seating position influences the injury severity. [16]

2.1.2 **Crash Simulation**

Crash simulations are a good tool to supplement real crash tests. Furthermore, they enable passive safety vehicle development and testing in an early design phase while being cheap and fast, compared to physical crash tests [17]. For Finite Element Analysis (FEA), many different models are available. These Finite Element Models (FEMs) perform well regarding accuracy and robustness. Besides the vehicle model, the human surrogate (either a Crash Test Dummy or a whole-body Human Body Model) influences the simulation accuracy and runtime. Golman et al. used a full vehicle FEM and the Total Human Model for Safety (THUMS) [18], to simulate one selected Real-World accident from the CIREN [19] database. Overall, they achieved an accurate injury prediction. Only the accuracy of head injury prediction was not satisfying [20]. Despite the advantages of detailed vehicle models and human surrogates, they need a certain amount of computational resources to be run. The full vehicle model developed by Ganesan et al. has been run with the GHBMC model (Global Human Body Model Consortium) and the THOR dummy (Test Device for Human Occupant Restraint), the runtime was 43 hours for the HBM, compared to 17 hours for the dummy. Both simulations were performed on 96 CPU cores [21].

This high runtime can be an issue in an optimization process using HBMs, where several iterations of the FEA are needed. The number of FEA runs increases fast with the number of parameters and their variations. If four parameters are varied and a full fractional experimental design is chosen, the number of FEA runs is the product sum of the number of variations per parameter. The FEA matrix for four parameters with two variations per parameter results in 16 (2^4) FEA runs (Figure 2-1).

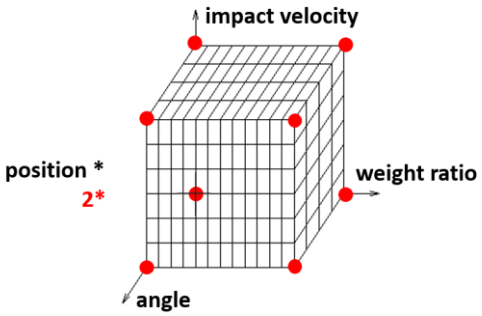

Figure 2-1 FEA matrix for a full fractional parameter variation for two variations per parameter, and four parameters.

If four parameters are varied, the total number of FEA runs increases with the number of variations. Assuming 17 hours per FEA run, the runtime increases as shown in Figure 2-2. Hence, optimization tasks can be very demanding.

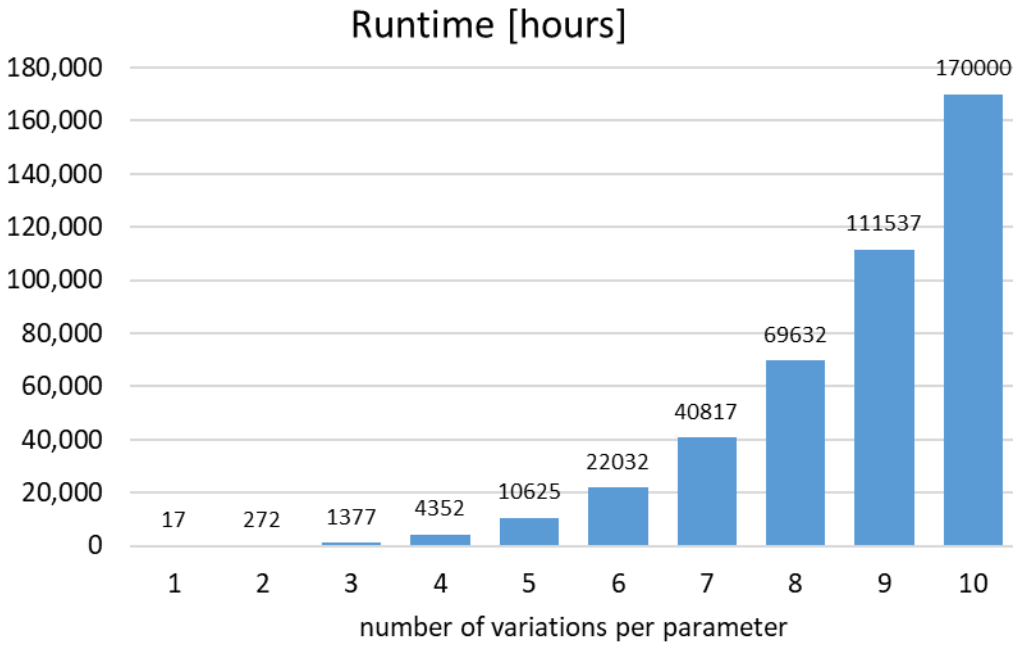

Figure 2-2 Runtime versus the number of variations per parameter, assuming 17 hours per FEA and four parameters.

2.2 Managing the Computational Effort

Many approaches have been developed to reduce computational effort or increase computational resources, yet these methods have their individual limitations. Some possible approaches are discussed in the following.

2.2.1 Parallel Computing

One option to deal with the increasing computational effort is parallel computing. Here the approach is to simply increase the computational resources. Due to the improvements in microprocessor technology during the last decades, the opportunity of using several processors for computing has already become state of the art. Additionally, the clock rates have increased. However, there are still limitations like the storage system speed that provides data to the processors. Furthermore, the economic standpoint must be considered due to the costs of acquiring and maintaining the hardware and software. [22]

Furthermore, the use of Graphic Processor Units (GPUs) for computing is promising and was discussed by Steuben. The use of parallel computing GPUs needs a deeper understanding. In his thesis, he addresses the problems with parallelization, synchronization, and approximation. [23]

2.2.2 Model Simplification

Simulation models are usually based on Computer Aided Design (CAD) models. Therefore, the complexity of the geometry design created in CAD has significant leverage on the mesh's complexity for the simulation. [24]

An approach to reduce computational effort is to reduce the geometry's complexity while aiming for a slight loss of accuracy. Examples of complexity reductions are removing fillets, holes, or screws, etcetera. An automated approach based on this was developed by Mounir et al.. [25]

2.2.3 Sub-System Models

Another option is to reduce the involved parts to the most relevant ones. Such a sub-system model is often called *buck model*. Due to the reduced number of components and relations, buck models are less computationally expensive. Iraeus and Lindquist [8] developed a driver-s6ide interior buck model to estimate rib fractures' risk in oblique frontal crashes. The model was validated with the NASS CDS. It matched the risk for senior occupants but overestimated the risk for young occupants. A sedan buck model for pedestrian impact response estimation has shown good performance and is well-reviewed by several studies [26][27][28].

2.2.4 Metamodeling

Representing physical problems with computer simulation models has become an integral part of engineering disciplines. Models are getting more and more complex. Often, they must be run several times for optimization processes. A common attempt to manage the increasing need for computational resources is using so-called meta-models or surrogate models, which became more popular in the last decades. These meta-models connect the input vector and the output vector of a computer simulation with mathematical algorithms. The wide field of applications for meta-models was reviewed by Alizadeh et al. by comparing more than 200 papers. When applied to a vehicle side crash simulation a possible input vector could be the striking vehicles impact velocity and mass. The output vectors are the struck vehicles' door intrusion and delta-v. By running FEA with the input vector, the output vector is calculated by solving many differential equations using physical boundary conditions. These complex relations are challenging to understand and computationally expensive. The meta-model connects these vectors with, in comparison to FEA, simple algorithms. This can make it easier to understand the input vector's influence on the output vector. [29]

A straightforward and universal definition of a meta-model is explained by Simpson et al.. If the relation between the input parameter y and output parameter x of a computer simulation can be defined as y=f(x), it is possible to approximate this function by defining

a meta-model as $\tilde{y}=g(x)$. Hence, the approximation is $y= \tilde{y}+e$ where e is the approximation error and the random error of the simulation. This can help to understand the relationship between y and x better and speed up design optimization processes. [30]

Due to many available meta-model types, it is nontrivial to select the most suitable type for a specific problem. Furthermore, every meta-model type has optional types that specify their behavior and hyperparameters, which can be varied to achieve a better approximation. For example, the meta-model type Kriging provides five different optional types (Linear, Power, Gaussian, Exponential, and Spherical). The hyperparameters of Kriging are the correlation function parameters. Jian et al. have collected and analyzed 26 different methods for the whole meta-model selection process. [31]

3 OBJECTIVES

Since current crash tests only cover a small range of parameters (impact velocity, weight ratio, impact angle, IRD), it is not well understood how well vehicles perform in crashes that differ from those test conditions. To address this, full vehicle FEA with human surrogates could be a valuable tool that helps to explore a larger space of parameters, yet they can be computationally expensive. The large number of simulations needed in an optimization process and the related computational effort may result in longer periods required for designing new vehicles and restraint systems. To deal with these problems, the approach in this thesis is to use a meta-model to predict the struck vehicles' door intrusion and velocity. A certain number of FEA is used as training points to train a meta-model. The minimum number of FEA runs required investigated by error analysis. Suitable meta-model types are tested and ranked due to their prediction quality.

This master thesis aims to reduce the computational effort of side crash FEA by replacing the full vehicle FEA with a meta-model. Hence, the following research questions are investigated:

- How well do current crash tests represent Real-World side crash configurations?
- Which meta-model type is the most promising to predict the stuck vehicles door intrusion and velocity?
- How accurate is the meta-model prediction in comparison to the finite element analysis?

4 METHODOLOGY

Figure 4-1 shows the overall methodology used in this thesis. The first step was to identify the parameters that are influencing the crash severity. This was done by approximating the side impact as a simple two-mass impact model. For practical reasons, the parameters are simplified and called input parameters. The distribution of the chosen input parameters was derived from Real-World accident data (NASS CDS) and compared against the IIHS and Euro NCAP MDB side impact crash test configurations (Table 1). As a result of this step, the input parameters range was set. The boundary conditions required for an occupant simulation model were evaluated since they influence the occupants' injury severity. Three different training sets were defined related to the input parameter range. FEA runs in which a full vehicle model struck by an MDB model were performed using those input parameters variations. The FEA results were prepared to get suitable output parameters for meta-model training. The input and output parameters were combined in three different training sets to evaluate which amount of training data is required. Five different meta-model types were trained using those sets, and their performance was ranked using a validation set. Furthermore, the meta-model prediction was compared to ten FEA runs with random input parameter variations.

Methodology

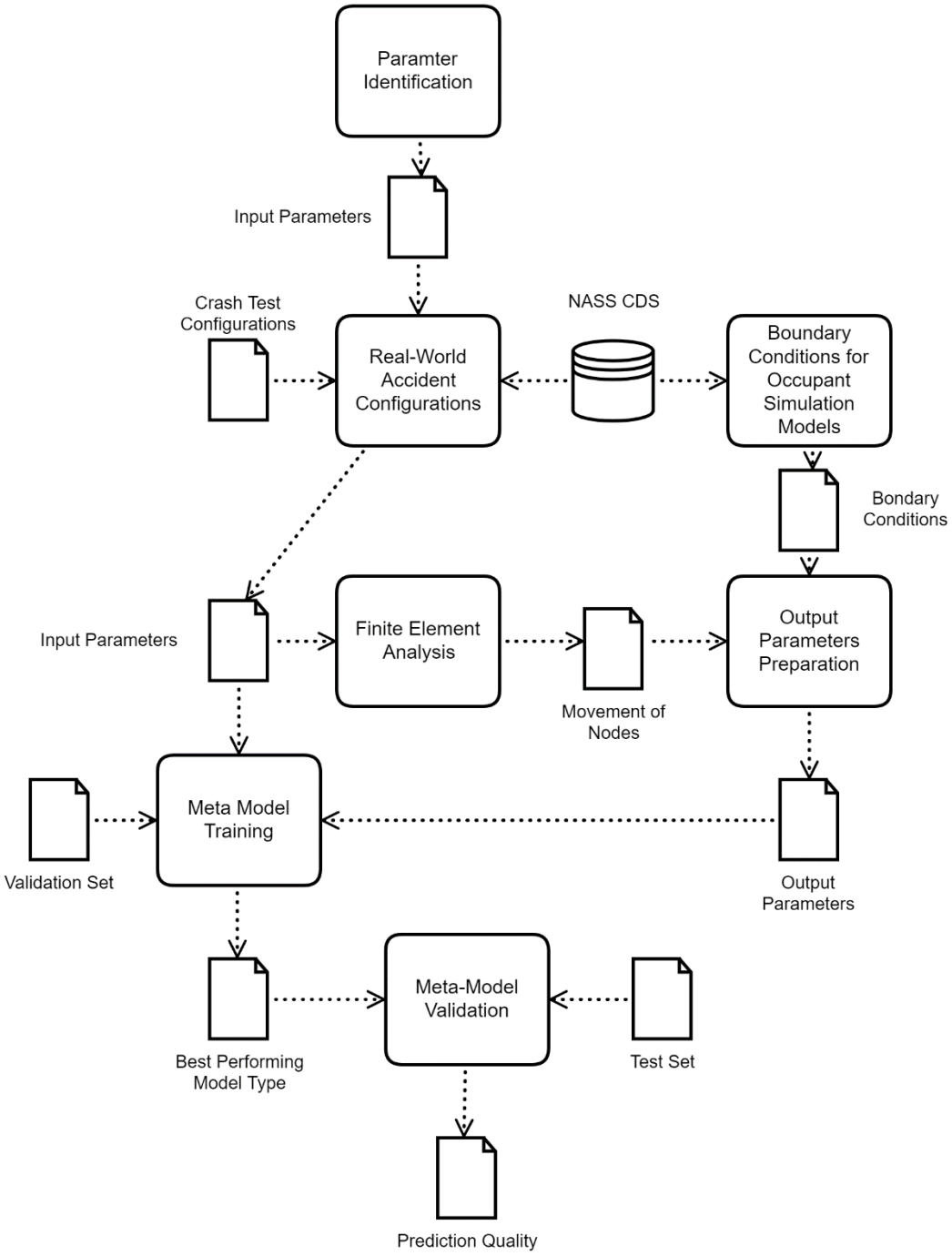

Figure 4-1 Flow chart of the overall methodology used in this thesis

4.1 Input Parameters

A simple collision model is used to identify the parameters that influence the magnitude of force that the struck vehicle is experiencing due to a side impact. The approach used by Burg and Moser for vehicle accident reconstruction was investigated [32].

4.1.1 Input Parameter Identification

Assuming the side impact as an inclined, smooth, and eccentric impulse and approximating the vehicles as rigid bodies, the impact can be sketched as in Figure 4-2. The striking vehicle is represented by body 1, the struck vehicle by body 2. Both bodies have an initial velocity. Just the part of the velocity that is normal to the contact plane is relevant. Furthermore, an angular velocity is considered for both vehicles. [33]

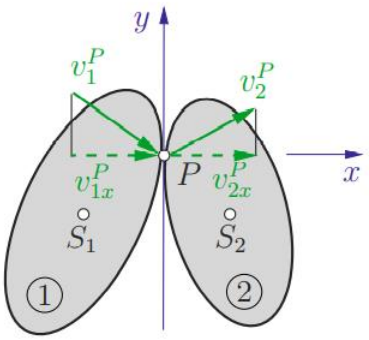

Figure 4-2 Elastic, inclined, smooth and eccentric impulse approximation. [33]

The next step is to make a free body diagram, as shown in Figure 4-3. For both bodies, the mass and the moment of inertia are relevant. Furthermore, the contact force's normal distance to the center of gravity of each body is essential. [33]

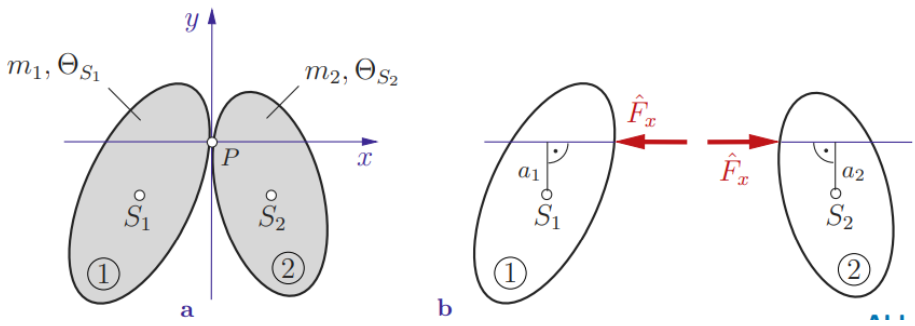

Figure 4-3 Free body diagram of the impulse approximation. [33]

The force equilibrium condition and momentum conservation are used to calculate the impact force (Equation 1).

$$\hat{F}_x = (1+e)\frac{v_{1x} - a_1\omega_1 - (v_{2x} - a_2\omega_2)}{\frac{1}{m_1} + \frac{1}{m_2} + \frac{a_1^2}{\theta_{S_1}} + \frac{a_2^2}{\theta_{S_2}}}$$

Equation 1; General impact force of an inclined, smooth, eccentric impulse. [33]

The parameters used in Equation 1 are defined in Table 2.

Table 2 Parameter description for an inclined, smooth, eccentric impulse.

Parameter	
$\hat{F}_x$	Force at the contact point
e	Coefficient of restitution
v_{1x}	Velocity of the striking vehicle normal to the contact plane
v_{2x}	Velocity of the struck vehicle normal to the contact plane
a_1	Orthogonal distance of the impact force to the center of gravity of the striking vehicle
a_2	Orthogonal distance of the impact force to the center of gravity of the stuck vehicle
ω_1	Angular velocity of the striking vehicle
ω_2	Angular velocity of the stuck vehicle
m_1	Mass of the striking vehicle
m_2	Mass of the struck vehicle
θ_{S_1}	Moment of inertia of striking vehicle about its center of gravity
θ_{S_2}	Moment of inertia of struck vehicle about its center of gravity

For simplification reasons, some parameters are set to constant values. It is assumed that both vehicles have no angular velocity, which means there is no yawing motion prior to the crash. The velocity of the struck vehicle is set to zero. The coefficient of restitution is set to one, which means a perfect elastic impulse is assumed. These assumptions simplify Equation 1 to Equation 2.

$$\hat{F}_x = \frac{2 * v_{1x}}{\frac{1}{m_1} + \frac{1}{m_2} + \frac{a_1^2}{\theta_{S_1}} + \frac{a_2^2}{\theta_{S_2}}}$$

Equation 2 Simplified calculating the impact force. [33]

The simplified Equation 2 is a function of the striking vehicle's impact velocity, the mass of the two vehicles, and the contact point position. Those parameters are not practical to apply on FEA due to their complexity. Hence, the impact velocity is the velocity of the striking vehicle. The weight ratio represents the two masses of the vehicles. The impact angle and the POI represent the impact force's orthogonal distance to the center of gravity of both vehicles and the moment of inertia of both vehicles.

4.1.2 Real-World Accident Configuration

The range of the input parameters should represent the impact conditions observed in Real-World accidents. The NASS CDS was used to derive the range of input parameters. Due to the weighed sampling system, the NASS CDS represents all vehicle accidents that are reported to the police in the US. It includes accidents with passenger cars, light trucks and vans. The data is publicly available and can be downloaded from a FTP server. Furthermore, the crash test parameters from Table 1 of IIHS MDB 2.0 and Euro NCAP MDB are added for comparison. [5]

Impact Velocity

The NASS CDS does not provide the impact velocity as a parameter. Therefore, it is calculated according to Sunnevång et al. using the masses of the striking and the struck vehicle in combination with the total Delta-V of the struck vehicle, see Equation 3. [34]

$$Impact\ Velocity = \left(\frac{m_{struck}}{m_{striking}} + 1\right) * \Delta v_{struck}$$

Equation 3 Calculation of the impact velocity using the masses of the striking and struck vehicle and the Delta-V of the struck vehicle. [34]

Weight Ratio

The weight ratio is calculated by dividing the mass of the striking vehicle, by the mass of struck vehicle, see Equation 4. The mass of a Honda Accord (model year 2014, mass 1666 kg) [21] is used to represent a possible crash test case.

$$Weight\ Ratio = \frac{mass_{striking}}{mass_{struck}}$$

Equation 4 Calculation of the weight ratio

Impact Angle

For the impact angle, the parameter Direction of Force of the most harmful event (DOF1) is used. The DOF1 of left side impacts is mirrored to make them comparable toright side impacts. The distribution of the DOF1 cannot be directly compared with the impact angle of the MDB because it depends on several parameters, for example, the angle of the contact plane. [32].

Point of Impact relative to the Wheelbase

The parameter DVD gives the distance from the direct damages' center to the middle of the weelbase of the struck vehicle, reported to the in the NASS CDS. For comparing the DVD for vehicles of different sizes, the DVD is normalized with the struck vehicle's wheelbase. A value of zero represents a force acting at the center of the wheelbase (in the middle of fronat and rear axle), while 100 represents a force acting directly at the

front axle. A force acting at the rear axle is represented by a value of -100, respectively. The DVD distribution cannot be directly compared to the MDB position because it depends on several parameters [32].

4.1.3 Design of Experiments

The DoE defines how the evaluated points are distributed within the experimental space of input parameters. The type of DoE has impact on the prediction quality. A simple DoE approach is the factorial design; suitable for observing main effects. Its major disadvantage is, that it is not optimal for deterministic problems, which is the case in this thesis. A space filling design would be more appropriate for some model types like kriging [30]. However, due to the meta-modelling approaches' high complexity for the underlying problem, the fractional design was chosen. Three different datasets were used for the meta-model training to evaluate the effects of different input parameter ranges on the prediction quality. One training set should cover the whole parameter range with three variations per parameter, as a full fractional design, called Full Range Model (FRM). The lower limit, the upper limit, and one point between the limits were chosen. For the second training set, called Half Range Model (HRM), the input parameter ranges of the impact angle and the position were reduced, but otherwise, the DoE was chosen the same way as for the FRM. For the third training set, called Focused Model (FM), the focus was set on the variation of the input parameters angle and position. Additionally, the amount of simulations was reduced.

4.2 Finite Element Analysis

NHTSA (National Highway Traffic Safety Administration) provides several full vehicle Finite Element models. In this thesis a Honda Accord (model year 2014) [21] was used as the struck vehicle. For the striking vehicle the IIHS MDB 1.0 developed by LSTC (Livermore Software Technology Corporation) was used. Both models are publicly available. The occupants (two THOR-50M at the front seats) and the included restraint systems (driver, passenger and curtain airbag and belts) were removed from the model

to reduce computational effort. The striking and struck vehicle type was not varied. Instead the Honda Accord and the IIHS MDB were used for all simulations to see the influences of varying input parameters. Another boundary condition is that there was no variation of the Honda Accord parameters. This means the stuck vehicle had the same mass (1666kg) and the same velocity (0 kph) in all simulation runs. Therefore, the input parameters are just depending on the IIHS MDB parameters. Hence, the impact velocity was represented by the longitudinal velocity of the MDB. The weight ratio was varied by adding or removing mass on the MDB carriage. The original mass of the used MDB 1.0 is 1500 kg. The default impact angle was a perpendicular impact. Offsets were applied by rotating the MDB, where counterclockwise rotation was represented by a positive angle. The distance from the front axle to the centerline of the MDB was used to specify the Point of Impact (Figure 4-4).

All simulations were run using LS Dyna R9.3.0, on a high-performance Linux cluster using 64 CPU cores.

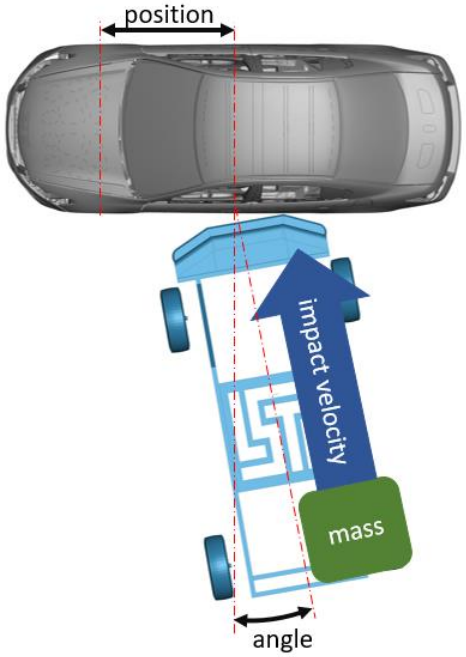

Figure 4-4 FEA setup with input parameters. [21]

4.2.1 Approximation of the Crush Surface

Since the relative intrusion of the door and the B-pillar is of interest, a relative coordinate system was used to derive the intrusion. This was realized by a sensor mounted at the non-struck side of the vehicle, where no intrusion occurs (passenger-side door). Hence, it was not affected by the crash deformation.

Furthermore, it is not possible to predict the intrusion of a large number of nodes that represent the FE-mesh of the vehicle model. Hence, the intrusion was approximated by moving, rigid planes that represent a simplified crush surface. Each plane was defined by three nodes from the vehicle model. Just the lateral displacement was of interest. Other displacements (longitudinal, vertical) of the node were neglected. The planes were chosen to cover most of the relevant contact surfaces for occupant simulations (thorax, shoulder, abdomen, pelvis). For illustrating possible contact surfaces, a 50-percentile male THOR-dummy was placed at the driver seat (Figure 4-5) [21]. All planes have the same size, and the defining nodes' location was the same within each plane. The selected nodes are located on the outer door panel., except for planes C and F, where the defining nodes were located on the B-pillar. The B-pillar was chosen because the edge of the outer door panel could influence the nodes' movement. Furthermore, the B-pillar deformation is assumed to be more accurate due to its higher stiffness.

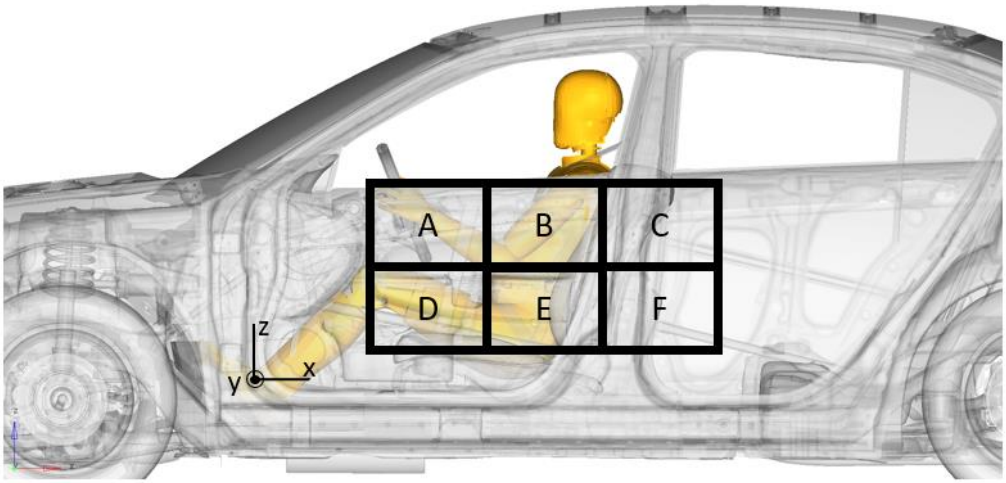

Figure 4-5 Definition of the intrusion planes. [21]

The planes are 350 mm wide and 250 mm high (b=350 mm; h=250 mm, Figure 4-6), with the lower-left edge of plane D starting at x=670,6 mm behind the front axle. The z coordinate is 465 mm above the ground. There is no gap between the planes in their initial position. A rotation of the planes is possible due to the definition with three nodes. Since a complex intrusion profile is approximated with a limited number of rigid planes some deviation is unavoidable.

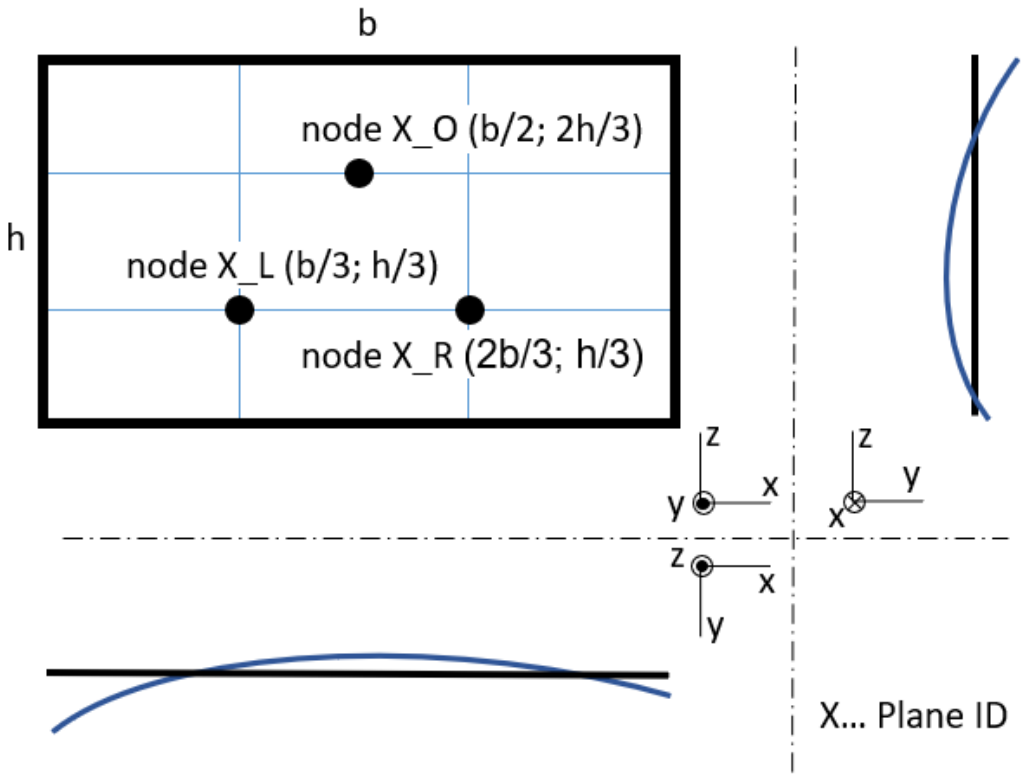

Figure 4-6 Plane and node definition and possible deviation due to rigid plane approximation.

4.2.2 Velocity of the Struck Vehicle

In Addition to the intrusion prediction the struck vehicles velocity during the crash is relevant. The struck vehicles lateral velocity (C_V). was calculated using the global y-position of the sensor.

4.2.3 Error analysis due to rigid plane approximation

Three nodes per plane were chosen to analyze the error associated to the rigid plane approximation. The relative distance of these nodes to the plane was measured over time. In Figure 4-7, the location of the nodes used for error analysis is shown. The black dots are the nodes that define the plane, and the colored dots are the nodes used in error analysis. Due to lack of time, this error was analyzed for one single FEA run (highest velocity and highest weight ratio). It was assumed that the maximum error occurs in this case for a perpendicular impact Yet, the researcher cannot preclude that larger errors are observed in simulations with non- perpendicular impacts.

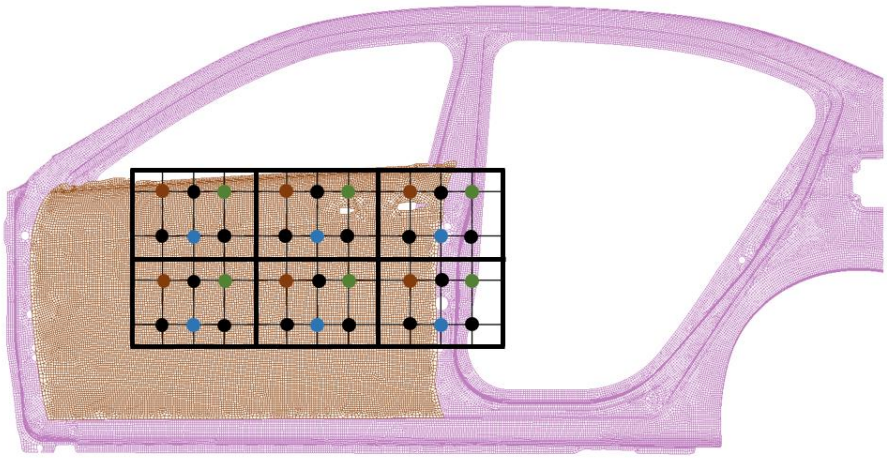

Figure 4-7 Nodes used for evaluating the error due to the rigid plane approximation (colored dots). [21]

4.3 Output Parameters

Since the FEA output curves show some fluctuations, simplifications were applied to the intrusion and velocity versus time curves. First, deviations prior to the beginning of the actual intrusion were replaced by an exponential curve. The beginning of the actual intrusion was defined by exceeding a penetration depth of five millimeters. Second, a polynomial curve was used to remove local fluctuations. The relevant time range where curve fitting was applied beginning at the time step where the amount of intrusion exceeds a depth of five mm and ends at 120 ms, since peak intrusion already occurred

at this time. A fourth-degree polynomial was assumed to be a good compromise between approximation accuracy and the number of needed meta-models.

4.3.1 Curves Approximation

The FEA intrusion and velocity curves showed some unexpected fluctuations. To ensure that the FEA deviations were not influencing the output parameters, they were removed. First, the deviations before the beginning of the actual intrusion were replaced by an exponential curve. The beginning of the actual intrusion is defined by exceeding five mm' penetration depth. Second, a polynomial curve was fitted to get rid of local deviations. The relevant time range where curve fitting was applied begins with the time step where the intrusion exceeds a depth of five mm and ends at 120 ms.

4.3.2 Influence of the Input Parameters

The output parameters should be applicable for all output curves. To evaluate the input parameters' influence, they were varied, and the intrusion and velocity curves were compared. Therefore, three input parameters are set to the central value, while the fourth was varied. Therefore, the individual contributions of each input parameter could be analyzed. This was done for one node of plane E (E_O).

4.3.3 Input-Output Parameters Comparison

To get an overview of the training sets and the relations between the input and output parameters, they were plotted versus the simulation number. There is a lot of information gathered for each node in those plots. Each node has five output parameters that were evaluated, regarding to four input parameters, in 81 (HRM, FRM), respectively 40 (FM), simulations. Therefore, each nodes plot consists of 729 (HRM, FRM) or 360 (FM) data points. There are 19 of those plots. Hence, one node (E_O) is reviewed more detailed, while the others are listed in the appendix (8A.2). However, some general states were made that apply for all nodes. The observed trends from the input parameter influence investigation can be checked as well as the output parameter

preparing method correctness. For a better overview the parameters were normalized with their maximum value.

4.4 Metamodeling

As there is a wide variety of meta-models with many of them using optional types and hyperparameters, it is not trivial to choose an appropriate meta-model for a specific purpose. There are several methods to choose the meta-model type, the optional type and the hyperparameters [31]. The choice of the approach is also depending on the available framework and software resources of the researcher. In this thesis the Surrogate Modeling Toolbox (SUMO) developed by Gorissen et al. [35] was used. SUMO supports a wide range of model types, optimization algorithms, selection algorithms, sample selection types, design of experiments and sample evaluation methods.

Since different meta-model types may be appropriate for one specific application, meta-models of different type were build using a Generic Algorithm (GA). Cross validation was used in the GA to get an optimized meta-model of each type. Cross-validation uses the training points to evaluate the meta-model's goodness of fit. The meta-model building repeats until one of three conditions is satisfied. These conditions are the maximum number of samples reached, the required accuracy set by the user was achieved, or the maximum time (set by the user) was exceeded [36, 37]. The result of the GA is the best performing meta-model for each type, with optimized optional-type and optimized hyperparameters. The selection of the best performing meta-model type was done by comparing the Root Relative Square Error (RRSE, Equation 5) for the predicted output parameters. Here the validation set, consisting of 16 points (Table 3), was used.

Table 3 The validation set, consisting of 16 FEA runs (full fractional design).

$weight\ ratio$	$impact\ velocity\ [kph]$	$angle\ [°]$	$position\ [mm]$
1.0	30	−5	1497
1.4	50	5	1697

For the cross-validation and the validation with the validation set the Root Relative Square Error (RRSE) was used. For the RRSE, the meta-model's deviation is compared to the deviation of the simplest model, the mean. It is a good measure for comparing different models, yet it is not a measure to assess the goodness of fit. A perfect fit is represented by a RRSE of zero, while a RRSE of one indicates that the simplest model would give the same error. However, RRSE does not imply a bad approximation in case the simplest model already provides a good fit. According to Gorissen et al., it can be defined as in Equation 5 [36]. The squared deviation of the points of the validation set (y_i) and the predicted points ($\tilde{y_i}$) is compared to the squared deviation of y_i and the mean-model ($\bar{y}$) of the training points. This is summed up for n validation points and the square-root is taken.

$$RRSE_{(y,\tilde{y})} = \sqrt{\frac{\sum_{i=1}^{n}(y_i - \tilde{y_i})^2}{\sum_{i=1}^{n}(y_i - \bar{y})^2}}$$

Equation 5 Root Relative Square Error. [36]

4.4.1 Meta-model Types

The underlying problem is of deterministic nature with multiple input and output parameters. According to Simson et al., Artificial Neuronal Networks, Response Surface models and Gaussian process models are suitable models for this application. [30] The chosen meta-model types are also depending on the toolbox and the availability of the GA for this meta-model type. Furthermore, the model building time is relevant. Since the Artificial Neuronal Networks (ANN) building time was much higher than of the other meta-model types it was not used.

From that point of view, the model types, Kriging, Least-Squares Support-Vector Machine (LSSVM), Rational, Radial Basis Function (RBF), and Gaussian Processes for Machine Learning (GPML) were chosen. They are briefly explained in the following.

Rational model

The simplest meta-model type of the selected types is the Rational model. It can be defined as in Equation 6 with ratios of polynomials (rational functions). The degrees of freedom of the rational functions $\alpha_{(x)}$ and $\beta_{(x)}$ are depending on three parameters, the variable weighting, the denominator flags, and degrees of freedom. Those are set during the GA. [38]

$$\tilde{y}_{(x)} = \frac{\alpha_{(x)}}{\beta_{(x)}}$$

Equation 6 Meta-model type Rational.

Kriging

The Kriging meta-model type is based on a combination of a polynomial model ($f_{(x)}$) and local deviations ($Z_{(x)}$), see Equation 7. While Kriging is based on a Gaussian process it uses previous covariance for a better approximation. [29] $Z_{(x)}$ is assumed to have a mean of zero and its correlation function is stochastic. A variety of correlation functions have been developed, those are also known as the meta-model optional type [30]. Depending on the optional type are the hyperparameters, which are optimized in the GA.

$$\tilde{y}_{(x)} = f_{(x)} + Z_{(x)}$$

Equation 7 Meta-model type Kriging. [29]

Radial Basis Functions

RBF was developed for multivariate data interpolation. It is a mathematical function that operates with real values. Based on the distance of the origin (Equation 8) and the center (Equation 9), this values are calculated. [39]

$$Q_{(x)} = Q_{(||X||)}$$

Equation 8 Distance from the origin. [39]

$$Q_{(x)} = Q_{(||X-c||)}$$

Equation 9 Distance from the center. [39]

The RBF meta-model can be defined as in Equation 10. It consists of n radial basis functions (r_i) that are integrated. This functions are depending on the distinct x_i and a weight w_i. [40]

$$\tilde{y}_{(x)} = \sum_{i=1}^{n} r_i Q(||x - x_i||)$$

Equation 10 Meta-model type Radial Basis Functions. [40]

GPML

The GPML model is based on the Gaussian distribution, but while the Gaussian distribution is using vectors, the GPML is using functions. As both meta-model types Kriging and GPML are based on Gaussian process, they are nearly identical. The GPML can be simply written as a combination of a deterministic function ($f_{(x)}$) added to a Gaussian focused process ($Z_{(x)}$) that is characterized due to its covariance function (Equation 11). [41]

$$\tilde{y}_{(x)} = f_{(x)} + Z_{(x)}$$

Equation 11 Gaussian Process for Machine Learning. [41]

LSSVM

The Support Vector Machines (SVM) method is based on minimizing the generalization error, while other meta-model types aim to minimize the training error. The generalization error is minimized by maximizing the space between the separating hyperplane and the data. The classifier (Equation 12) consists of n training points (y_i, x_i), two constants ($\propto_i, b$) and a function ($\Psi_{(x,x_i)}$). $\Psi_{(x,x_i)}$ defines the optioal type some examples are: linear, polynomial, radial basis function, or a several layers neural. [42]

$$\tilde{y}_{(x)} = sign\left[\sum_{i=1}^{n} \propto_i y_i \Psi_{(x,x_i)} + b\right]$$

Equation 12 Meta-model type Support Vector Machine. [42]

The traditional approach solving Equation 12 leads to quadratic programming, while the least squares approach end up in a set of linear equations. [43]

4.5 Meta-model Validation

The meta-model should predict the intrusion and velocity curves as boundary conditions for an occupant simulation model. The applicability is assessed by comparing the predicted curves with the FEA result curves for the same input parameters. Several studies have used some form of the Normalized Root Mean Square Error (NRMSE) to assess prediction values [44][45][46]. In this study the NRMSE is calculated by dividing the deviation of original intrusion (y_i) and the predicted intrusion ($\tilde{y}_i$) by the deviation between y_i and the mean of the original intrusion ($\bar{y}_i$) (Equation 13). The evaluation is done from the beginning of the predicted intrusion to the maximum of the predicted intrusion, as illustrated in Figure 4-8. The mean RRSE for the intrusion of all predicted nodes, the vehicles' velocity, and validation points was calculated. A NRMSE of zero is a perfect prediction, while a value of one means that the simplest model would give the same prediction error.

$$NRMSE = 1 - \frac{\sum_{i=1}^{n} |y_i - \tilde{y}_i|}{\sum_{i=1}^{n} |y_i - \bar{y}_i|}$$

Equation 13 Normalized Root Mean Square Error.

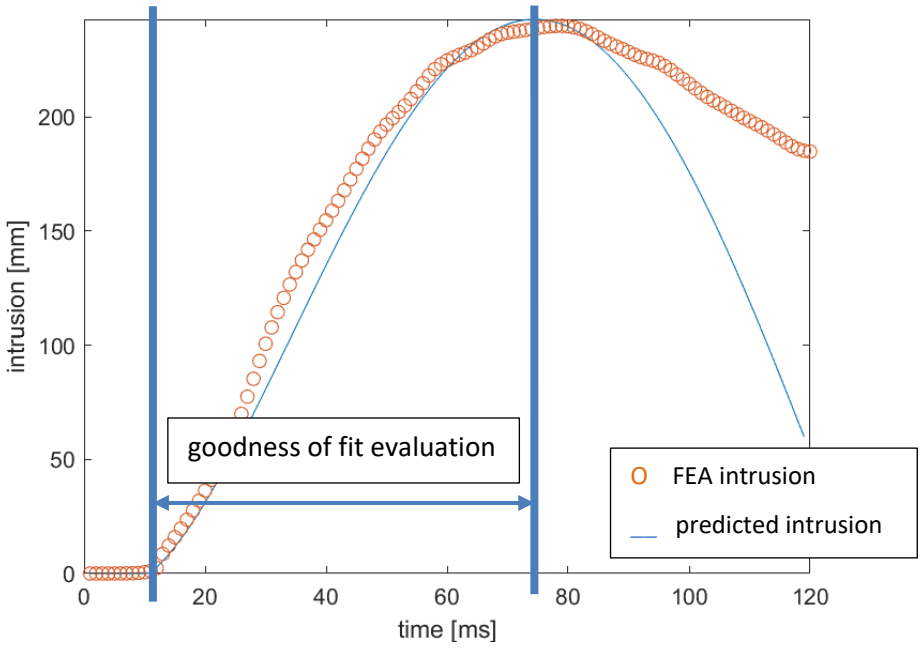

Figure 4-8 Time range of the prediction evaluation.

The used test set is randomly chosen in the input parameter range and consists of ten simulations (Table 4).

Table 4 Test set for meta-model validation.

Simulation ID	weight ratio	impact velocity [kph]	angle [°]	position [mm]
1	0.86	23	-4	1425
2	1.41	55	1	1678
3	1.39	22	5	1398
4	0.91	49	-6	1499
5	1.15	31	7	1510
6	1.05	52	11	1891
7	1.21	31	14	1609
8	1.39	33	19	1457
9	1.53	44	-15	1300
10	0.92	26	-17	1250

5 RESULTS

5.1 Input Parameters

First, the distribution of input parameters identified with the simple collision model, obtained from Real-World accidents of NASS CDS is compared against currently used parameters in crash test protocols. Based on those accident data, the input parameter range for the DoE is defined, considering limitations of the FEA models. Approximation errors due to simplifications are evaluated and addressed. Finally, the results of the meta-model training and are presented and assessed.

5.1.1 Real-World Accident Configuration

In this section, data obtained from NASS CDS is presented to set the range of input parameters. Additionally, the parameters used in the IIHS Side MDB and Euro NCAP Side MDB are shown. For the following boxplots, the whiskers were defined by the respective quartile plus/minus 1.5 times the interquartile range. The value of the impact velocity in real-world accidents varies from three kph up to 191 kph (Figure 5-2), while both crash tests use an impact velocity of 60 kph. More than three out of four accidents have a lower impact velocity than the crash tests. The accidents' weight ratio is mainly between 0.18 and 1.96 with a maximum outlier of 4.13 (Figure 5-1). For this parameter, the two tests have different values.

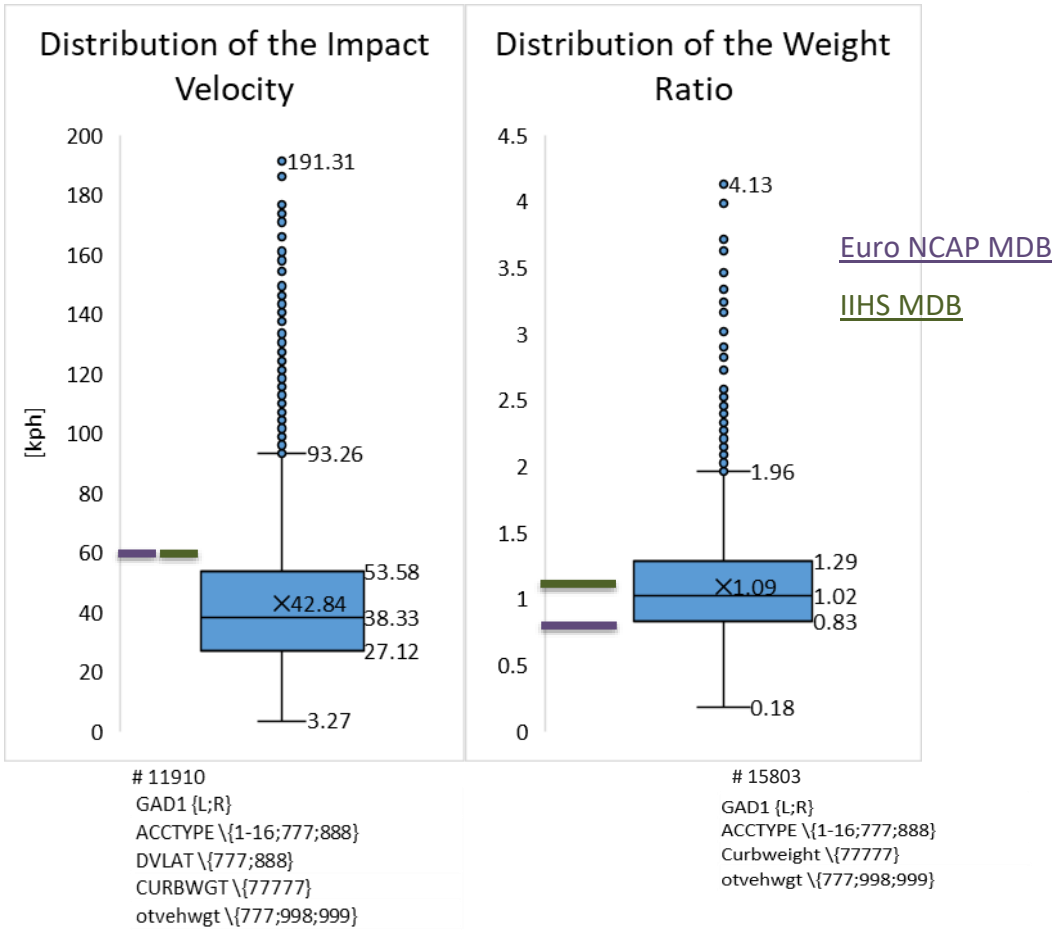

Figure 5-2 Distribution of the impact velocity

Figure 5-1 Distribution of the Weight Ratio

Both MDB side impact tests have a DOF1 of three, representing a perpendicular impact. Three out of four vehicles experienced a DOF1 between 12 and three o'clock (Figure 5-3), the others are distributed between three and six o'clock. This means that the majority of struck vehicles are experiencing an impact force that is angled between a front impact (DOF1=12) and a perpendicular impact (DOF1=3). Figure 5-4 shows that more POIs are located behind the center of the wheelbase. Also, the IIHS MDB is slightly behind the middle of the wheelbase for the Accord test, almost equal to the mean value obtained from NASS CDS data. For the Euro NCAP test, the R-value is not known. Hence it is not shown in the figure.

Euro NCAP MDB

IIHS MDB

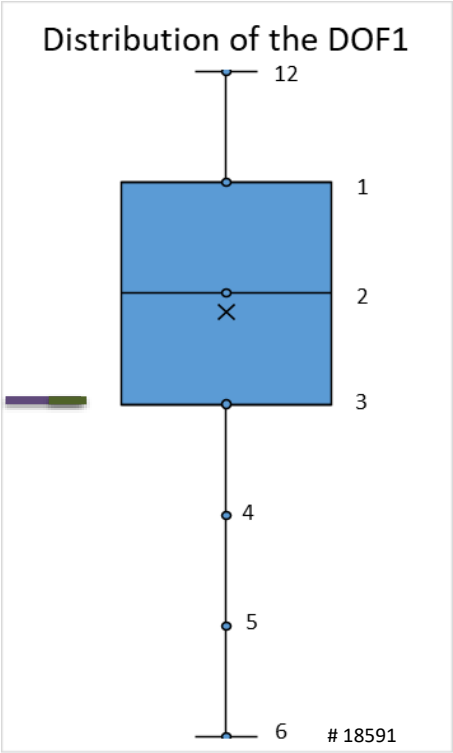

Figure 5-3 Distribution of the DOF1.

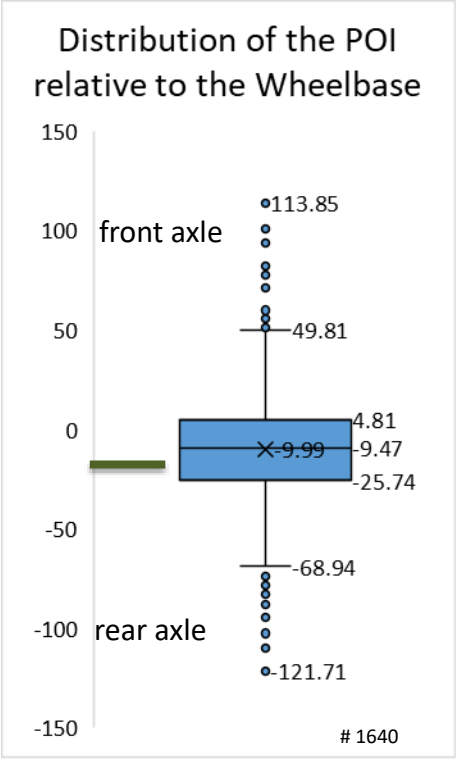

Figure 5-4 Distribution of the POI relative to the wheelbase

5.1.2 Input Parameter Range

Many assumptions were necessary to set these limits properly. On the one hand, a wide range of the Real-World side crashes, shown in previous figures, should be covered, while on the other hand, the FEA result curves should be comparable, meaning that a narrower range would be preferred. For the impact velocity, a value higher than 20 kph is needed. Otherwise, the intrusion is too small for a meaningful prediction result. However, intrusions of less than 50 mm are assumed to be irrelevant for occupant simulation models since injury severity is expected to be low. The upper limit for the impact velocity is the passenger compartment's complete structural failure. Furthermore, the gap between the training points should not be too large. Therefore, an upper limit of 60kph is assumed to be a good compromise and the impact velocity range limits are set from 20 kph to 60 kph. 70.3% of the Real-World side crashes are covered by the chosen impact velocity range.

The MDB mass represents the weight ratio of the two vehicles, since the struck vehicle’s mass is constant in this thesis. Analogous to the impact velocity, a compromise between the coverage of Real-World side crashes and the distance between the training points is necessary. The weight ratio range is set from 0.8 to 1.6, which means the mass of the MDB is varied from 1333 kg to 2666 kg. This covers 70% of the Real-World side crashes.

When it comes to the impact angle, it is difficult to find reasonable limits because, with a higher angle, the crash turns more and more to a glace-off collision. In this case evaluating the output parameters is very difficult, because the curves change their characteristics. Hence, the range is set from -20° to 20° for the FRM and from -10° to 10° for the HRM.

A similar problem occurs for an extensive range of the position. Hence, the barrier's position is varied -400 mm and +400 mm relative to the default value of 1597 mm for the FRM and FM. For the HRM, the range is reduced to values from -200 mm to +200 mm relative to the default value (1597 mm).

5.1.3 Design of Experiments

The FRM set and the HRM set consist of 81 equally distributed FEA runs (Table 5 and Table 6). For the FM set, 40 FEA runs are used, five variations for the impact velocity and the weight ratio combined with eight variations of the impact angle and the impact velocity, visualized in Figure 5-5.

Table 5 Parameter range of input parameters of the FRM training data set (full fractional design).

$weight\ ratio$	$impact\ velocity\ [kph]$	$angle\ [°]$	$position\ [mm]$
0.8	20	−20	1197
1.2	40	0	1597
1.6	60	20	1997

Table 6 Parameter range of input parameters of the HRM training data set (full fractional design).

$weight\ ratio$	$impact\ velocity\ [kph]$	$angle\ [°]$	$position\ [mm]$
0.8	20	−10	1397
1.2	40	0	1597
1.6	60	10	1797

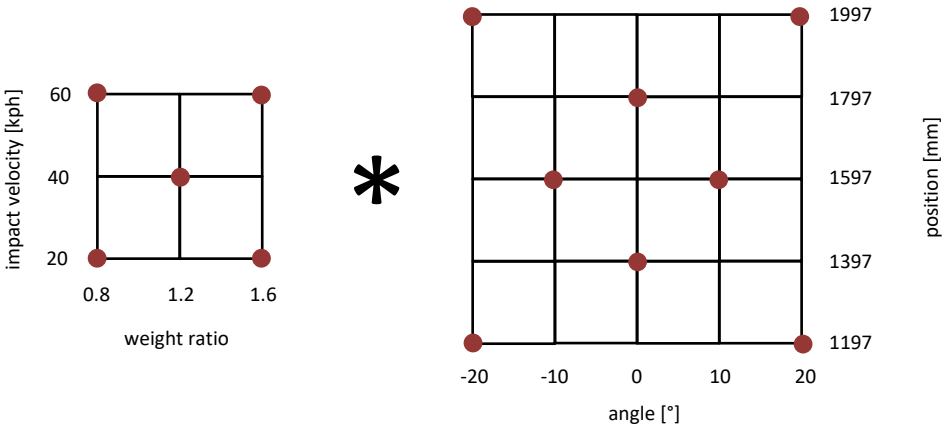

Figure 5-5 Variations of the input parameters for the FM training data set.

5.2 Output Parameters

5.2.1 Curve Approximation

Due to the intrusion curve's approximation with a polynomial curve of degree four, some deviation occurs. To get an overview of how good each curve's fit is, the NRMSE is evaluated. The mean for each intrusion and velocity curve over all FEAs is listed in Table 7. While the best approximation was reached by the HRM, which represents a smaller input parameter range for the impact angle and the position, the FRM and FM archived a similar approximation quality. The nodes of plane E and F (rear lower planes, see Figure 4-5) achieved a better approximation accuracy than the others. Plane A (front upper) is the worst performing intrusion panel. The C_V has a lower approximation accuracy than all nodes.

Table 7 Approximation error of the boundary curves. (NRMSE)

Plane	Node	FRM	HRM	FM	Mean Node	Mean Plane
A	A_L	0.886	0.902	0.890	0.893	0.899
	A_O	0.872	0.886	0.872	0.877	
	A_R	0.917	0.940	0.923	0.927	
B	B_L	0.931	0.952	0.933	0.939	0.935
	B_O	0.914	0.930	0.918	0.921	
	B_R	0.941	0.955	0.938	0.945	
C	C_L	0.919	0.943	0.919	0.927	0.922
	C_O	0.910	0.933	0.898	0.913	
	C_R	0.917	0.947	0.908	0.924	
D	D_L	0.882	0.917	0.890	0.896	0.916
	D_O	0.908	0.942	0.922	0.924	
	D_R	0.919	0.945	0.922	0.929	
E	E_L	0.936	0.964	0.939	0.946	0.952
	E_O	0.948	0.972	0.950	0.957	
	E_R	0.946	0.971	0.945	0.954	
F	F_L	0.939	0.963	0.932	0.945	0.942
	F_O	0.931	0.959	0.932	0.941	
	F_R	0.928	0.961	0.930	0.940	
-	C_V	0.856	0.863	0.852	0.857	-
Mean	-	0.916	0.939	0.916	-	-

5.2.2 Influence of the Input parameters

As the different input parameters have a different impact on the observed intrusion, their contribution was analyzed. The curves are shown in Figure 5-6. The Baseline input parameters are:

- Impact velocity of 40 kph
- Weight ratio of 1.2
- Impact angle of 0°
- Position of 1597 mm

The impact velocity correlated with the maximum intrusion, while it did affect neither the onset nor the time of maximum intrusion. Only the impact velocity was affecting the incline of the curve substantially. The weight ratio influenced the maximum intrusion time and had a negligible impact on the maximum intrusion value. Noticeable for the impact angle was that it was the only parameter that influenced the start of intrusion. Furthermore, the maximum intrusion and the maximum intrusion time were affected. For the position, influence at the maximum intrusion time and the maximum intrusion value was observed. The general shape of the intrusion curves is similar. The impact velocity seems to have the biggest influence on intrusion.

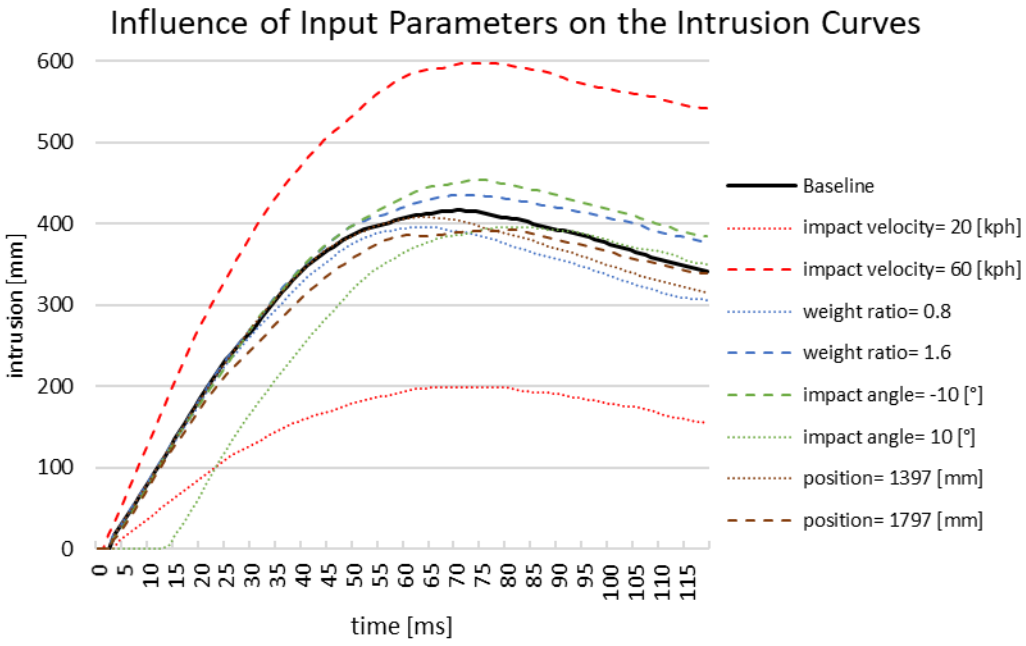

Figure 5-6 Influence of the input parameters on the intrusion curves.

For the Baseline of the velocity, the same input parameter values as for the intrusion Baseline are chosen. Interesting was the velocity reduction between 50 ms and 55 ms and a second increase after that. This could have resulted from a contact loss after a first impact and a second impact right after that. Depending on the involved parts' stiffness, the velocity gradient is higher or lower.

The impact velocity had an evident influence on the velocity of the struck vehicle, as it was expected (Figure 5-7). A higher gradient and a higher maximum velocity were observed for a higher impact velocity. Furthermore, a faster reduction of the velocity after the peak value was observed. The curve looks similar to the Baseline at the beginning of the crash for different weight ratios, yet for a higher weight ratio, the struck vehicle's maximum velocity was higher and vice versa. Noticeable for the impact angle of 10° was that a similar time shift as for the intrusion curve was observed. However, the impact angle variation did not significantly influence the maximum velocity. The position influenced the observed loss of contact. Furthermore, the position influenced the maximum velocity. Noticeable was that at a time of 75 ms, the curves with position and impact angle variations stabilized at a quite similar velocity. As for intrusion, the impact velocity showed the most significant impact on the velocity curves.

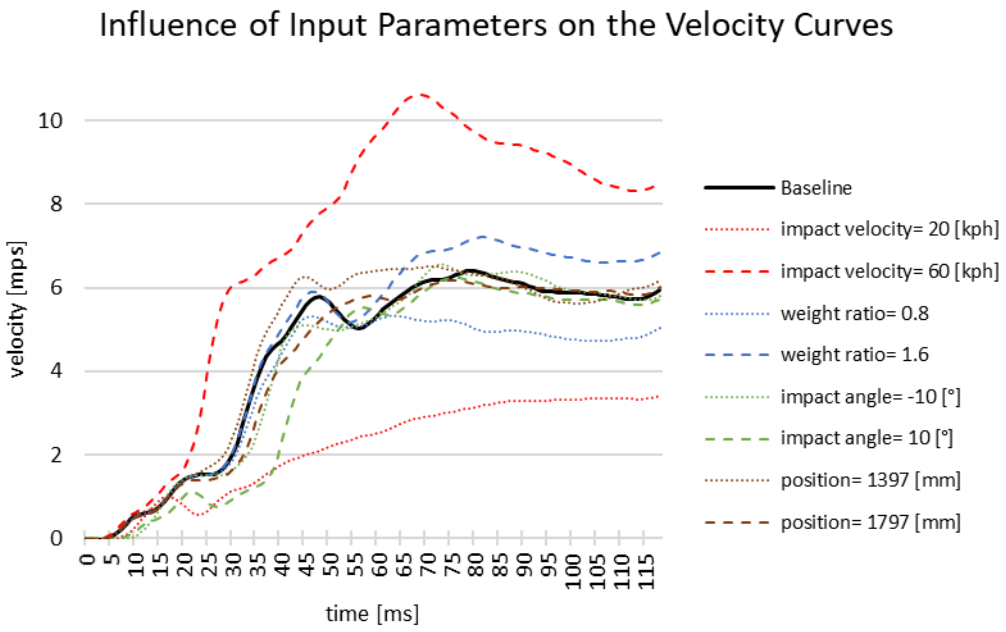

Figure 5-7 Influence of the input parameters on the vehicle velocity curves.

5.2.3 Output Parameter Definition

Due to the high number of influencing factors on the choice of representative output parameters, this step is nontrivial and needs a lot of analyzing and iterative steps. On the one hand, the choice of the output parameter has a significant impact on the meta-model type, and on the other hand, the chosen meta-model type is influencing the best suitable output parameters. Anyhow, to predict one output parameter, one meta-model is needed. Hence the number of meta-models depends on the number of output parameters. Simultaneously, the polynomial curve level that approximates the FEA intrusion and velocity sets the number of necessary output parameters and vice versa the goodness of the approximation.

A compromise can solve this problem. Polynomial approximations with a grade from three to six were considered and tested. The result was that an approximation with a degree of three is too inaccurate, while an approximation with degree five is very accurate but needs six boundary conditions. Hence the approximation with grade four was a good compromise between the accuracy of the approximation and complexity of the boundary conditions.

Five boundary conditions (output parameters) were needed to build a polynomial curve of grade four. The first output parameter was the start time X1 of the intrusion, mainly depending on the MDB position and angle. It had a significant impact on the curve shape, if a node was directly in contact with the barrier (force was applied diectly) or it was ‘pulled along’ by the door panel. The second and third output parameters were intrusion Y2 and the inclination k2 between the onset of intrusion and the maximum intrusion. The fourth and fifth output parameter were the maximum intrusion Y3 and the time at the maximum intrusion X3. The boundary conditions were defined as in Table 8 (Figure 5-8).

Table 8 Boundary conditions for the grade four polynomial curve.

Number	Boundary Condition
1	$Y_{(X1)} = 0$
2	$Y_{(\frac{X1+X3}{2})} = Y2$
3	$\frac{dY_{(\frac{X1+X3}{2})}}{dX} = k2$
4	$Y_{(X3)} = Y3$
5	$\frac{dY_{(X3)}}{dX} = 0$

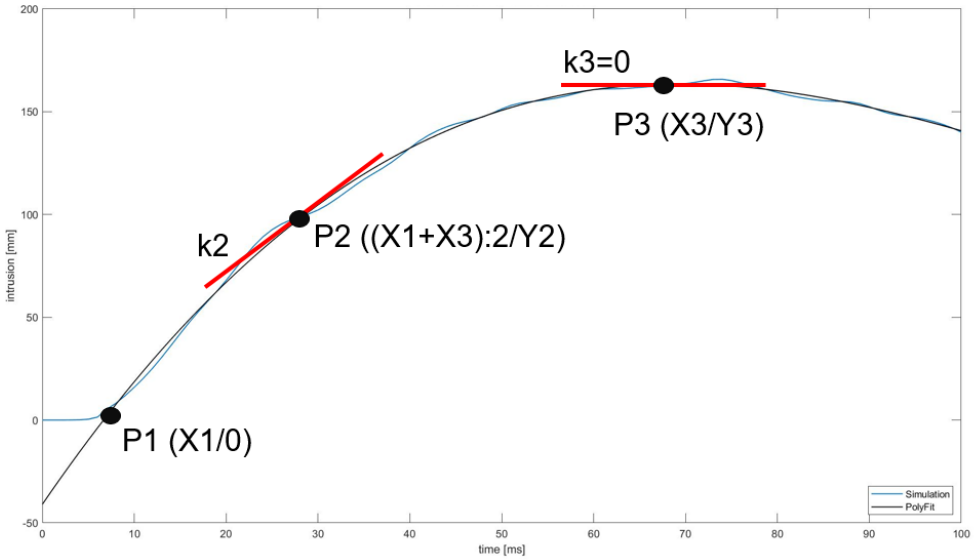

Figure 5-8 Boundary conditions for a fourth degree polynomial.

5.3 Input-Output Parameter Comparison

The output parameters are plotted against the input parameters to identify trends of the output parameter preparation method and possible errors. This is done exemplary for one node of Plane E (E_O). Additional information can be found in the appendix (A-6). For the following figures, the input parameters (weight ratio, impact velocity, impact

angle, position) are drawn in red, while the output parameters (X1-start of intrusion/velocity curve, X3-time at maximum intrusion/velocity, Y3-maximum intrusion/velocity, Y2-intrusion/velocity, K2 gradient at Y2) are drawn in blue. The input and output parameters are normalized by their maximum value. At the horizontal axis, the simulation number is shown.

5.3.1 Half Range Model

The input-output parameter comparison of the HRM is plotted in Figure 5-9. It consists of 81 input parameter combinations.

A correlation between X1 and the input-parameters impact angle and impact velocity was observed. X1 was quite independent of the other input parameters (weight ratio and position). The intrusion starting time of node E_O peaked for an impact angle of 10° and a position of 1797 mm and was around two to ten times higher than for other impact angles and positions. This was not observed for all nodes. Figure 5-10 shows the FEM setup for an impact angle of -10°. The reason for the different intrusion start could be related to the node's higher distance to the point of initial contact. Also, the stiffness of other involved parts could have influenced it. For the time at the maximum intrusion (X3) the value range was smaller than for X1. The minimum of X3 was around 60% of its maximum value. Furthermore, lots of fluctuations were observed which can be analyzed using those charts.

The intrusion values Y2 and Y3 were correlating with the impact velocity and weight ratio. However, also fluctuations occurred for different impact angles and positions. The incline K2 seems to have similar dependencies as Y2 and Y3, yet K2 showed more fluctuations which might have occurred due to the position variation. The intrusion values (Y2, K2, Y3) for an impact velocity of 60 kph were around three to ten times higher than for an impact velocity of 20 kph

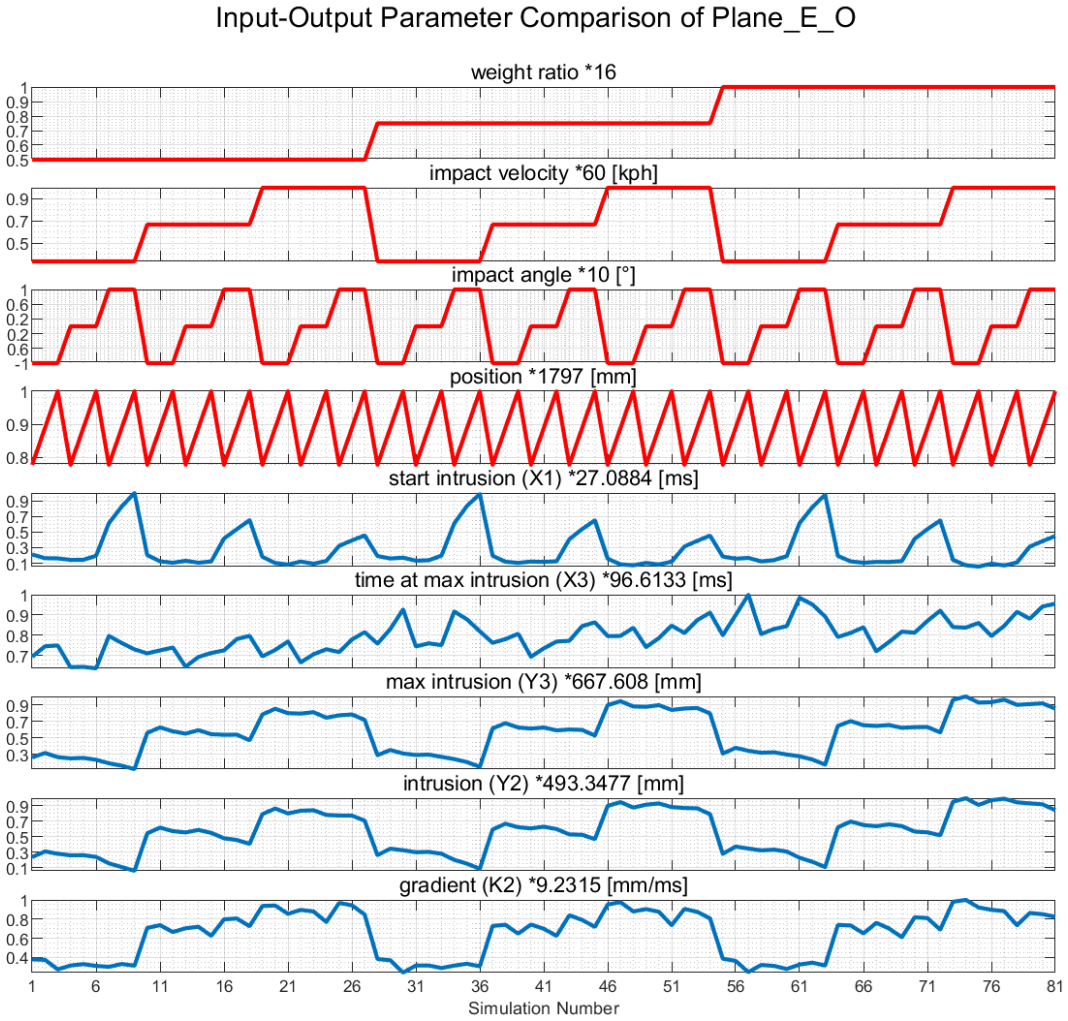

Figure 5-9 Input-Output parameter comparison for Plane E_O of the HRM.

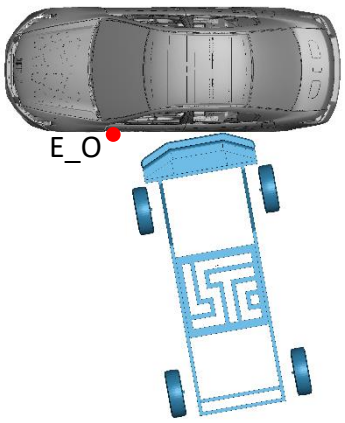

Figure 5-10 FEA with an impact angle of 10° and a position of 1797 mm.

5.3.2 Full Range Model

The input-output parameter comparison of the FRM is plotted in Figure 5-11. It consists of 81 input parameter combinations. For the FRM, similar dependencies as for the HRM were observed. Hence, a correlation between X1 and the input-parameters impact angle and impact velocity was observed. X1 was quite independent of the other input parameters (weight ratio and position). The intrusion starting time of node E_O has its peak at an impact angle of 20° and a position of 1997 mm. Values of X1 were around eight to ten times higher compared to other impact angles and positions. Therefore, a reduced influence of the impact velocity value and weight ratio value compared to the HRM were observed for this configuration (impact angle=20°, position=1997). The reason for the different intrusion start could be related to the node's higher distance to the point of initial contact (Figure 5-10). Also, the stiffness of other involved parts could have influenced it. For the time at the maximum intrusion (X3) the value range was smaller than for the start of intrusion (X1). The minimum of X3 was about 50% of its maximum value. Furthermore, lots of fluctuations were observed and no clear impact of the input variables was visible.

The intrusion values Y2 and Y3 were correlating with the velocity and weight ratio. However, also fluctuations occurred for different impact angles and positions. The incline K2 seems to have similar dependencies as Y2 and Y3, yet K2 showed more fluctuations that might be related to the position variation. The intrusion values (Y2, K2, Y3) for an impact velocity of 60 kph were around two to ten times higher than for an impact velocity of 20 kph.

However, for simulations with a combination of an impact angle between -20° and 20° and a position between 1197 mm and 1997 mm, the output parameter preparation method was not working optimally, since higher fluctuations occurred. For those parameter values the intrusion curves starts to change from the expected curve (Figure 5-12-A) to a curve with different shape (Figure 5-12-B).

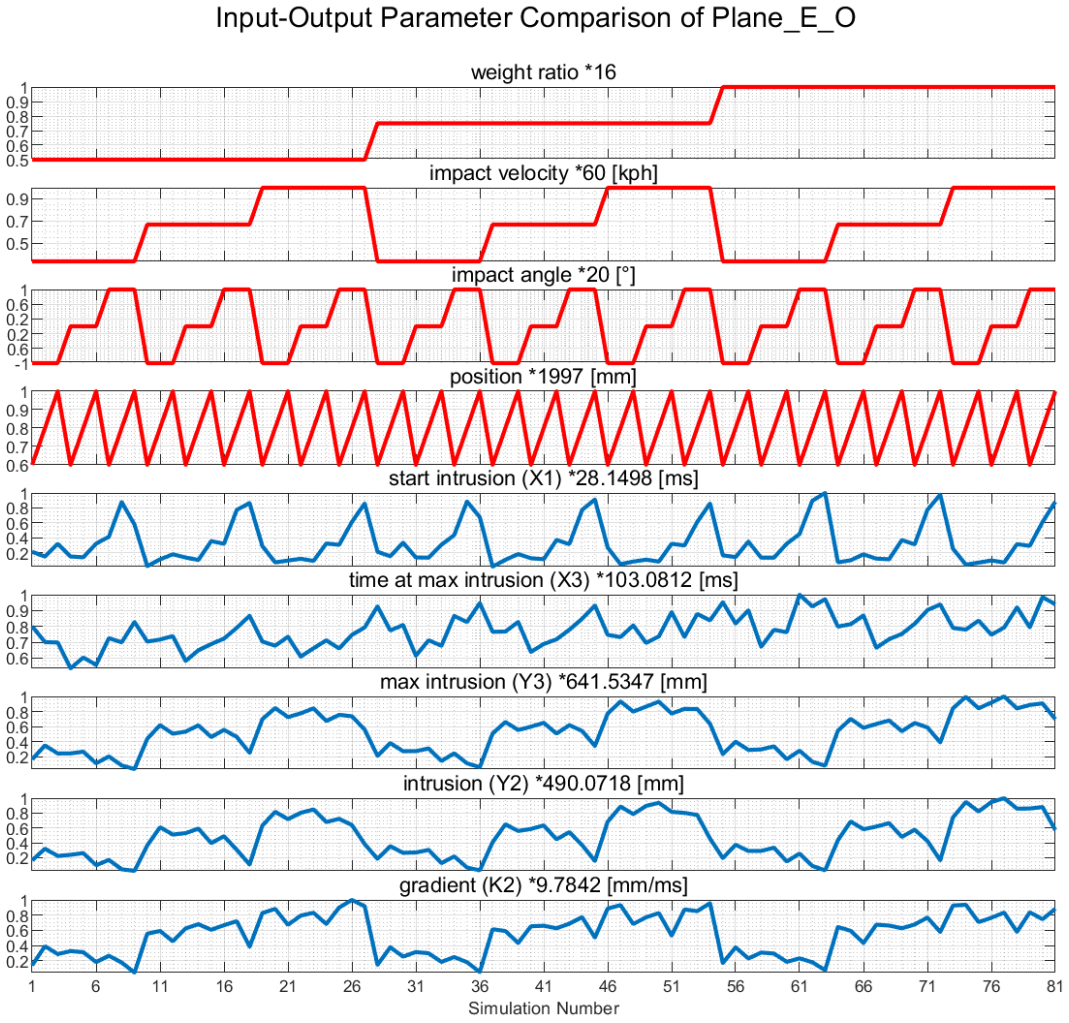

Figure 5-11 Input-Output parameter comparison for Plane E_O of the FRM.

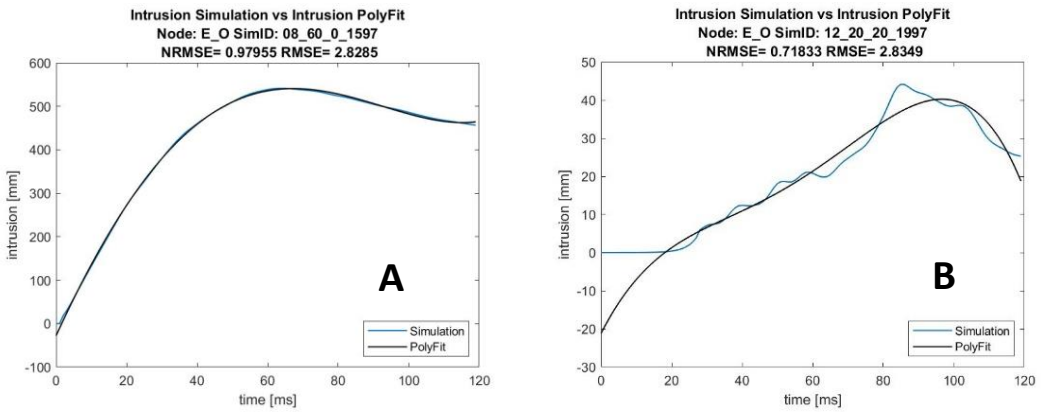

Figure 5-12 Change of the characteristics of the intrusion curve.

5.3.3 Focused Model

The input-output parameter comparison of the FM is It consists of 40 input parameter combinations. Since the FM was a combination of the HRM and the FRM similar effects were observed (Figure 5-13). Hence, a correlation between X1 and the input-parameters impact angle and impact velocity was observed. X1 was quite independent of the other input parameters (weight ratio and position). The intrusion starting time of node E_O peaks at an impact angle of 20° and a position of 1997 mm and was about eight to ten times higher than for other impact angles and positions. Therefore, a reduced influence of the impact velocity value and weight ratio value compared to the FRM was observed for this configuration (impact angle=20°, position=1997). The reason for the different intrusion start could be related to the node's higher distance to the point of initial contact (Figure 5-10). Also, the stiffness of other involved parts could have influenced X1. For the time at the maximum intrusion (X3) the value range was smaller than for the start of intrusion (X1). The minimum of X3 was about 50% smaller than its maximum value. Furthermore, lots of fluctuations were observed and no clear impact of the input variables was visible.

The intrusion values Y2 and Y3 were correlating with the impact velocity and weight ratio. However, also fluctuations occurred for different impact angles and positions. The incline K2 seems to have similar dependencies as Y2 and Y3. Yet, K2 showed more fluctuations that might have been caused by the position variation. The intrusion values (Y2, K2, Y3) for an impact velocity of 60 kph were around two to ten times higher than for an impact velocity of 20 kph.

However, for simulations with a combination of an impact angle between -20° and 20° and a position between 1197 mm and 1997 mm, the output parameter preparation method was not working optimally. The intrusion curves start to change its shape from the expected curve (Figure 5-12-A) to a curve with different shape (Figure 5-12-B).

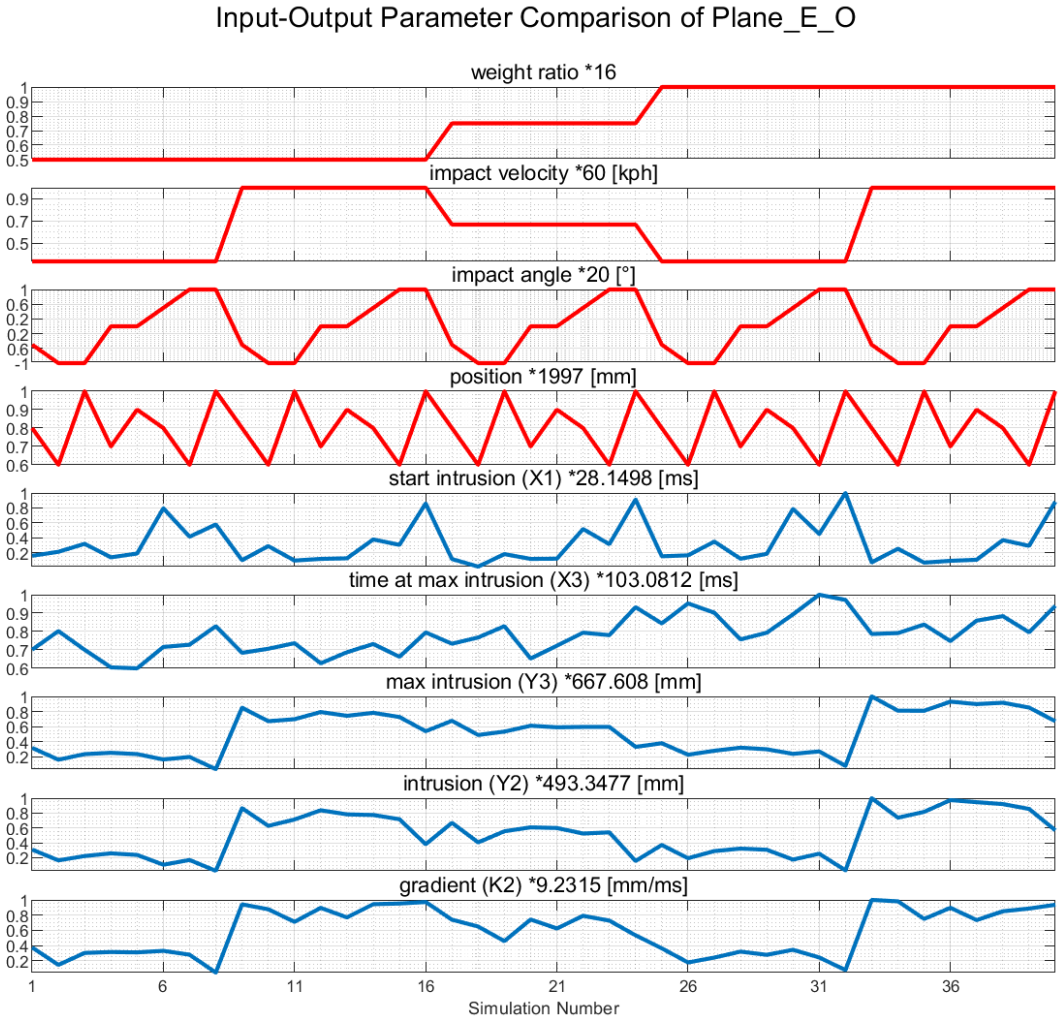

Figure 5-13 Input-Output parameter comparison for Plane E_O of the FM.

5.4 Error due to Rigid Plane Approximation

The NRMSE calculated for the three test points (Figure 4-7) points per plane is shown in Figure 5-14. An NRMSE of one indicates a perfect approximation. While six nodes reached a NRMSE above 0.9, six nodes were between 0.8 and 0.9. Five nodes had an NRMSE below 0.8. The planes A, C, D and E showed better approximations than B and F. Plane F had the worst approximation quality.

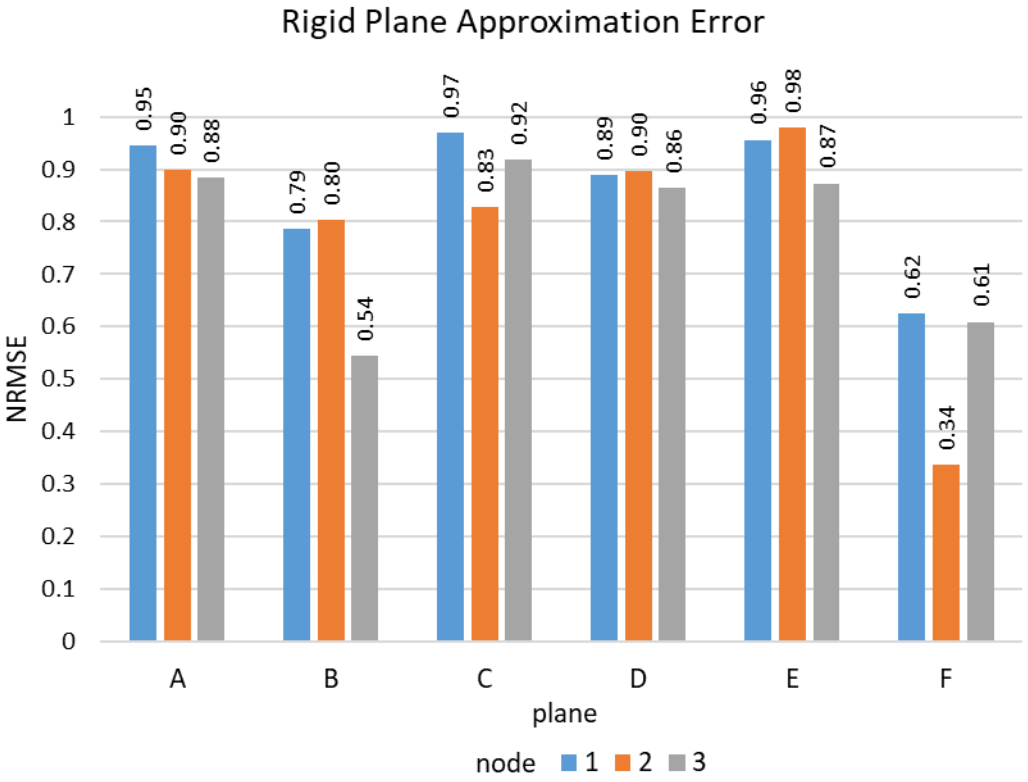

Figure 5-14 NRMSE of the rigid plane approximation.

5.5 Metamodeling

After all meta-models for each training set and each meta-model type were built, the selection was done by comparing the RRSE for the predicted output parameters. The validation set, consisting of 16 points, was used. The mean RRSE was calculated over all the validation points. As mentioned, a value of zero is a perfect prediction, while a value of one means that the simplest model would give the same prediction error. The best performing meta-models were the RBF models, followed by the GPML models and the

LSSVM models for all training sets. The Kriging models and Rational models were less suitable for this application. Noticeable is that the meta-models did not perform much better than the simplest model for time predictions. They perform much better than the simplest model for predicting the intrusion-based values Y3, Y2, and K2.

5.5.1 Half Range Model

The mean RRSE over all nodes, the velocity and over all output parameters was between 0.491 and 0.968 (Figure 5-15). For the time-related output parameters' predictions, it was observed that the meta-models were providing as good predictions as the simplest model. The parameters Y3, Y2, and K2, had much better prediction results over all model types than the simplest model. The best meta-models for the HRM were the RBF models (0.491) followed by the GPML models (0.511), the LSSVM models (0.516), the Rational models (0.820), and the Kriging models (0.968). Only for X1, the GPML models and LSSVM models performed slightly better than the RBF models. On average, all meta-models performed better than the simplest model.

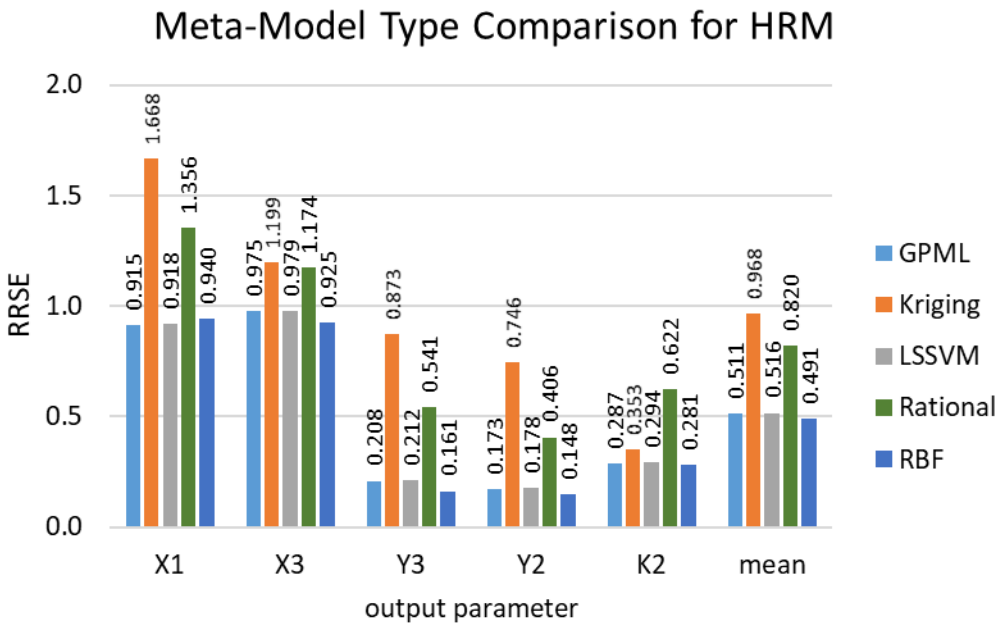

Figure 5-15 Average RRSE of the HRM over all nodes and the velocity.

5.5.2 Full Range Model

The mean RRSE over all nodes, the velocity and over all output parameters was between 0.628 and 1.615 (Figure 5-15). For the time-related output parameters' predictions, it was observed that the meta-models were providing not as good predictions as the simplest model. For the average RRSE over all output parameters, the RBF models (0.628) performed best. Furthermore, The RBF models performed best for all output parameters. While for the GPML models (0.674) and the LSSVM models (0.654), good results have been observed, the Kriging models (1.615) and the Rational models (1.009) performed on average worse than the simplest model.

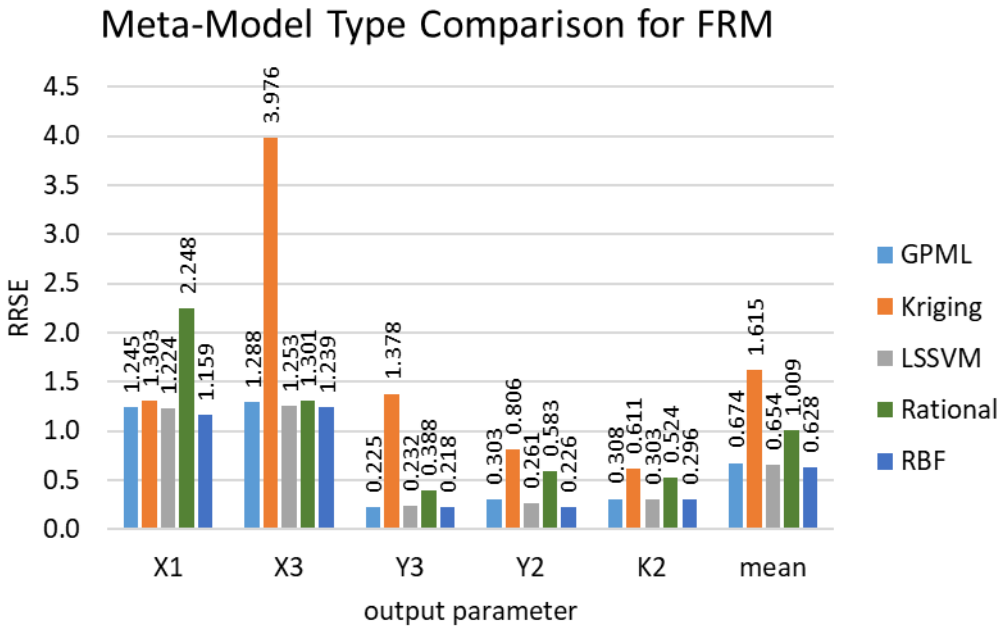

Figure 5-16 Average RRSE of the FRM over all nodes and the velocity.

5.5.3 Focused Model

The mean RRSE over all nodes, the velocity and over all output parameters was between 0.470 and 1.977 (Figure 5-17). RBF models (0.470) have performed best on average, followed by the GPML models (0.483), the LSSVM models (0.483), the Kriging models (1.415), and the Rational models (1.977). The RBF models were not the best models for every output parameter. For X3, the best performing meta-models were the LSSVM models, while for Y3, the Kriging models were best. However, for X1, Y2, and K2, the RBF models performed best.

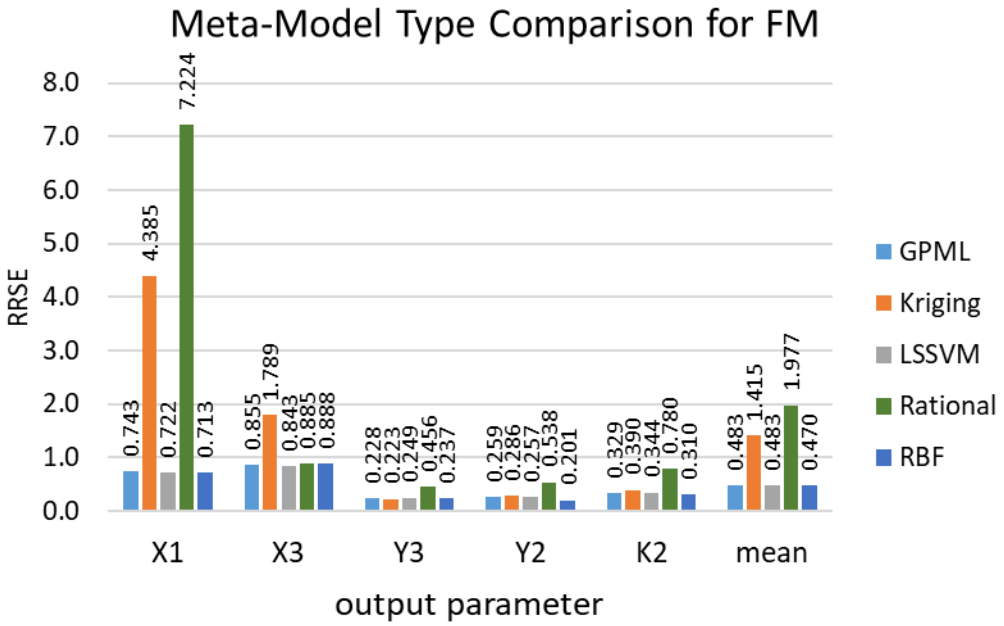

Figure 5-17 Average RRSE of the FM over all nodes and the velocity.

5.6 Meta-Model Validation

The RBF models' validation was done by predicting the intrusion and velocity curves for ten input parameter variations, the test set. The prediction was compared to the FEA result to calculate the NRMSE. The mean NRMSE of all intrusion and velocity curves was plotted, and the variance for the NRMSE was evaluated. A perfect fit is given by an NRMSE of one.

The mean NRMSE was between 0.518 and 0.620 (Figure 5-18), the FRM had the best prediction result, followed by the FM and the HRM. For Simulation number two, all meta-models had their best prediction accuracy combined with low variance. For simulation number one to six, the HRM, FRM, and FM had an NRMSE between 0.499 and 0.910. For simulation numbers seven to ten, the NRMSE was between -0.067 and 0.600. Furthermore, the variance for simulation numbers seven to ten increased.

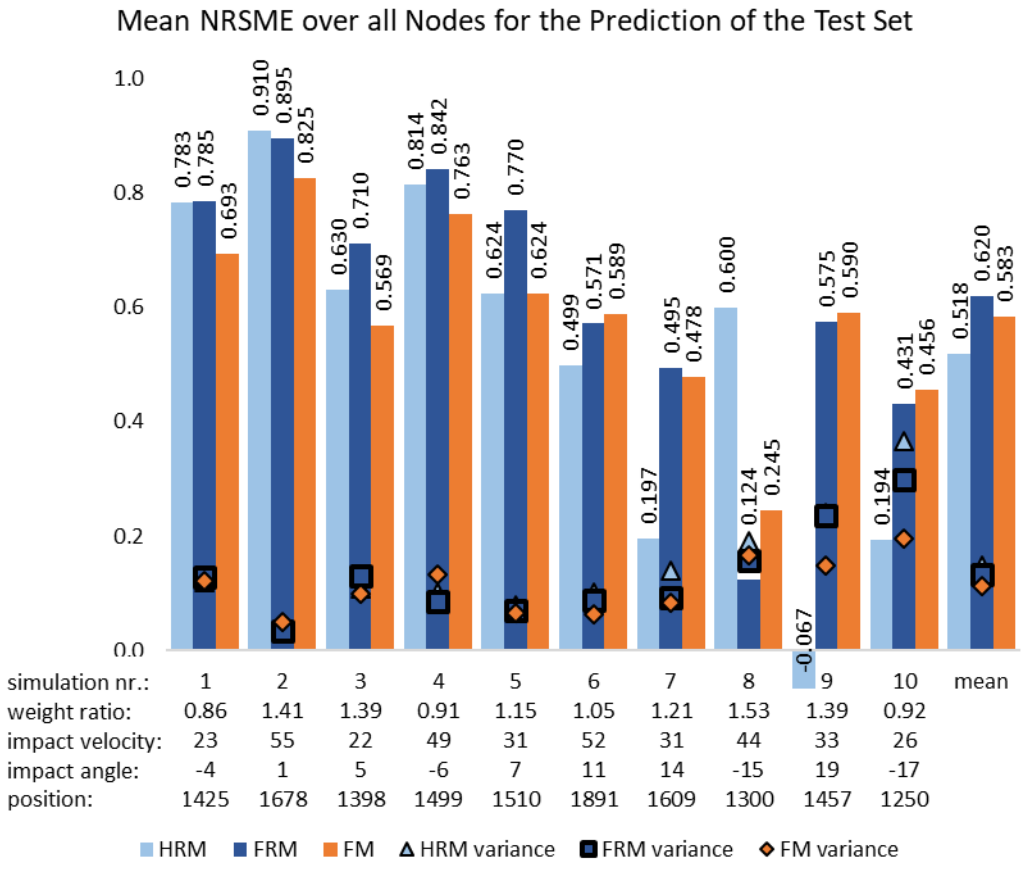

Figure 5-18 Prediction quality of the HRM, FRM and FM for the test set.

6 DISCUSSION

Input parameters

The IIHS and the Euro NCAP's side impact test represent one accident of many in the Real-World accident configuration. The chosen input parameter ranges for the impact velocity, and the weight ratio cover around 70% of the vehicles that experienced lateral loading in NASS CDS. Three out of four vehicles experienced lateral loading with a DOF1 between three and twelve o'clock. It can be assumed that both side impact participants in Real-World accidents have a longitudinal velocity. This could be the reason for the non-symmetrical distribution of the DOF1. Due to the assumption that the FEA's stuck vehicle has no impact velocity, the DOF1 has to be represented in another way. The intrusion curve starts changing its characteristics for impact angles of more than 20° or less than -20°. The higher the impact angle's absolute value, the more the impact becomes a glace-off. Therefore, for the FRM and FM, an impact angle range from -20° to 20° is a good compromise between avoiding a glacee-off and covering lots of accident configurations. For the HRM, a reduced range of -10° to 10° is set. The MDB position range is set from 1197 mm to 1997 mm for the FRM and FM and from 1397 mm to 1797 mm for the HRM. It was observed that for extreme values of the impact angle and the position, the fluctuations in the intrusion curves increased. This occurs especially when the node is not directly in contact with the MDB, means that it is not pushed directly by the MDB but pulled along with the other nodes. A Quite similar effect was observed when the crash turns more into a glace-off, which occurs for higher deviation from a perpendicluar stroke. The impact angle and the position showed a smaller effect on the velocity curves.

Output Parameters

The curve approximation's accuracy is quite different for each node and the velocity. It is the same for the FRM and the FM, yet it was better for the HRM. The difference between the HRM and the FRM is the input-parameter range regarding the impact angle and the impact position. It was observed that high absolute values for the impact angle tent to turn the impact to a glace-off. This glace-off intrusion curve is less likely to be represent by a grade four polynomial. Hence, the lower approximation accuracy could result from this. The best approximation accuracy for intrusion was observed for plane E. This could be related to the position of the plane. It is located in the middle of the lower plane row. Therefore, it is direct contact with the MDB in more simulations. The lowest accuracy is observed for plane A, which might be related to its position (upper front panel). Therefore, it is not as often in direct contact with the MDB than other planes. The velocity approximation has a lower accuracy than the intrusion approximation of the nodes. This might be related to the higher oscillating curve properties of the velocity, and therefore the polynomial grade might be too low.

The impact velocities influence on the intrusion depth and the gradient was observed. However, no clear influence on the starting time or maximum intrusion time was found. The weight ratio's relations to the maximum intrusion and its time were observed, yet neither the starting time nor the gradient was affected by the weight ratio. The impact angle had influence on all observed characteristics, except the gradient (K2) seems unaffected. The position showed an impact on all characteristics, yet the influence was not that high for the other input parameters. It has to be said that just the node E_O was observed, other nodes are assumed to have the same or at least similar characteristics, yet it might be that the input parameters' influence is stronger or weaker.

The velocity of the struck vehicle showed more fluctuation than the intrusion curves. For the first 20 ms, it is increasing moderately. After that, a high gradient was observed. This gradient might be very important for occupant simulation models. The striking vehicle's impact velocity had more influence on the gradient and the maximum velocity

than the other input parameters. A velocity reduction was observed after this high gradient for some input parameter configurations. This effect might be related to the stiffness of different involved parts and the first contact's elastic impulse. For a high velocity, this effect was not observed, yet the effect occurred for the weight ratio variation. The weight ratio showed an impact on the maximum velocity, while it did not influence the gradient clearly. The influence of impact angle and position on the maximum velocity was low, while there was an influence on the gradient and the curve's shape.

A fourth order polynomial curve was used to approximate the intrusion and velocity curves. The approximation with a grade three polynomial curve was too inaccurate, and the grade five polynomial curve would need more boundary conditions and hence more meta models. For the velocity, the same polynomial degree as for the intrusion was used. This might not be optimal for the intrusion velocity due to its higher fluctuations.

The input-output parameter comparison was done in detail for the node E_O. It was observed that the intrusion start time was higher for an impact angle of 10° (20°) and a position of 1797 (1997) mm. This correlates with the input parameter influence result. That applied to the HRM (FRM) input parameter range. This effect might be related to the node's relative position to the MDB. This might be one of the reasons why it was different for other nodes.

Metamodeling

The best performing meta-models were the RBF models, yet there was only a small difference between the GPML and LSSVM models. For the Kriging and Rational models, it can be said that they are less suitable for this application. For the intrusion time predictions (X1, X3), the simplest model is more accurate for the FRM, compared to all of the tested meta-model types. However, the HRM performs better than the simplest model, and the FM performs better than the HRM for those output parameters. No clear ranking of the test sets can be done for the other output parameters (Y3, Y2, K2). Over all output parameters, the FM performs best, followed by the HRM and the FRM. Anyhow the selected meta-model type for all parameters to be predicted was the RBF model.

The RBF meta-models were tested with the test set. The accuracy of the prediction was quite different for different input parameter values. For simulation, numbers six to ten, the input parameter range of the HRM was exceeded and except for simulation number six and eight the prediction worked poorly. The HRM did also not work better for simulation number one to five, where it was expected to do so, as the input parameters were within the range of the HRM. The FM model's performance is good, especially when it comes to variance. However, on average, it is less accurate than the FRM. The FRM had the best prediction accuracy of all models.

While the prediction works well for high impact velocities and impact angles close to zero, it works poorly for low velocities and increasing impact angles.

Noticeable is that predictions for an angle closer to zero provided higher accuracy and a smaller variance for all models.

7 CONCLUSION

The accuracy of the meta-model prediction depends on several approximations. Furthermore, the underlying FEM is quite complex due to the high number of parts and boundary conditions. Therefore, the approximation with a meta-model is limited and does not provide good accuracy. To increase the accuracy, a more detailed look into each node's properties is necessary. Therefore, the choice of the nodes defining the intrusion profile is important. It should be carefully considered which areas are necessary for an occupant simulation model. The lower the number of nodes, the easier it is to look into detail and adjust properties for each node.

For the input parameter range, special focus has to be put on impact angle and position. These input parameters affect the accuracy, because the structural parts involved in preventing intrusion and the load direction change. Due to the high complexity of the FEM, this has a tremendous impact on the FEA result, therefore also on the meta-model prediction. The impact velocity and the weight ratio affect the intrusion depth and the maximum intrusion time, not the main involved parts. Even if the load on some parts may increase or decrease, the involved parts do not change completely. Furthermore, the load direction is not changing. Reducing the range of impact angles and the position could help, yet it also decreases the represented number of Real-World accidents.

The most promising way to increase the accuracy would be a different DoE approach. The FM has shown that a similar result for the FRM is achieved although only 40 instead of 81 training points was used. Therefore, a space-filling DoE could increase the prediction quality.

Another way to increase the accuracy could be to increase the degree of polynomial. However, this also makes the approach more complex, and the expected advantages for the intrusion prediction limited. For the velocity prediction, it would be necessary to increase the degree of polynomial to allow for a better approximation.

The used input-output parameter comparison helps get an overview of all simulations. Furthermore, it can help to identify failed simulations or failed output preparation.

Extrapolating the input parameter ranges did not work well, as seen for the HRM. Furthermore, HRM did not provide higher accuracy than the FRM for the simulations that were within the HRM range.

When it comes to the meta-model type, GPML, LSSVM, and RBF models have shown good results, while Kriging and Rational models seem to be less suitable.

In this thesis, the result of the meta-model prediction quality is not satisfying. Considering the high effort to build the whole metamodeling process, it should be considered to use other methods to decrease the computational effort for the underlying FEM.

8 REFERENCES

[1] European health report 2018. More than numbers, evidence for all, WHO Regional Office for Europe, DK-2100 Copenhagen Ø, Denmark 2019

[2] Commission staff working document. EU road safety policy framework 2021-2030 - next steps towards "vision zero", European Commission, Brussels 2019

[3] Interim evaluation of the policy orientations on road safety 2011-2020. Luxembourg: Publications Office 2015

[4] Thomas P., M. Lerner, S. Niesen, R. Welsh, J. J. F.Commandeur, L. T. Aarts, T. J. Davidse a. N. Bos: Study on serious road traffic injuries in the EU. Luxembourg: Publications Office 2016

[5] Gregory A. Radja: National automotive sampling system – crashworthiness data system. analytical user manual 2015. Office of data acquisition national center for statistics and analysis national highway traffic safety administration (2016)

[6] Stevenson M., M. Segui-Gomez, I. Lescohier, C. Di Scala a. G. McDonald-Smith: An overview of the injury severity score and the new injury severity score. Injury prevention : journal of the International Society for Child and Adolescent Injury Prevention 7 (2001) 1, S. 10–13

[7] Joodaki H., B. Gepner a. J. Kerrigan: Leveraging machine learning for predicting human body model response in restraint design simulations. Computer methods in biomechanics and biomedical engineering (2020), S. 1–15

[8] Iraeus J., a. M. Lindquist: Development and validation of a generic finite element vehicle buck model for the analysis of driver rib fractures in real life nearside oblique frontal crashes. Accident; analysis and prevention 95 (2016) Pt A, S. 42–56

[9] Ye X., J. P.Gaewsky, L. E. Miller, D. A. Jones, M. E. Kelley, J. D. Suhey,B. Koya, A. A. Weaver a. J. D. Stitzel: Numerical investigation of driver lower extremity injuries in finite element frontal crash reconstruction. Traffic Injury Prevention 19 (2018) sup1, S21-S28

[10] Perez-Rapela D., J. L. Forman, S. H. Huddleston a. J. R. Crandall: Methodology for vehicle safety development and assessment accounting for occupant response

variability to human and non-human factors. Computer methods in biomechanics and biomedical engineering (2020), S. 1–16

[11] Laberge-Nadeau C., F. Bellavance, S. Messier, L. Vézina a. F. Pichette: Occupant injury severity from lateral collisions: a literature review. Journal of safety research 40 (2009) 6, S. 427–435

[12] Side impact mobile deformable barrier testing protocol version 8.1.2, European new car assessment programme, Belgium 2020

[13] Side Impact Test Protocol 2.0 (Version I), Insurance Institute for Highway Safety, 988 Dairy Rd, Ruckersville, VA 22968. 2020

[14] Arbelaez R., B. Baker and J. Nolan: Delta vs for IIHS side impact crash tests and their relationship to real-world crash severity. Insurance Institute for Highway Safety (2005)

[15] Bareiss M. and H. C. Gabler: Estimating near side crash injury risk in best performing passenger vehicles in the United States. Accident; analysis and prevention 138 (2020), S. 105434

[16] Liu C. and J. C. Pressley: Side impact motor vehicle crashes: driver, passenger, vehicle and crash characteristics for fatally and nonfatally-injured rear-seated adults. Injury epidemiology 3 (2016) 1, S. 23

[17] Zhao G., Y. Zhao and X. Li: Whole Car Side Impact Mode and Response Evaluation. Procedia Engineering 29 (2012), S. 2667–2671

[18] Iwamoto M., Y. Kisanuki, I. Watanabe, K. Furusu, K. Miki and J. Hasegawa: Development of a finite element model of the total human model for safety (THUMS) and application to Injury Reconstruction. IRCOBI 2002 (2002)

[19] Crash Injury Research-CIREN. National highway traffic safety administration

[20] Golman Adam J., K. A. Danelson, L. E. Miller and J. D. Stitzel: Injury prediction in a side impact crash using human body model simulation. Accident Analysis & Prevention 64 (2014), S. 1–8

[21] Singh H., V. Ganesan, J. Davies, M. Paramasuwom and Gradischnig: Vehicle interior and restraints modeling development of full vehicle finite element model

including vehicle interior and occupant restraints systems for occupant safety analysis using THOR dummies (2018)

[22] Grama A., V. Kumar, G. Karypis and A. Gupta: Introduction to parallel computing. New York, London: Addison-Wesley 2003

[23] John C. Steuben: Massively parallel engineering simulations ongraphics processors: parallelization,synchronization, and approximation, Colorado School of Mines Ph.D. Thesis. Golden, Colorado 2014

[24] White D. R., S. Saigal and S. J. Owen.: Meshing complexity: predicting meshing difficulty for single part CAD models. Engineering with Computers 21 (2005), S. 76–90

[25] Mounir H., A. Nizar and B. Abdelmajid: CAD model simplification using a removing details and merging faces technique for a FEM simulation. J Mech Sci Technol 26 (2012), S. 3539–3548

[26] Wu T., T. Kim, V. Bollapragada, D. Poulard, H. Chen, M. B. Panzer, J.L. Forman, J.R. Crandall a. B. Pipkorn: Evaluation of biofidelity of THUMS pedestrian model under a whole-body impact conditions with a generic sedan buck. Traffic Injury Prevention 18 (2017) sup1, S148-S154

[27] Forman J., H. Joodaki, A. Forghani, P. Riley, V. Bollapragada, D. Lessley, B. Overby, S. Heltzel, J. Kerrigan, J. Crandall, S. Yarboro a. D. Weiss: Whole-body Response for Pedestrian Impact with a Generic Sedan Buck. Stapp Car Crash Journal 59 (2015), S. 401–444

[28] Suzuki S., Y. Takahashi, M. Okamoto, R Fredriksson, S. Oda: Validation of a pedestrian sedan buck using a human finite element model

[29] Alizadeh R., J. K. Allen a. F. Mistree: Managing computational complexity using surrogate models: a critical review, Bd. 31. Springer-Verlag London Ltd. 2020

[30] Simpson T. W., J.D. Peplinski, P. N. Koch and J. K. Allen: Metamodels for computer-based engineering design: survey and recommendations. Engineering with Computers 17 (2001) 2, S. 129–150

[31] Jian L., R. Alizadeh, J. Hao, G. Wang, J. K. Allen and F. Mistree: A rule-based method for automated surrogate model selection. Advanced Engineering Informatics 45 (2020)

[32] Burg H. and A. Moser: Handbuch verkehrsunfallrekonstruktion. unfallaufnahme, fahrdynamik, simulation. ATZ/MTZ-Fachbuch. 2017

[33] Gross D., W. Hauger, J. Schröder and W. A. Wall: Technische Mechanik. Kinetik. Technische Mechanik, Band 3, Ed. 9. Berlin: Springer 2006

[34] Sunnevång C., E. Rosén, O. Boström and U. Lechelt: Thoracic injury risk as a function of crash severity - car-to-car side impact tests with WorldSID compared to real-life crashes. Annals of advances in automotive medicine / Annual Scientific Conference 54 (2010), S. 159–168

[35] Gorissen D., I. Couckuyt and P. Demeester: A Surrogate modeling and adaptive sampling toolbox for computer based design (2010)

[36] Gorissen D., I Couckuyt, E. Laermans and T. Dhaene: Multiobjective global surrogate modeling, dealing with the 5-percent problem. Engineering with Computers 26 (2010) 1, S. 81–98

[37] Gorissen D., T. Dhaene and F. De Turck: Evolutionary model type selection for global surrogate modeling (2009)

[38] Dirk Gorissen: Heterogeneous evolution of surrogate models, Katholieke universiteit Leuven Master's Thesis. Leuven, Belgium 2007

[39] Shan S. and G.G. Wang: Survey of modeling and optimization strategies to solve high-dimensional design problems with computationally-expensive black-box functions. Structural and Multidisciplinary Optimization 41 (2010) 2, S. 219–241

[40] Broomhead D. and D. Lowe: Multivariable Functional Interpolation and Adaptive Networks. Complex Syst 2 (1988)

[41] Iooss B., L. Boussouf, A. Marrel and V. Feuillard: Numerical study of algorithms for metamodel construction and validation. 2009

[42] Vapnik Vladimir N.: The Nature of Statistical Learning Theory. New York, NY: Springer New York 2000

[43] Suykens J.A.K. and J. Vandewalle: Least Squares Support Vector Machine Classifiers. Neural Processing Letters 9 (1999) 3, S. 293–300

[44] Zhong Y., J. Tang, X. Li, B. Gao, H. Qian and W. Huaqiang: Dynamic memristor-based reservoir computing for high-efficiency temporal signal processing. Nature communications 12 (2021) 1, S. 408

[45] Kokla M., J. Virtanen, M. Kolehmainen, J. Paananen a. K. Hanhineva: Random forest-based imputation outperforms other methods for imputing LC-MS metabolomics data: a comparative study. BMC bioinformatics 20 (2019) 1, S. 492

[46] Jiang R., W. He, L. He, J. A. Yang, B. Qian, W. Zhou, P. He: Modelling adaptation strategies to reduce adverse impacts of climate change on maize cropping system in Northeast China. Scientific reports 11 (2021) 1, S. 810

A APPENDIX

A.1 Simulation Sets

Table Appendix 1 Input parameter variations for the training set of the HRM.

Simulation ID	weight ratio	impact velocity [kph]	angle [°]	position [mm]	FRM	HRM	FM
1	0.8	20	0	1397		x	x
2	0.8	20	0	1597	x	x	
3	0.8	20	0	1797		x	x
4	0.8	20	10	1397		x	
5	0.8	20	-10	1397		x	
6	0.8	20	10	1597		x	x
7	0.8	20	-10	1597		x	x
8	0.8	20	10	1797		x	
9	0.8	20	-10	1797		x	
10	0.8	40	0	1397		x	
11	0.8	40	0	1597	x	x	
12	0.8	40	0	1797		x	
13	0.8	40	10	1397		x	
14	0.8	40	-10	1397		x	
15	0.8	40	10	1597		x	
16	0.8	40	-10	1597		x	
17	0.8	40	10	1797		x	
18	0.8	40	-10	1797		x	
19	0.8	60	0	1397		x	x
20	0.8	60	0	1597	x	x	
21	0.8	60	0	1797		x	x
22	0.8	60	10	1397		x	
23	0.8	60	-10	1397		x	
24	0.8	60	10	1597		x	x
25	0.8	60	-10	1597		x	x
26	0.8	60	10	1797		x	
27	0.8	60	-10	1797		x	
28	1.2	20	0	1397		x	
29	1.2	20	0	1597	x	x	
30	1.2	20	0	1797		x	
31	1.2	20	10	1397		x	
32	1.2	20	-10	1397		x	
33	1.2	20	10	1597		x	
34	1.2	20	-10	1597		x	
35	1.2	20	10	1797		x	
36	1.2	20	-10	1797		x	
37	1.2	40	0	1397		x	x
38	1.2	40	0	1597	x	x	
39	1.2	40	0	1797		x	x
40	1.2	40	10	1397		x	

Appendix

41	1.2	40	-10	1397		x		
42	1.2	40	10	1597		x		x
43	1.2	40	-10	1597		x		x
44	1.2	40	10	1797		x		
45	1.2	40	-10	1797		x		
46	1.2	60	0	1397		x		
47	1.2	60	0	1597	x	x		
48	1.2	60	0	1797		x		
49	1.2	60	10	1397		x		
50	1.2	60	-10	1397		x		
51	1.2	60	10	1597		x		
52	1.2	60	-10	1597		x		
53	1.2	60	10	1797		x		
54	1.2	60	-10	1797		x		
55	1.6	20	0	1397		x		x
56	1.6	20	0	1597	x	x		
57	1.6	20	0	1797		x		x
58	1.6	20	10	1397		x		
59	1.6	20	-10	1397		x		
60	1.6	20	10	1597		x		x
61	1.6	20	-10	1597		x		x
62	1.6	20	10	1797		x		
63	1.6	20	-10	1797		x		
64	1.6	40	0	1397		x		
65	1.6	40	0	1597	x	x		
66	1.6	40	0	1797		x		
67	1.6	40	10	1397		x		
68	1.6	40	-10	1397		x		
69	1.6	40	10	1597		x		
70	1.6	40	-10	1597		x		
71	1.6	40	10	1797		x		
72	1.6	40	-10	1797		x		
73	1.6	60	0	1397		x		x
74	1.6	60	0	1597	x	x		
75	1.6	60	0	1797		x		x
76	1.6	60	10	1397		x		
77	1.6	60	-10	1397		x		
78	1.6	60	10	1597		x		x
79	1.6	60	-10	1597		x		x
80	1.6	60	10	1797		x		
81	1.6	60	-10	1797		x		
82	0.8	20	0	1197	x			
83	0.8	20	0	1997	x			
84	0.8	20	20	1197	x			x
85	0.8	20	-20	1197	x			x

Appendix

86	0.8	20	20	1597	x		
87	0.8	20	-20	1597	x		
88	0.8	20	20	1997	x		x
89	0.8	20	-20	1997	x		x
90	0.8	40	0	1197	x		
91	0.8	40	0	1997	x		
92	0.8	40	20	1197	x		
93	0.8	40	-20	1197	x		
94	0.8	40	20	1597	x		
95	0.8	40	-20	1597	x		
96	0.8	40	20	1997	x		
97	0.8	40	-20	1997	x		
98	0.8	60	0	1197	x		
99	0.8	60	0	1997	x		
100	0.8	60	20	1197	x		x
101	0.8	60	-20	1197	x		x
102	0.8	60	20	1597	x		
103	0.8	60	-20	1597	x		
104	0.8	60	20	1997	x		x
105	0.8	60	-20	1997	x		x
106	1.2	20	0	1197	x		
107	1.2	20	0	1997	x		
108	1.2	20	20	1197	x		
109	1.2	20	-20	1197	x		
110	1.2	20	20	1597	x		
111	1.2	20	-20	1597	x		
112	1.2	20	20	1997	x		
113	1.2	20	-20	1997	x		
114	1.2	40	0	1197	x		
115	1.2	40	0	1997	x		
116	1.2	40	20	1197	x		x
117	1.2	40	-20	1197	x		x
118	1.2	40	20	1597	x		
119	1.2	40	-20	1597	x		
120	1.2	40	20	1997	x		x
121	1.2	40	-20	1997	x		x
122	1.2	60	0	1197	x		
123	1.2	60	0	1997	x		
124	1.2	60	20	1197	x		
125	1.2	60	-20	1197	x		
126	1.2	60	20	1597	x		
127	1.2	60	-20	1597	x		
128	1.2	60	20	1997	x		
129	1.2	60	-20	1997	x		
130	1.6	20	0	1197	x		

Appendix

131	1.6	20	0	1997	x		
132	1.6	20	20	1197	x		x
133	1.6	20	-20	1197	x		x
134	1.6	20	20	1597	x		
135	1.6	20	-20	1597	x		
136	1.6	20	20	1997	x		x
137	1.6	20	-20	1997	x		x
138	1.6	40	0	1197	x		
139	1.6	40	0	1997	x		
140	1.6	40	20	1197	x		
141	1.6	40	-20	1197	x		
142	1.6	40	20	1597	x		
143	1.6	40	-20	1597	x		
144	1.6	40	20	1997	x		
145	1.6	40	-20	1997	x		
146	1.6	60	0	1197	x		
147	1.6	60	0	1997	x		
148	1.6	60	20	1197	x		x
149	1.6	60	-20	1197	x		x
150	1.6	60	20	1597	x		
151	1.6	60	-20	1597	x		
152	1.6	60	20	1997	x		x
153	1.6	60	-20	1997	x		x

A.2 Input-Output Parameters Comparison FRM

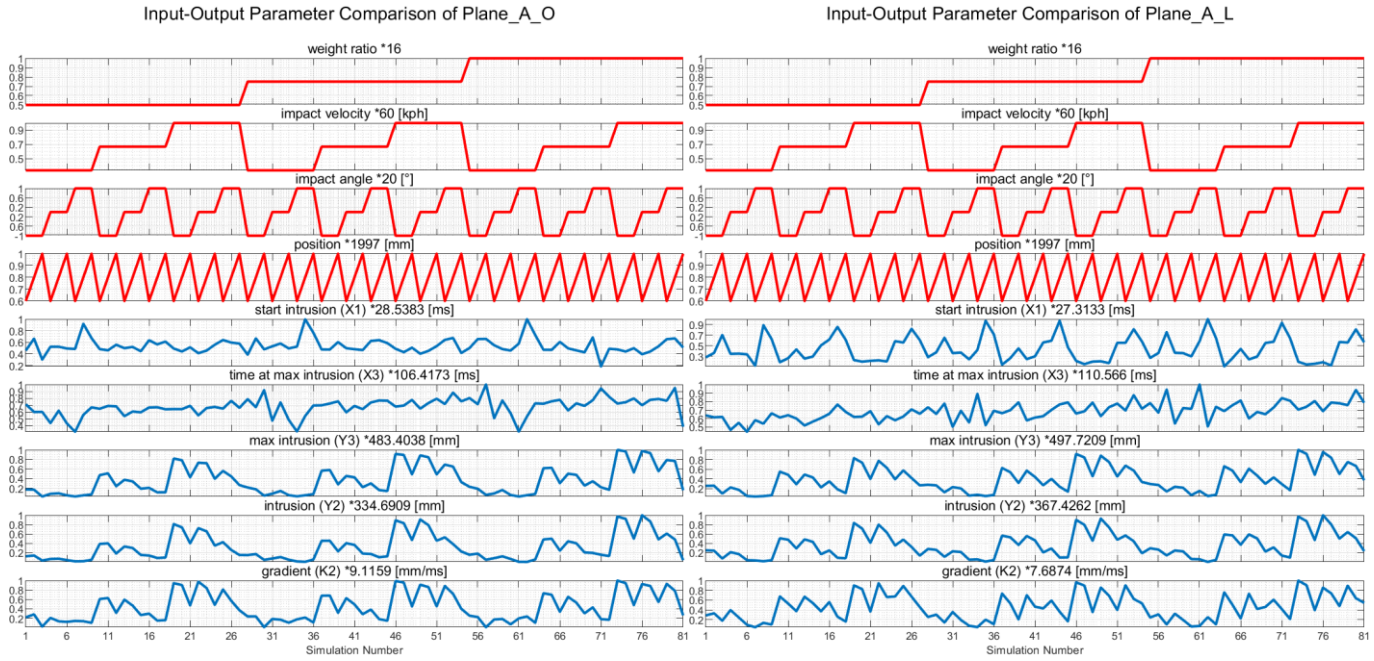

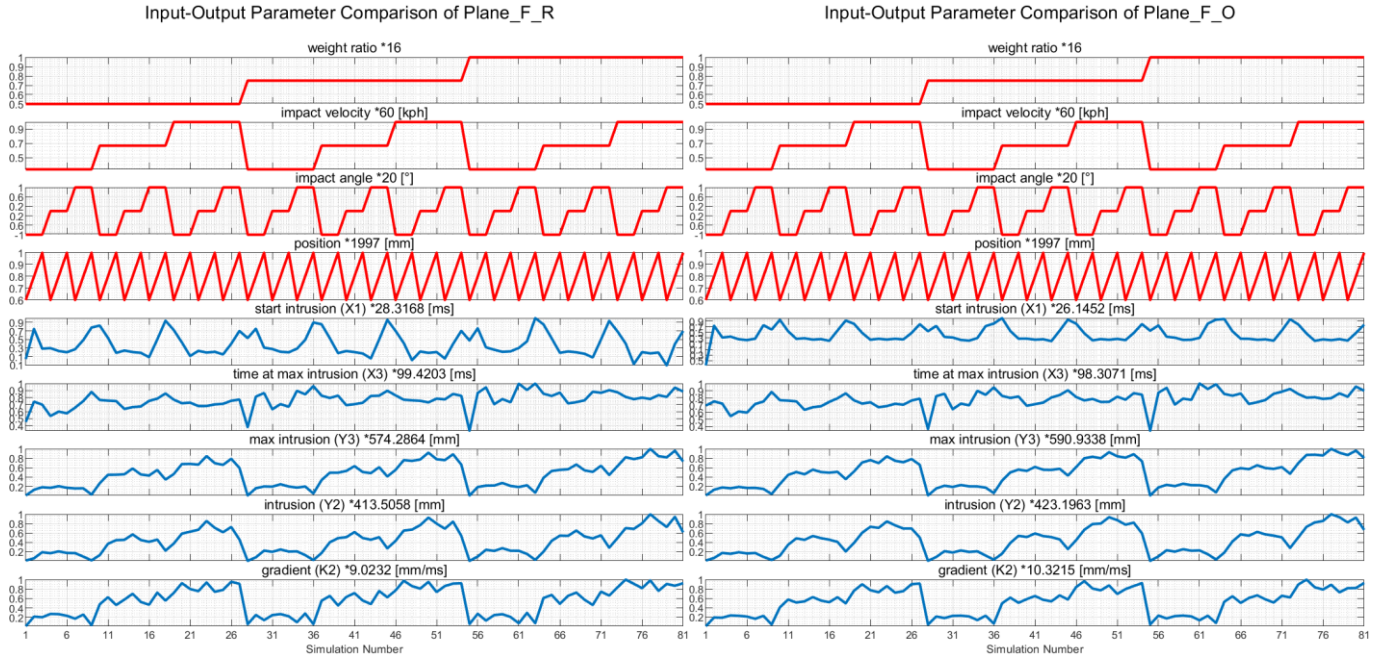

Appendix

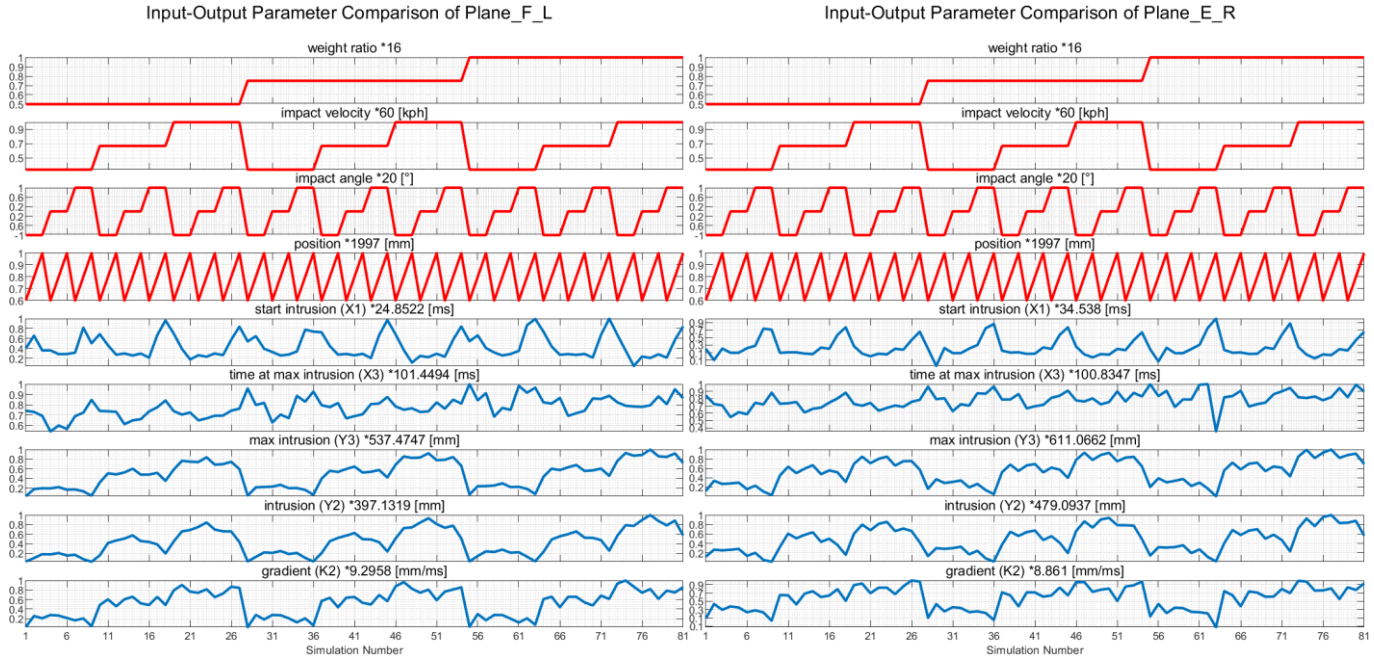
Input-Output Parameter Comparison of Plane_F_L
weight ratio *16
impact velocity *60 [kph]
impact angle *20 [°]
position *1997 [mm]
start intrusion (X1) *24.8522 [ms]
time at max intrusion (X3) *101.4494 [ms]
max intrusion (Y3) *537.4747 [mm]
intrusion (Y2) *397.1319 [mm]
gradient (K2) *9.2958 [mm/ms]
Simulation Number
Input-Output Parameter Comparison of Plane_E_R
weight ratio *16
impact velocity *60 [kph]
impact angle *20 [°]
position *1997 [mm]
start intrusion (X1) *34.538 [ms]
time at max intrusion (X3) *100.8347 [ms]
max intrusion (Y3) *611.0662 [mm]
intrusion (Y2) *479.0937 [mm]
gradient (K2) *8.861 [mm/ms]
Simulation Number

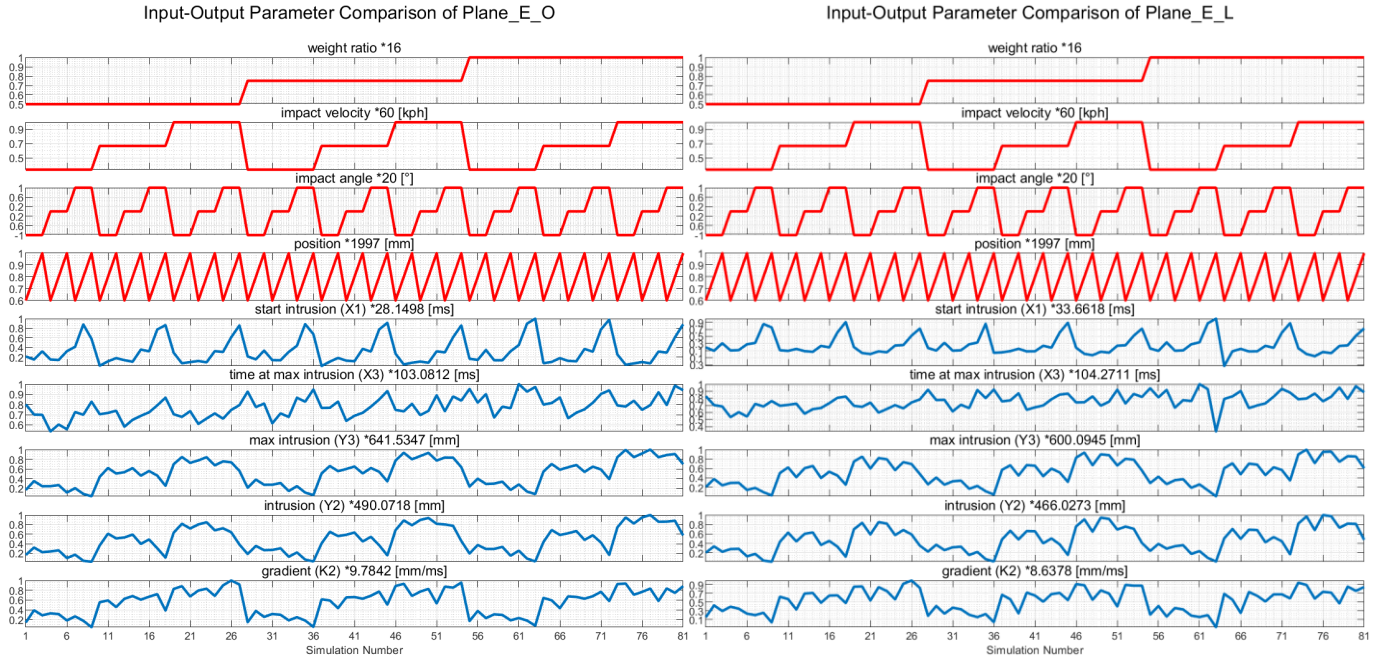
Input-Output Parameter Comparison of Plane_E_O
weight ratio *16
impact velocity *60 [kph]
impact angle *20 [°]
position *1997 [mm]
start intrusion (X1) *28.1498 [ms]
time at max intrusion (X3) *103.0812 [ms]
max intrusion (Y3) *641.5347 [mm]
intrusion (Y2) *490.0718 [mm]
gradient (K2) *9.7842 [mm/ms]
Simulation Number
Input-Output Parameter Comparison of Plane_E_L
weight ratio *16
impact velocity *60 [kph]
impact angle *20 [°]
position *1997 [mm]
start intrusion (X1) *33.6618 [ms]
time at max intrusion (X3) *104.2711 [ms]
max intrusion (Y3) *600.0945 [mm]
intrusion (Y2) *466.0273 [mm]
gradient (K2) *8.6378 [mm/ms]
Simulation Number

Appendix

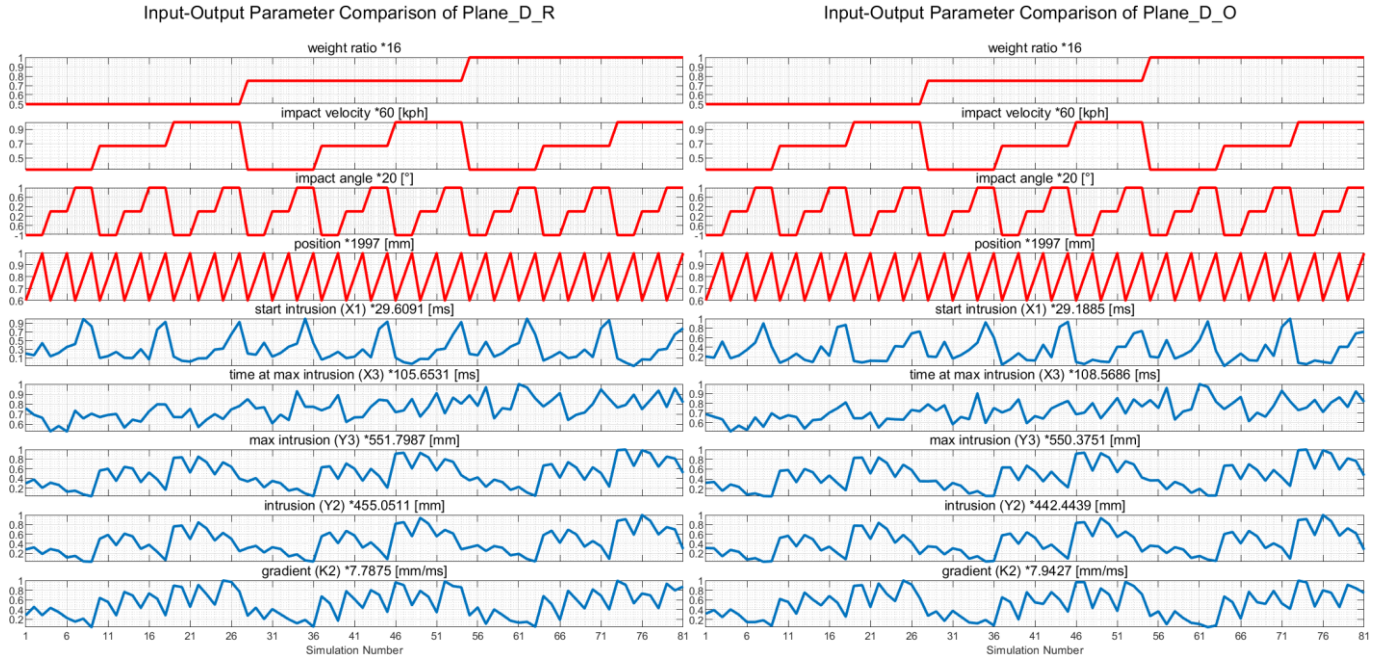
Input-Output Parameter Comparison of Plane_D_R
weight ratio *16
impact velocity *60 [kph]
impact angle *20 [°]
position *1997 [mm]
start intrusion (X1) *29.6091 [ms]
time at max intrusion (X3) *105.6531 [ms]
max intrusion (Y3) *551.7987 [mm]
intrusion (Y2) *455.0511 [mm]
gradient (K2) *7.7875 [mm/ms]
Simulation Number
Input-Output Parameter Comparison of Plane_D_O
weight ratio *16
impact velocity *60 [kph]
impact angle *20 [°]
position *1997 [mm]
start intrusion (X1) *29.1885 [ms]
time at max intrusion (X3) *108.5686 [ms]
max intrusion (Y3) *550.3751 [mm]
intrusion (Y2) *442.4439 [mm]
gradient (K2) *7.9427 [mm/ms]
Simulation Number

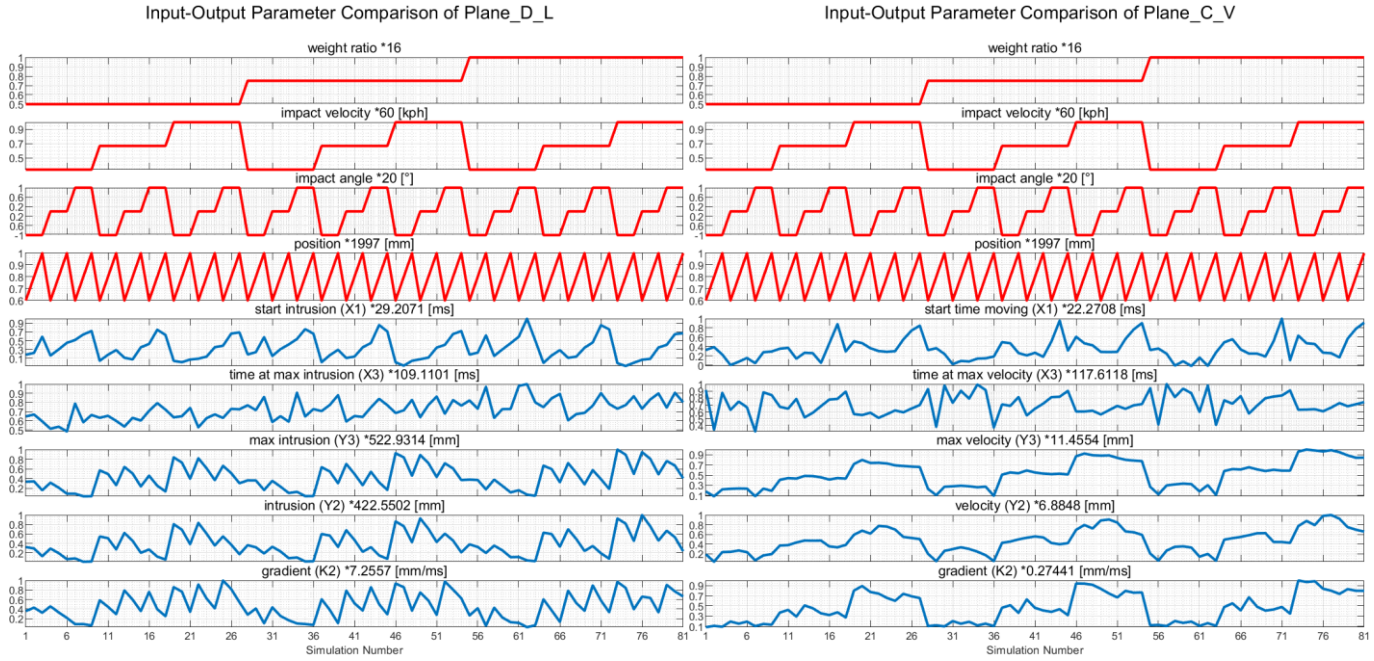
Input-Output Parameter Comparison of Plane_D_L
weight ratio *16
impact velocity *60 [kph]
impact angle *20 [°]
position *1997 [mm]
start intrusion (X1) *29.2071 [ms]
time at max intrusion (X3) *109.1101 [ms]
max intrusion (Y3) *522.9314 [mm]
intrusion (Y2) *422.5502 [mm]
gradient (K2) *7.2557 [mm/ms]
Simulation Number
Input-Output Parameter Comparison of Plane_C_V
weight ratio *16
impact velocity *60 [kph]
impact angle *20 [°]
position *1997 [mm]
start time moving (X1) *22.2708 [ms]
time at max velocity (X3) *117.6118 [ms]
max velocity (Y3) *11.4554 [mm]
velocity (Y2) *6.8848 [mm]
gradient (K2) *0.27441 [mm/ms]
Simulation Number

Appendix

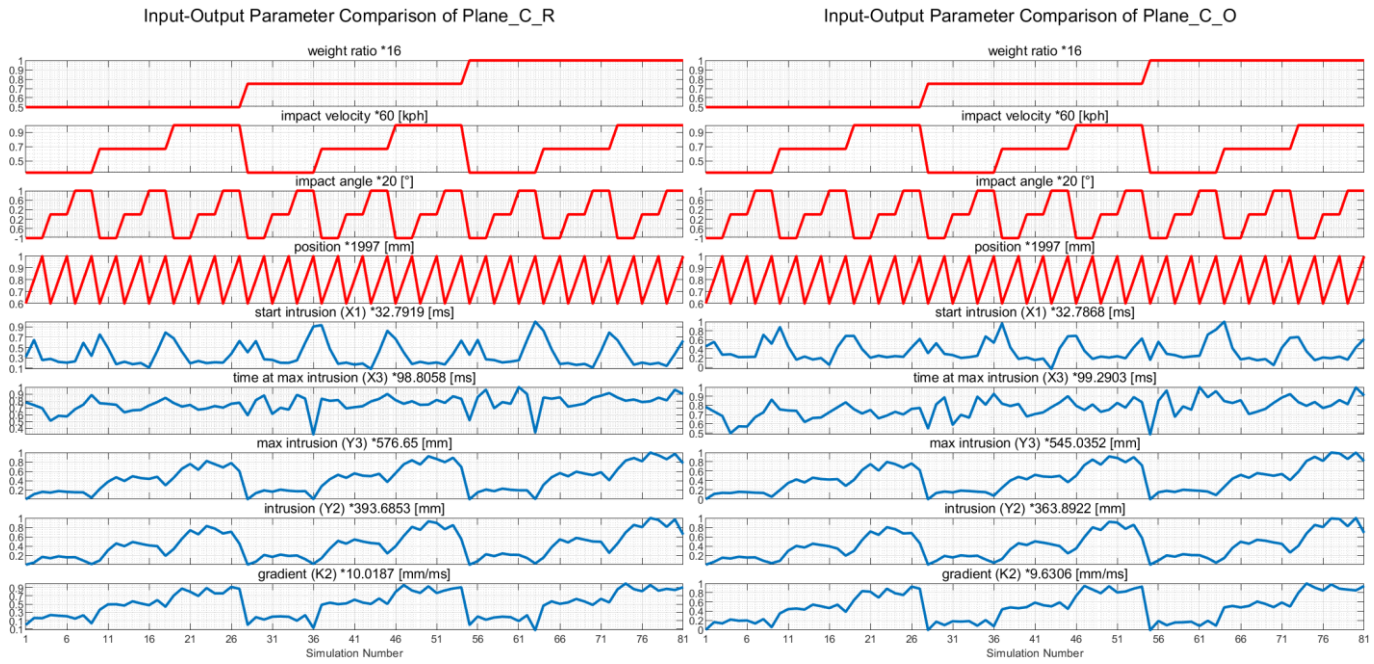
Input-Output Parameter Comparison of Plane_C_R
weight ratio *16
impact velocity *60 [kph]
impact angle *20 [°]
position *1997 [mm]
start intrusion (X1) *32.7919 [ms]
time at max intrusion (X3) *98.8058 [ms]
max intrusion (Y3) *576.65 [mm]
intrusion (Y2) *393.6853 [mm]
gradient (K2) *10.0187 [mm/ms]
Simulation Number

Input-Output Parameter Comparison of Plane_C_O
weight ratio *16
impact velocity *60 [kph]
impact angle *20 [°]
position *1997 [mm]
start intrusion (X1) *32.7868 [ms]
time at max intrusion (X3) *99.2903 [ms]
max intrusion (Y3) *545.0352 [mm]
intrusion (Y2) *363.8922 [mm]
gradient (K2) *9.6306 [mm/ms]
Simulation Number

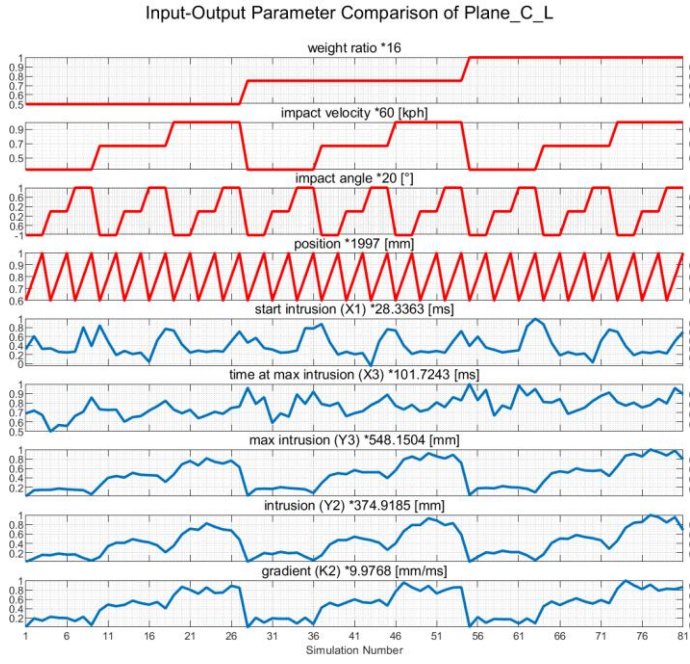
Input-Output Parameter Comparison of Plane_C_L
weight ratio *16
impact velocity *60 [kph]
impact angle *20 [°]
position *1997 [mm]
start intrusion (X1) *28.3363 [ms]
time at max intrusion (X3) *101.7243 [ms]
max intrusion (Y3) *548.1504 [mm]
intrusion (Y2) *374.9185 [mm]
gradient (K2) *9.9768 [mm/ms]
Simulation Number

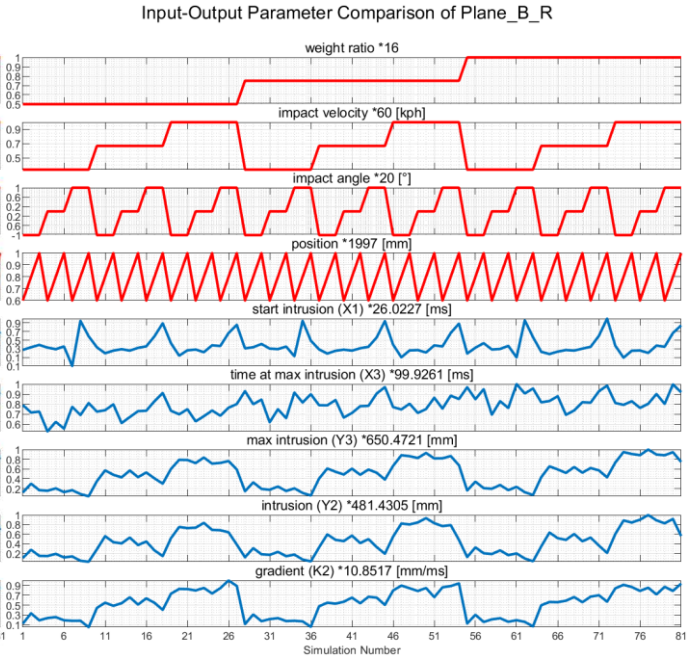
Input-Output Parameter Comparison of Plane_B_R
weight ratio *16
impact velocity *60 [kph]
impact angle *20 [°]
position *1997 [mm]
start intrusion (X1) *26.0227 [ms]
time at max intrusion (X3) *99.9261 [ms]
max intrusion (Y3) *650.4721 [mm]
intrusion (Y2) *481.4305 [mm]
gradient (K2) *10.8517 [mm/ms]
Simulation Number

Appendix

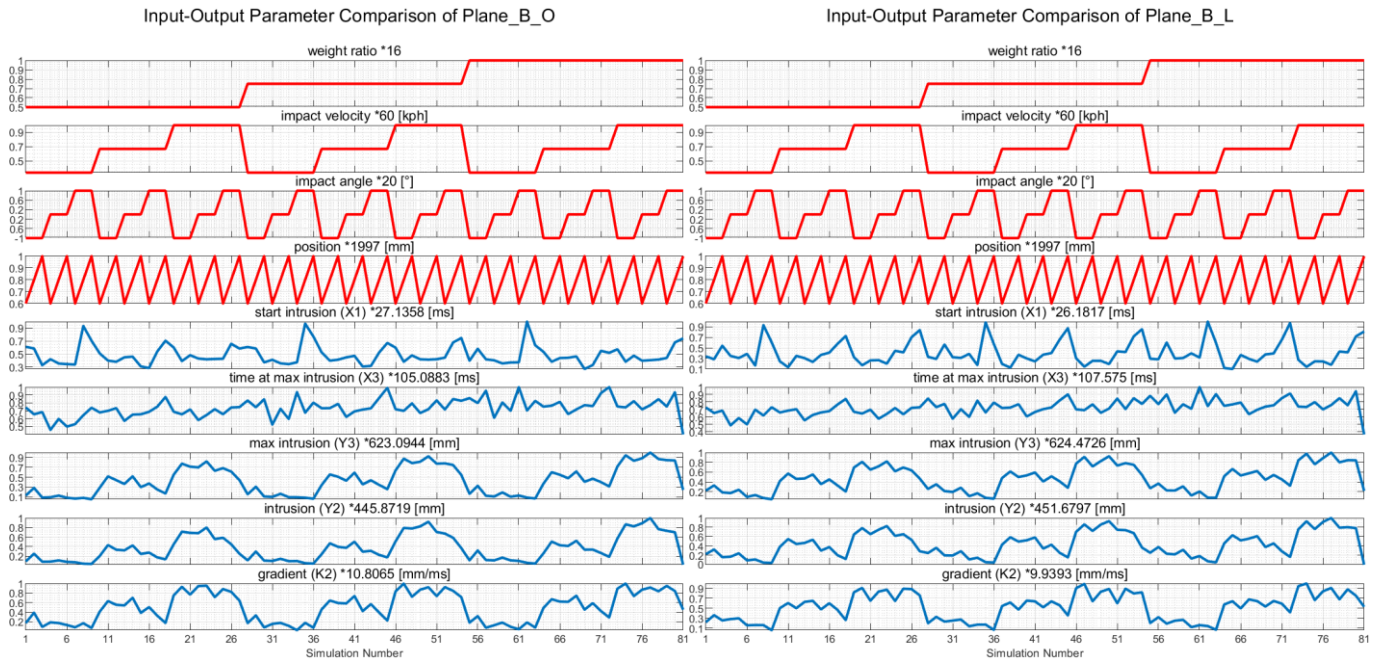
Input-Output Parameter Comparison of Plane_B_O
weight ratio *16
impact velocity *60 [kph]
impact angle *20 [°]
position *1997 [mm]
start intrusion (X1) *27.1358 [ms]
time at max intrusion (X3) *105.0883 [ms]
max intrusion (Y3) *623.0944 [mm]
intrusion (Y2) *445.8719 [mm]
gradient (K2) *10.8065 [mm/ms]
Simulation Number
Input-Output Parameter Comparison of Plane_B_L
weight ratio *16
impact velocity *60 [kph]
impact angle *20 [°]
position *1997 [mm]
start intrusion (X1) *26.1817 [ms]
time at max intrusion (X3) *107.575 [ms]
max intrusion (Y3) *624.4726 [mm]
intrusion (Y2) *451.6797 [mm]
gradient (K2) *9.9393 [mm/ms]
Simulation Number

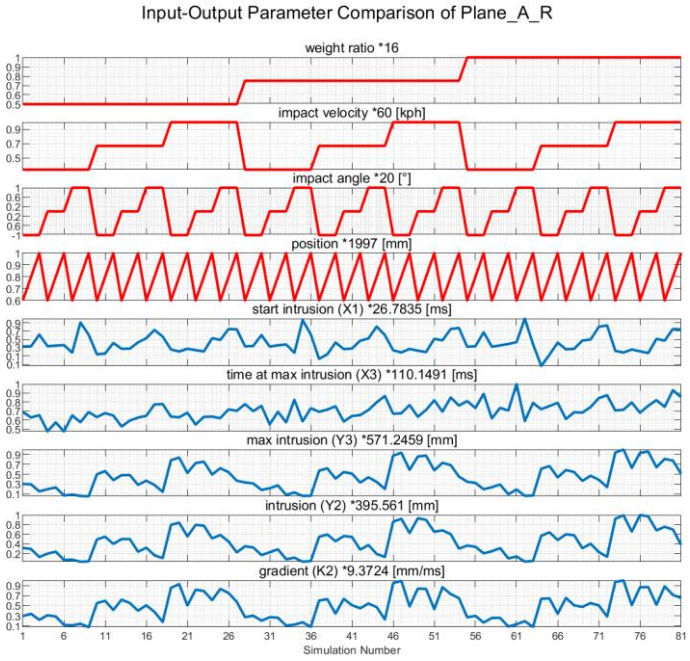
Input-Output Parameter Comparison of Plane_A_R
weight ratio *16
impact velocity *60 [kph]
impact angle *20 [°]
position *1997 [mm]
start intrusion (X1) *26.7835 [ms]
time at max intrusion (X3) *110.1491 [ms]
max intrusion (Y3) *571.2459 [mm]
intrusion (Y2) *395.561 [mm]
gradient (K2) *9.3724 [mm/ms]
Simulation Number

A.3 Input-Output Parameters Comparison HRM

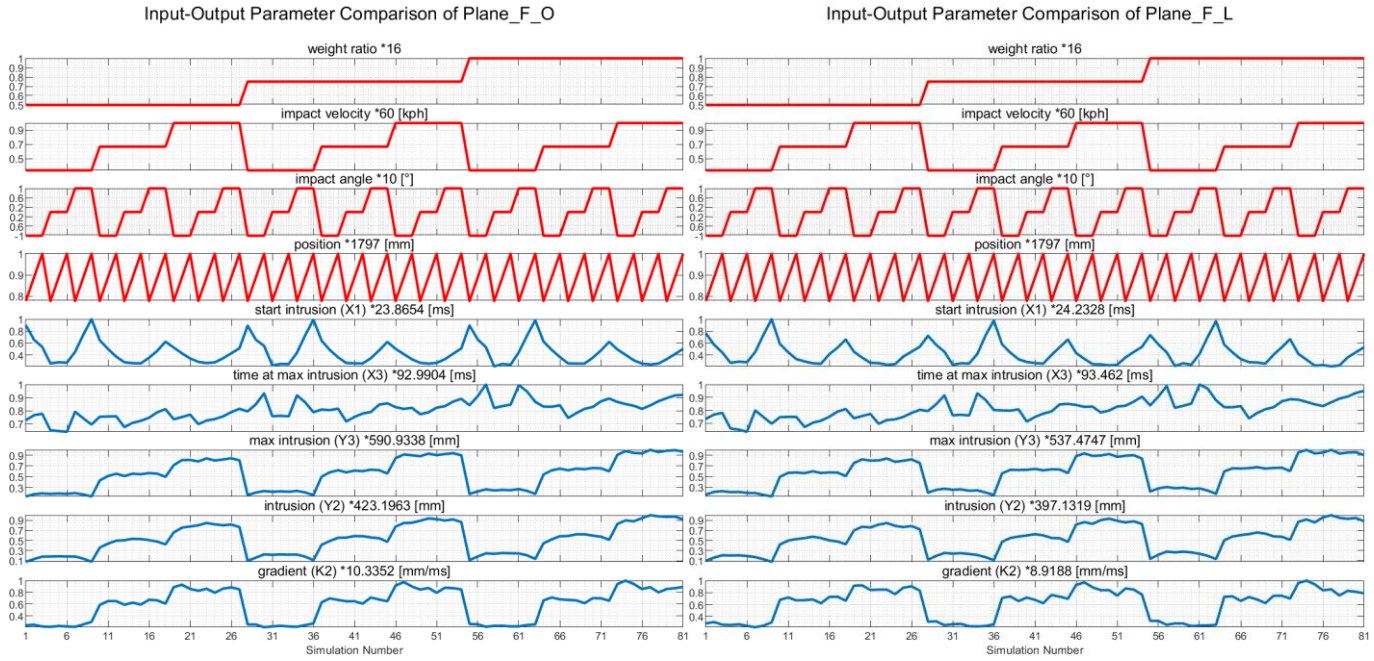

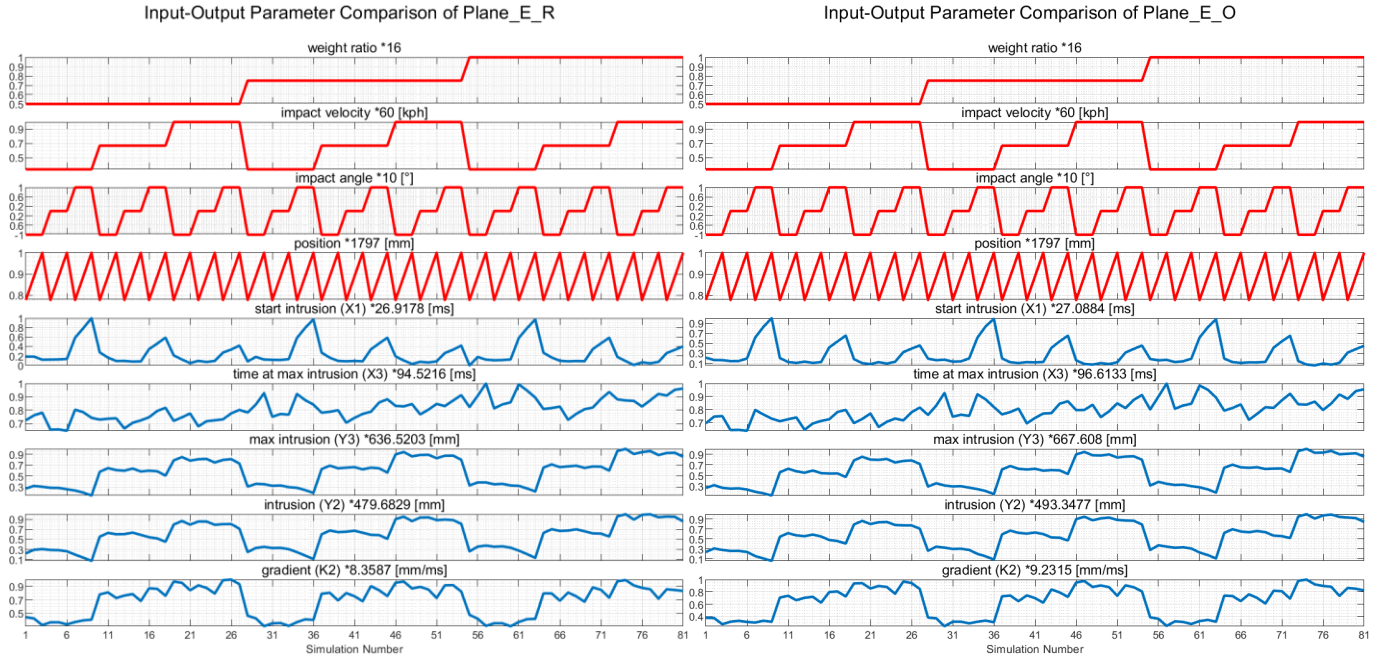

Appendix

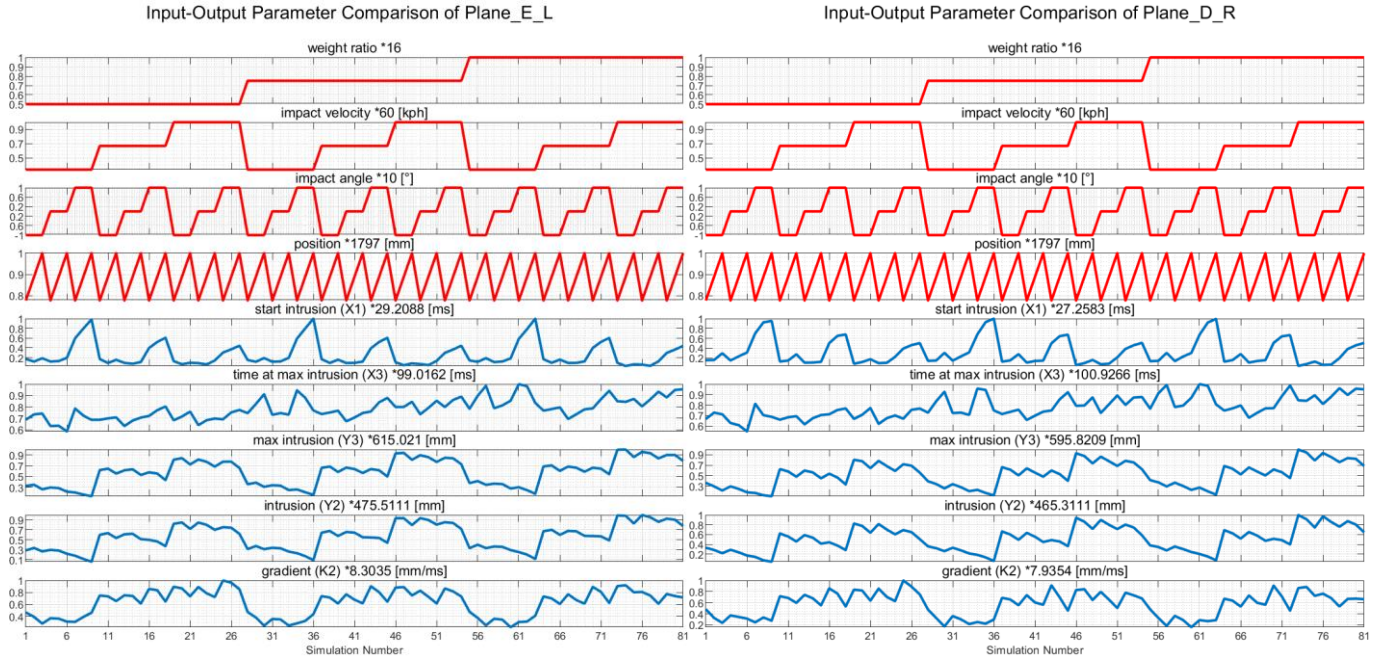
Input-Output Parameter Comparison of Plane_E_L
weight ratio *16
impact velocity *60 [kph]
impact angle *10 [°]
position *1797 [mm]
start intrusion (X1) *29.2088 [ms]
time at max intrusion (X3) *99.0162 [ms]
max intrusion (Y3) *615.021 [mm]
intrusion (Y2) *475.5111 [mm]
gradient (K2) *8.3035 [mm/ms]
Simulation Number

Input-Output Parameter Comparison of Plane_D_R
weight ratio *16
impact velocity *60 [kph]
impact angle *10 [°]
position *1797 [mm]
start intrusion (X1) *27.2583 [ms]
time at max intrusion (X3) *100.9266 [ms]
max intrusion (Y3) *595.8209 [mm]
intrusion (Y2) *465.3111 [mm]
gradient (K2) *7.9354 [mm/ms]
Simulation Number

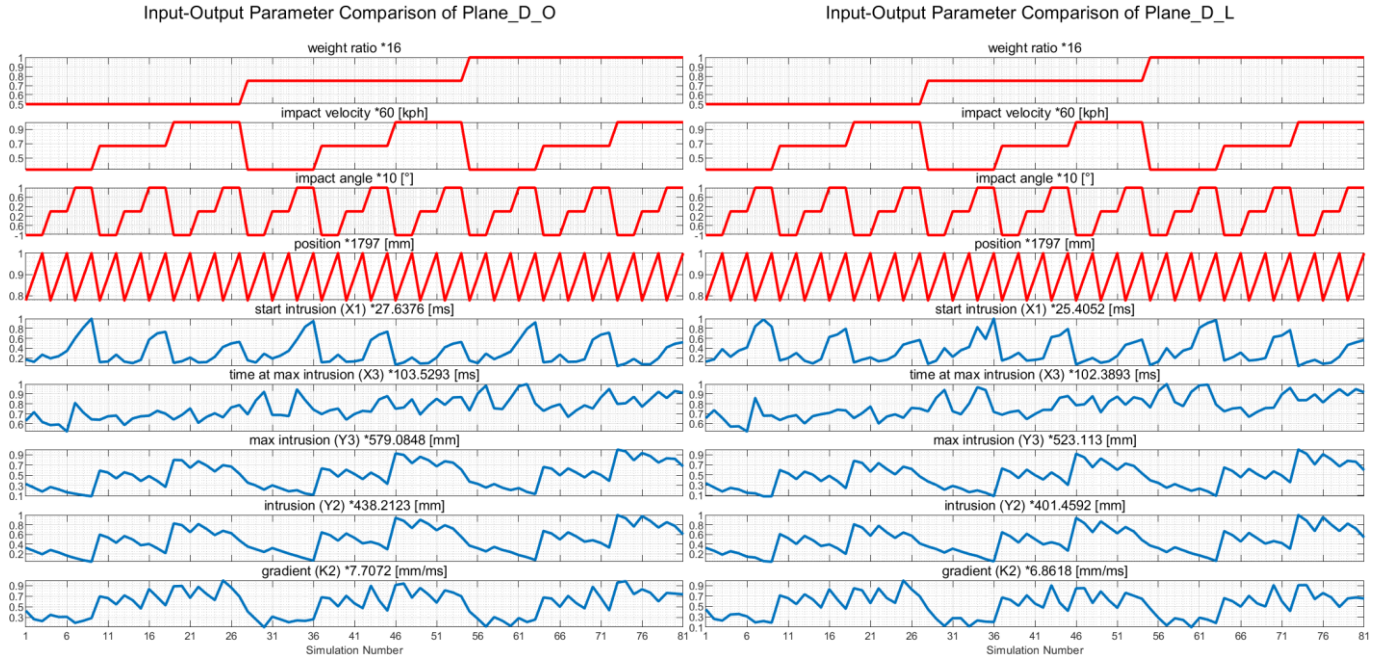
Input-Output Parameter Comparison of Plane_D_O
weight ratio *16
impact velocity *60 [kph]
impact angle *10 [°]
position *1797 [mm]
start intrusion (X1) *27.6376 [ms]
time at max intrusion (X3) *103.5293 [ms]
max intrusion (Y3) *579.0848 [mm]
intrusion (Y2) *438.2123 [mm]
gradient (K2) *7.7072 [mm/ms]
Simulation Number

Input-Output Parameter Comparison of Plane_D_L
weight ratio *16
impact velocity *60 [kph]
impact angle *10 [°]
position *1797 [mm]
start intrusion (X1) *25.4052 [ms]
time at max intrusion (X3) *102.3893 [ms]
max intrusion (Y3) *523.113 [mm]
intrusion (Y2) *401.4592 [mm]
gradient (K2) *6.8618 [mm/ms]
Simulation Number

Appendix

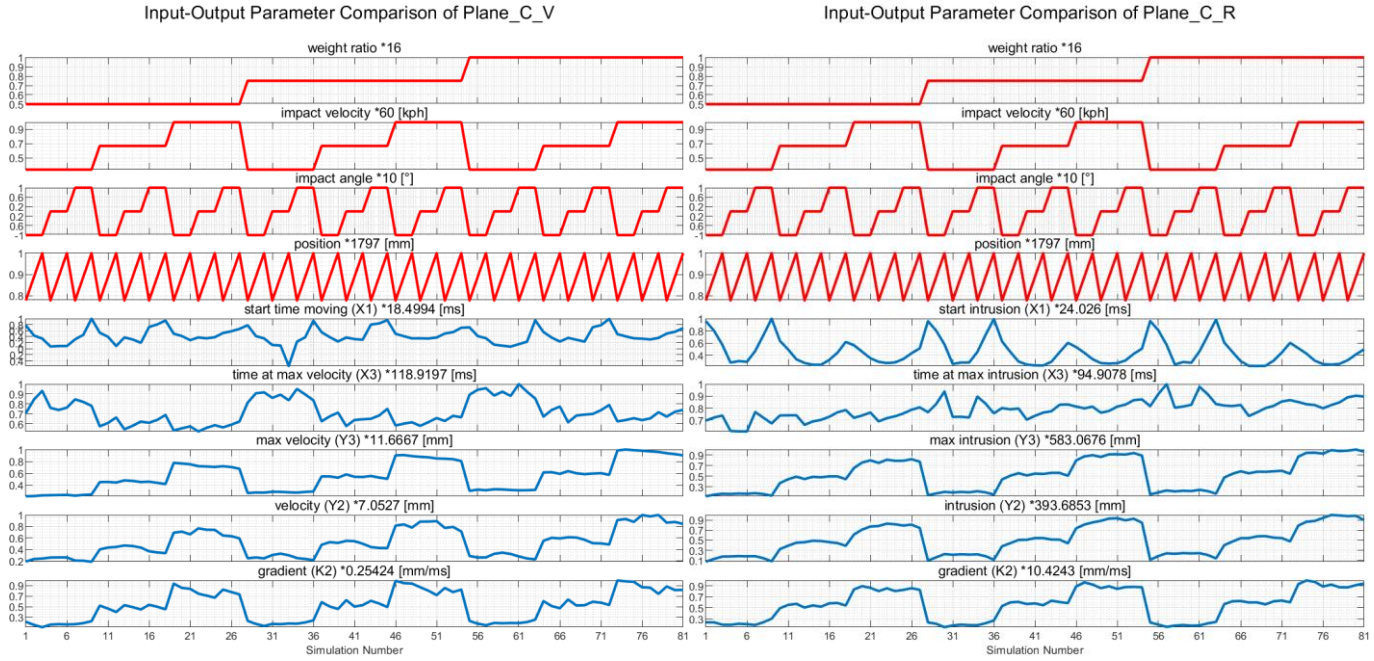
Input-Output Parameter Comparison of Plane_C_V
weight ratio *16
impact velocity *60 [kph]
impact angle *10 [°]
position *1797 [mm]
start time moving (X1) *18.4994 [ms]
time at max velocity (X3) *118.9197 [ms]
max velocity (Y3) *11.6667 [mm]
velocity (Y2) *7.0527 [mm]
gradient (K2) *0.25424 [mm/ms]
Simulation Number
Input-Output Parameter Comparison of Plane_C_R
weight ratio *16
impact velocity *60 [kph]
impact angle *10 [°]
position *1797 [mm]
start intrusion (X1) *24.026 [ms]
time at max intrusion (X3) *94.9078 [ms]
max intrusion (Y3) *583.0676 [mm]
intrusion (Y2) *393.6853 [mm]
gradient (K2) *10.4243 [mm/ms]
Simulation Number

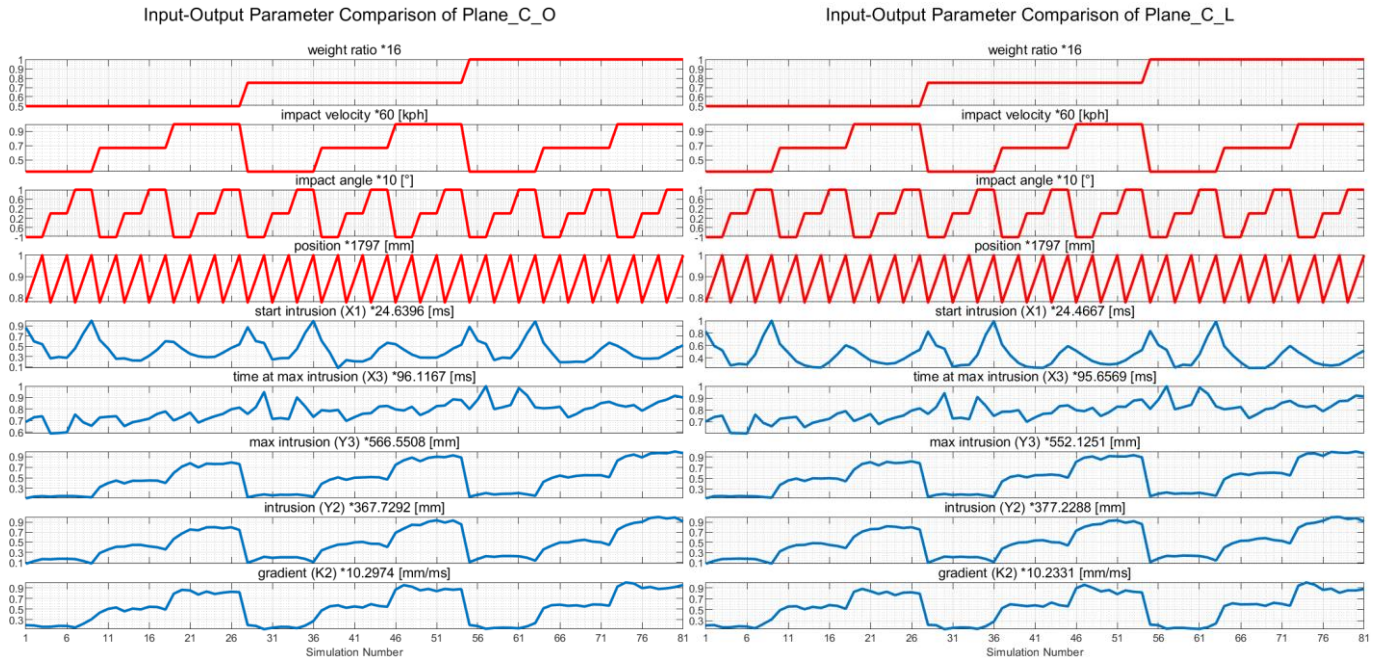
Input-Output Parameter Comparison of Plane_C_O
weight ratio *16
impact velocity *60 [kph]
impact angle *10 [°]
position *1797 [mm]
start intrusion (X1) *24.6396 [ms]
time at max intrusion (X3) *96.1167 [ms]
max intrusion (Y3) *566.5508 [mm]
intrusion (Y2) *367.7292 [mm]
gradient (K2) *10.2974 [mm/ms]
Simulation Number
Input-Output Parameter Comparison of Plane_C_L
weight ratio *16
impact velocity *60 [kph]
impact angle *10 [°]
position *1797 [mm]
start intrusion (X1) *24.4667 [ms]
time at max intrusion (X3) *95.6569 [ms]
max intrusion (Y3) *552.1251 [mm]
intrusion (Y2) *377.2288 [mm]
gradient (K2) *10.2331 [mm/ms]
Simulation Number

Appendix

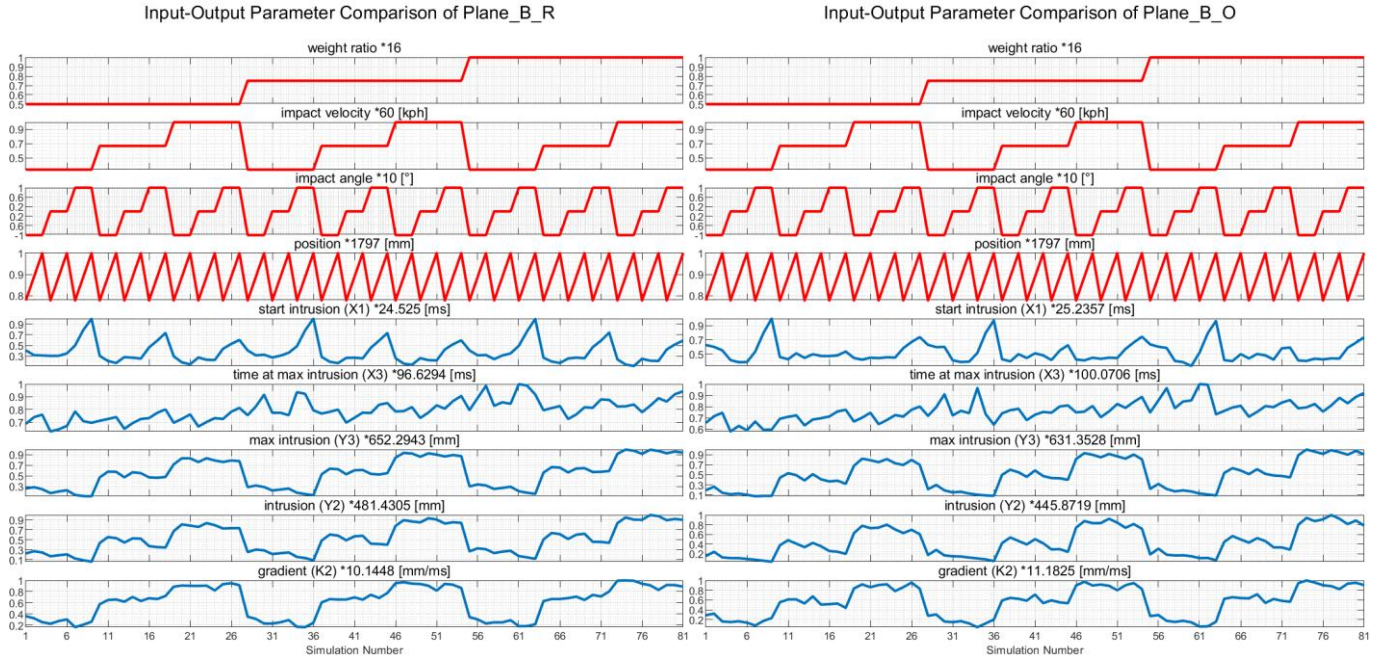
Input-Output Parameter Comparison of Plane_B_R
weight ratio *16
impact velocity *60 [kph]
impact angle *10 [°]
position *1797 [mm]
start intrusion (X1) *24.525 [ms]
time at max intrusion (X3) *96.6294 [ms]
max intrusion (Y3) *652.2943 [mm]
intrusion (Y2) *481.4305 [mm]
gradient (K2) *10.1448 [mm/ms]
Simulation Number
Input-Output Parameter Comparison of Plane_B_O
weight ratio *16
impact velocity *60 [kph]
impact angle *10 [°]
position *1797 [mm]
start intrusion (X1) *25.2357 [ms]
time at max intrusion (X3) *100.0706 [ms]
max intrusion (Y3) *631.3528 [mm]
intrusion (Y2) *445.8719 [mm]
gradient (K2) *11.1825 [mm/ms]
Simulation Number

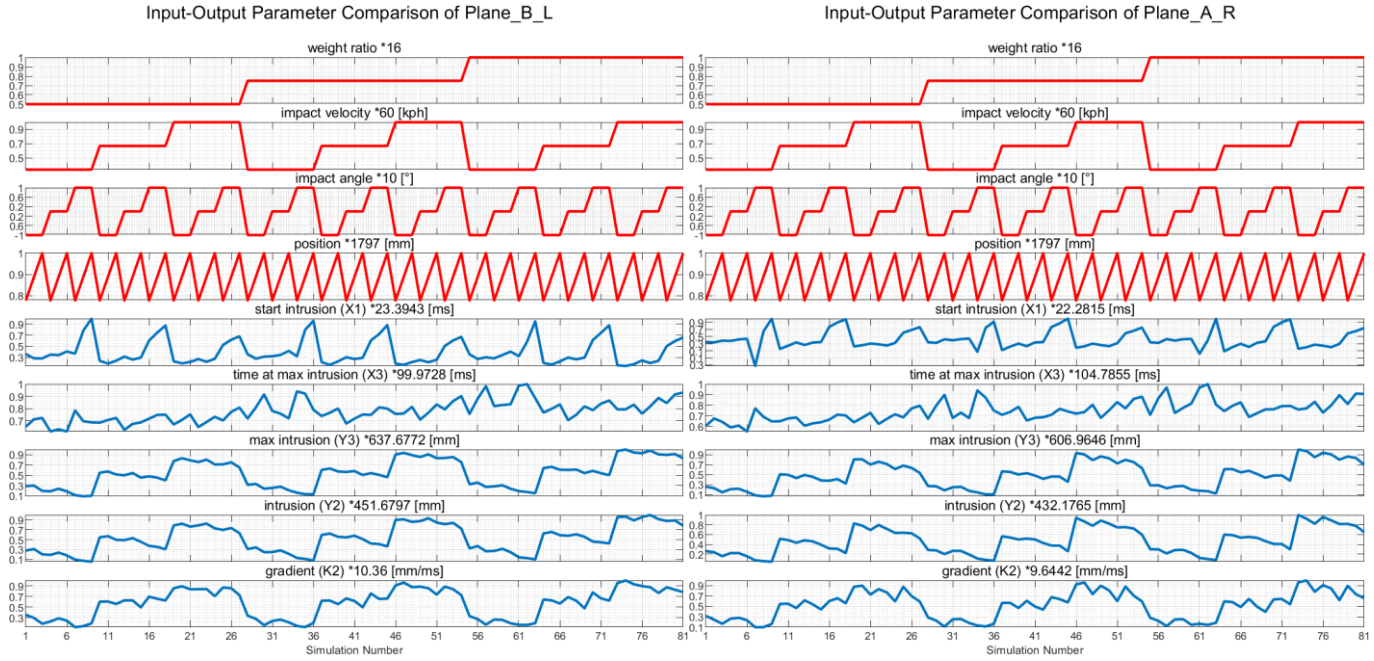
Input-Output Parameter Comparison of Plane_B_L
weight ratio *16
impact velocity *60 [kph]
impact angle *10 [°]
position *1797 [mm]
start intrusion (X1) *23.3943 [ms]
time at max intrusion (X3) *99.9728 [ms]
max intrusion (Y3) *637.6772 [mm]
intrusion (Y2) *451.6797 [mm]
gradient (K2) *10.36 [mm/ms]
Simulation Number
Input-Output Parameter Comparison of Plane_A_R
weight ratio *16
impact velocity *60 [kph]
impact angle *10 [°]
position *1797 [mm]
start intrusion (X1) *22.2815 [ms]
time at max intrusion (X3) *104.7855 [ms]
max intrusion (Y3) *606.9646 [mm]
intrusion (Y2) *432.1765 [mm]
gradient (K2) *9.6442 [mm/ms]
Simulation Number

Appendix

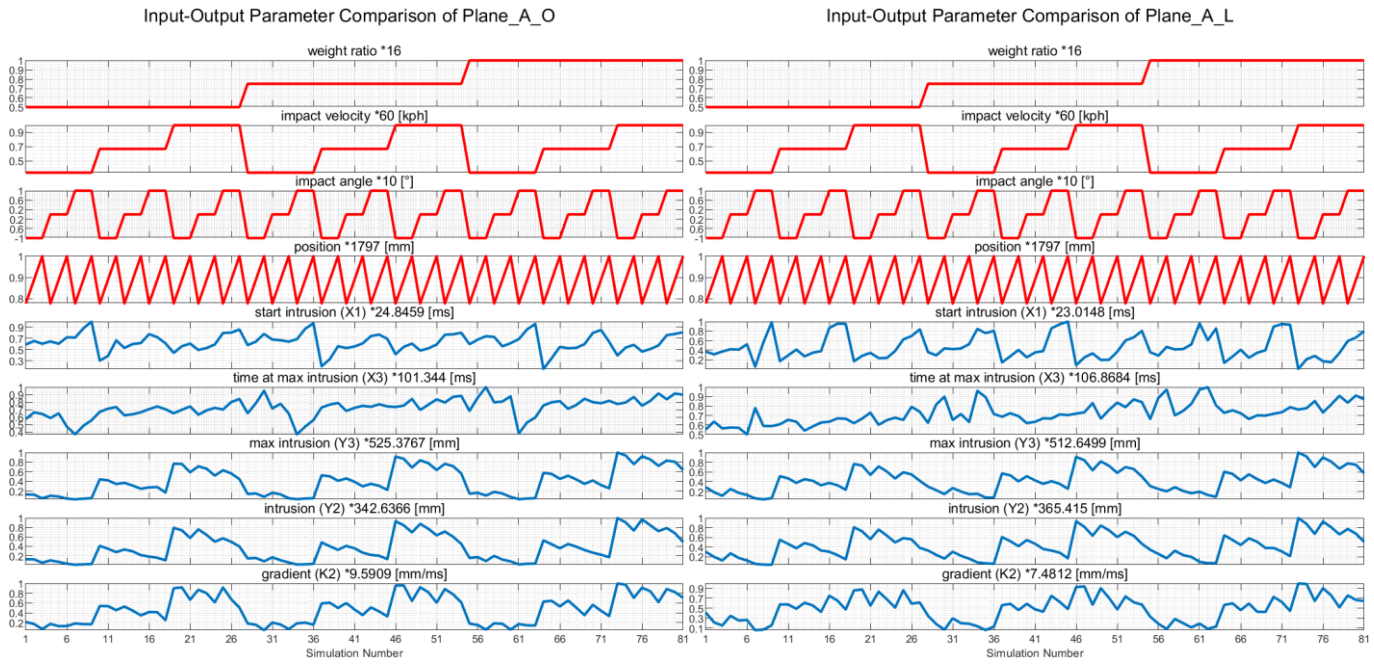
Input-Output Parameter Comparison of Plane_A_O
weight ratio *16
impact velocity *60 [kph]
impact angle *10 [°]
position *1797 [mm]
start intrusion (X1) *24.8459 [ms]
time at max intrusion (X3) *101.344 [ms]
max intrusion (Y3) *525.3767 [mm]
intrusion (Y2) *342.6366 [mm]
gradient (K2) *9.5909 [mm/ms]
Simulation Number
Input-Output Parameter Comparison of Plane_A_L
weight ratio *16
impact velocity *60 [kph]
impact angle *10 [°]
position *1797 [mm]
start intrusion (X1) *23.0148 [ms]
time at max intrusion (X3) *106.8684 [ms]
max intrusion (Y3) *512.6499 [mm]
intrusion (Y2) *365.415 [mm]
gradient (K2) *7.4812 [mm/ms]
Simulation Number

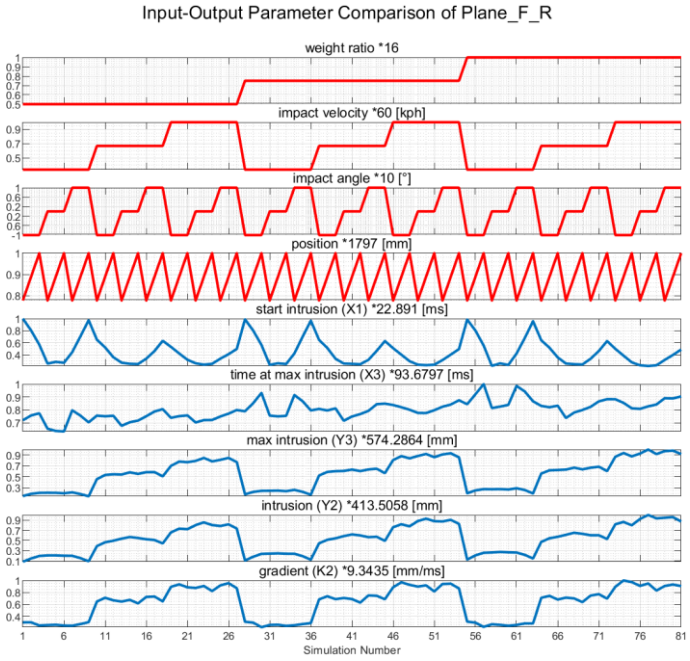
Input-Output Parameter Comparison of Plane_F_R
weight ratio *16
impact velocity *60 [kph]
impact angle *10 [°]
position *1797 [mm]
start intrusion (X1) *22.891 [ms]
time at max intrusion (X3) *93.6797 [ms]
max intrusion (Y3) *574.2864 [mm]
intrusion (Y2) *413.5058 [mm]
gradient (K2) *9.3435 [mm/ms]
Simulation Number

A.4 Input-Output Parameters Comparison FM

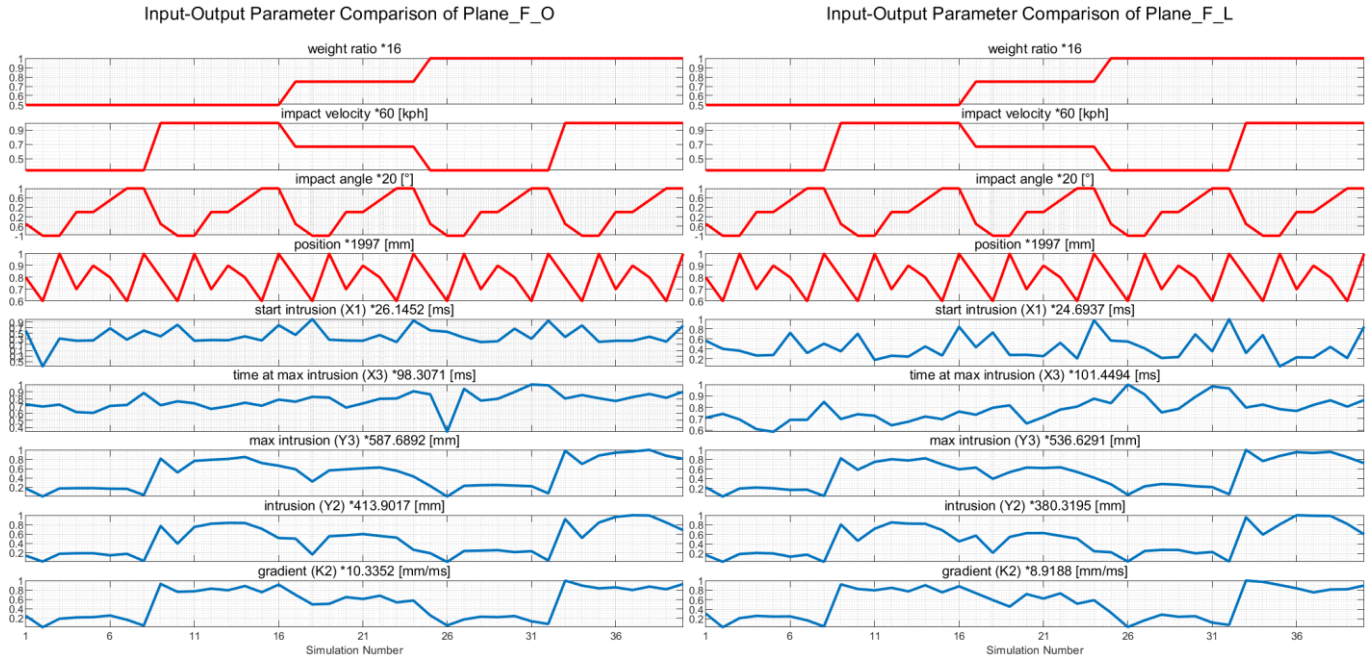

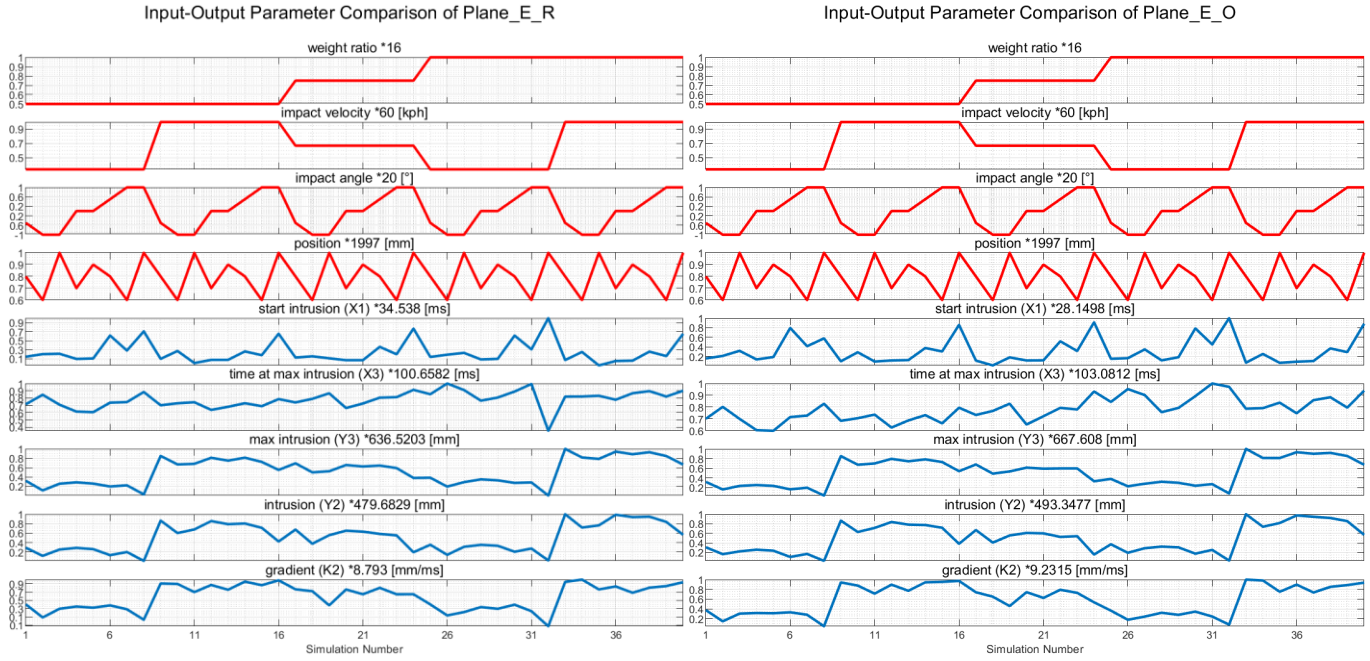

Appendix

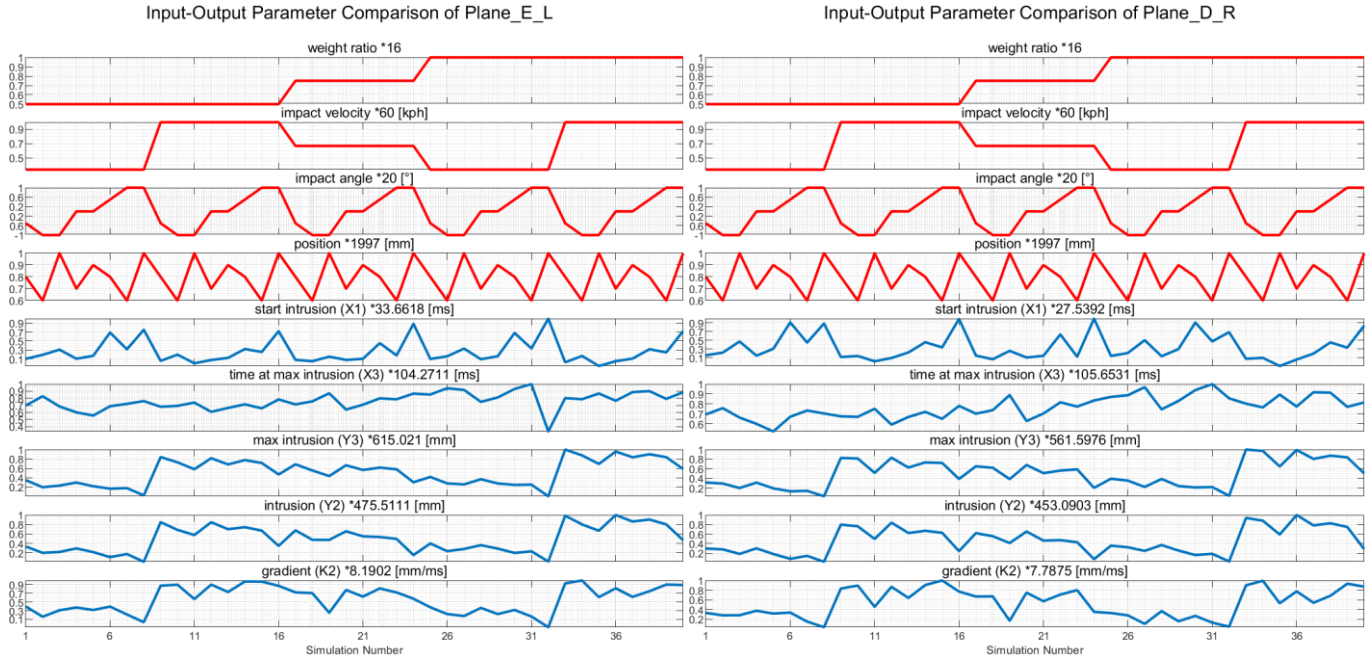
Input-Output Parameter Comparison of Plane_E_L
weight ratio *16
impact velocity *60 [kph]
impact angle *20 [°]
position *1997 [mm]
start intrusion (X1) *33.6618 [ms]
time at max intrusion (X3) *104.2711 [ms]
max intrusion (Y3) *615.021 [mm]
intrusion (Y2) *475.5111 [mm]
gradient (K2) *8.1902 [mm/ms]
Simulation Number
Input-Output Parameter Comparison of Plane_D_R
weight ratio *16
impact velocity *60 [kph]
impact angle *20 [°]
position *1997 [mm]
start intrusion (X1) *27.5392 [ms]
time at max intrusion (X3) *105.6531 [ms]
max intrusion (Y3) *561.5976 [mm]
intrusion (Y2) *453.0903 [mm]
gradient (K2) *7.7875 [mm/ms]
Simulation Number

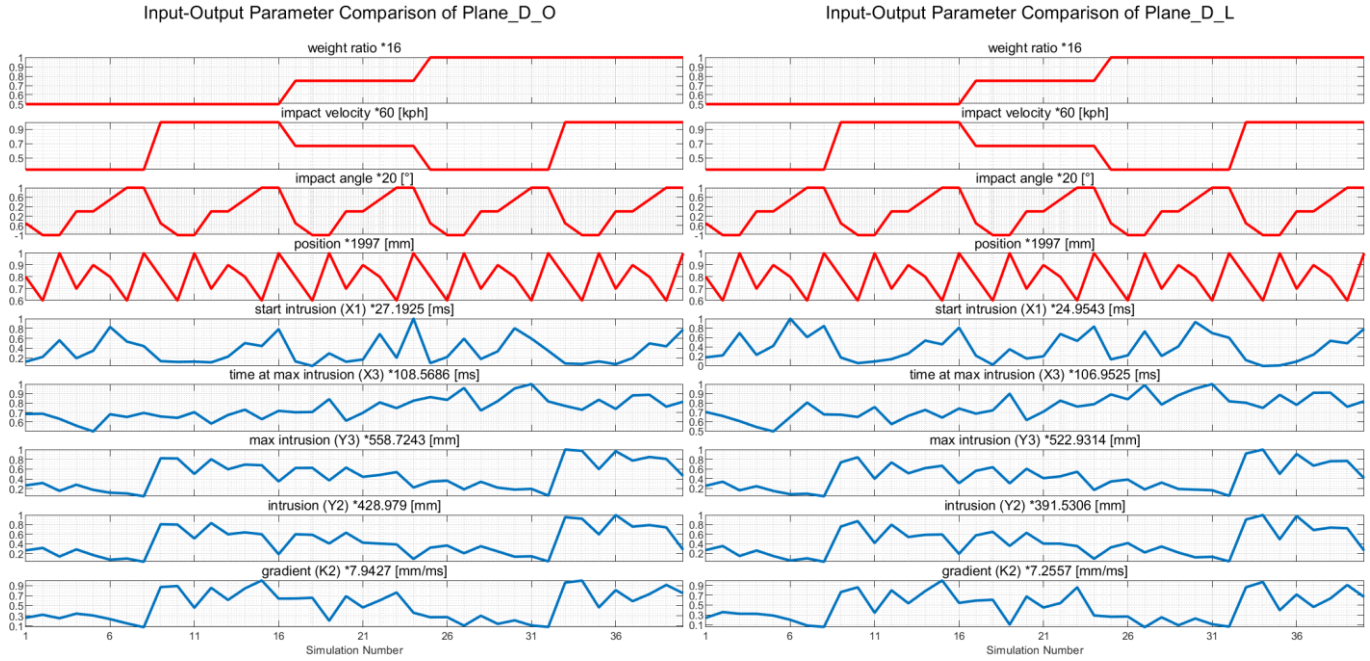
Input-Output Parameter Comparison of Plane_D_O
weight ratio *16
impact velocity *60 [kph]
impact angle *20 [°]
position *1997 [mm]
start intrusion (X1) *27.1925 [ms]
time at max intrusion (X3) *108.5686 [ms]
max intrusion (Y3) *558.7243 [mm]
intrusion (Y2) *428.979 [mm]
gradient (K2) *7.9427 [mm/ms]
Simulation Number
Input-Output Parameter Comparison of Plane_D_L
weight ratio *16
impact velocity *60 [kph]
impact angle *20 [°]
position *1997 [mm]
start intrusion (X1) *24.9543 [ms]
time at max intrusion (X3) *106.9525 [ms]
max intrusion (Y3) *522.9314 [mm]
intrusion (Y2) *391.5306 [mm]
gradient (K2) *7.2557 [mm/ms]
Simulation Number

Appendix

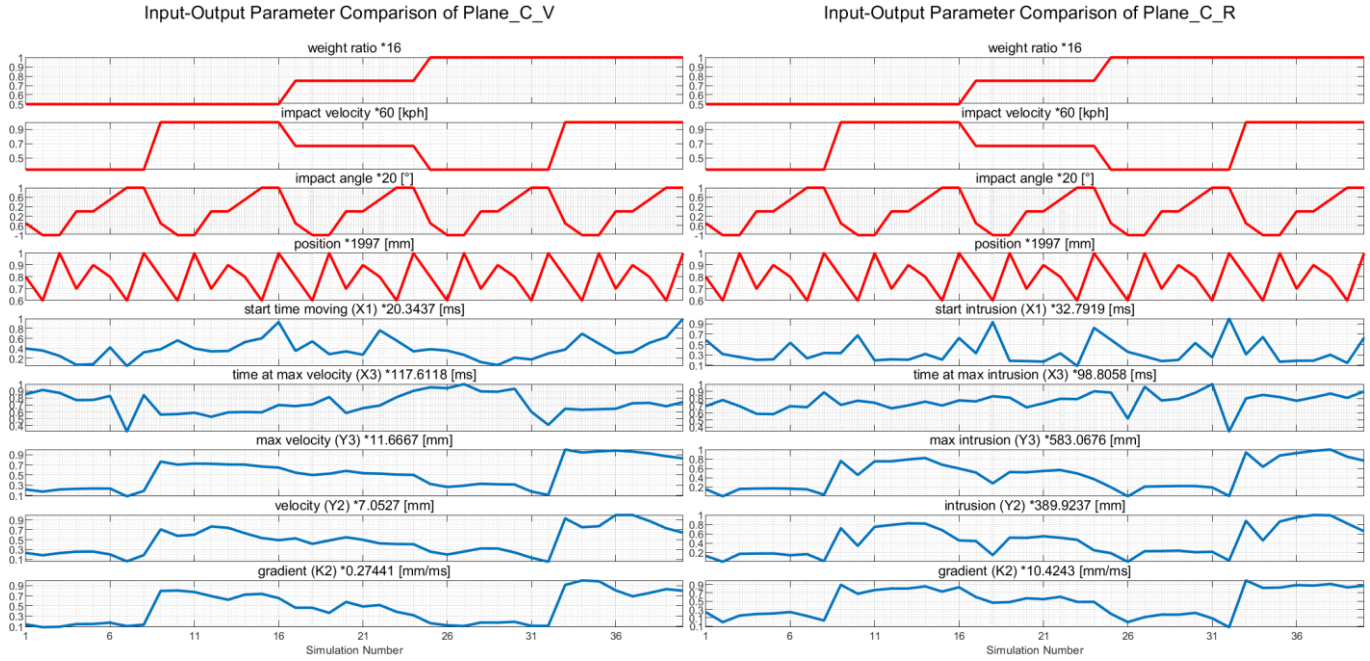
Input-Output Parameter Comparison of Plane_C_V
weight ratio *16
impact velocity *60 [kph]
impact angle *20 [°]
position *1997 [mm]
start time moving (X1) *20.3437 [ms]
time at max velocity (X3) *117.6118 [ms]
max velocity (Y3) *11.6667 [mm]
velocity (Y2) *7.0527 [mm]
gradient (K2) *0.27441 [mm/ms]
Simulation Number
Input-Output Parameter Comparison of Plane_C_R
weight ratio *16
impact velocity *60 [kph]
impact angle *20 [°]
position *1997 [mm]
start intrusion (X1) *32.7919 [ms]
time at max intrusion (X3) *98.8058 [ms]
max intrusion (Y3) *583.0676 [mm]
intrusion (Y2) *389.9237 [mm]
gradient (K2) *10.4243 [mm/ms]
Simulation Number

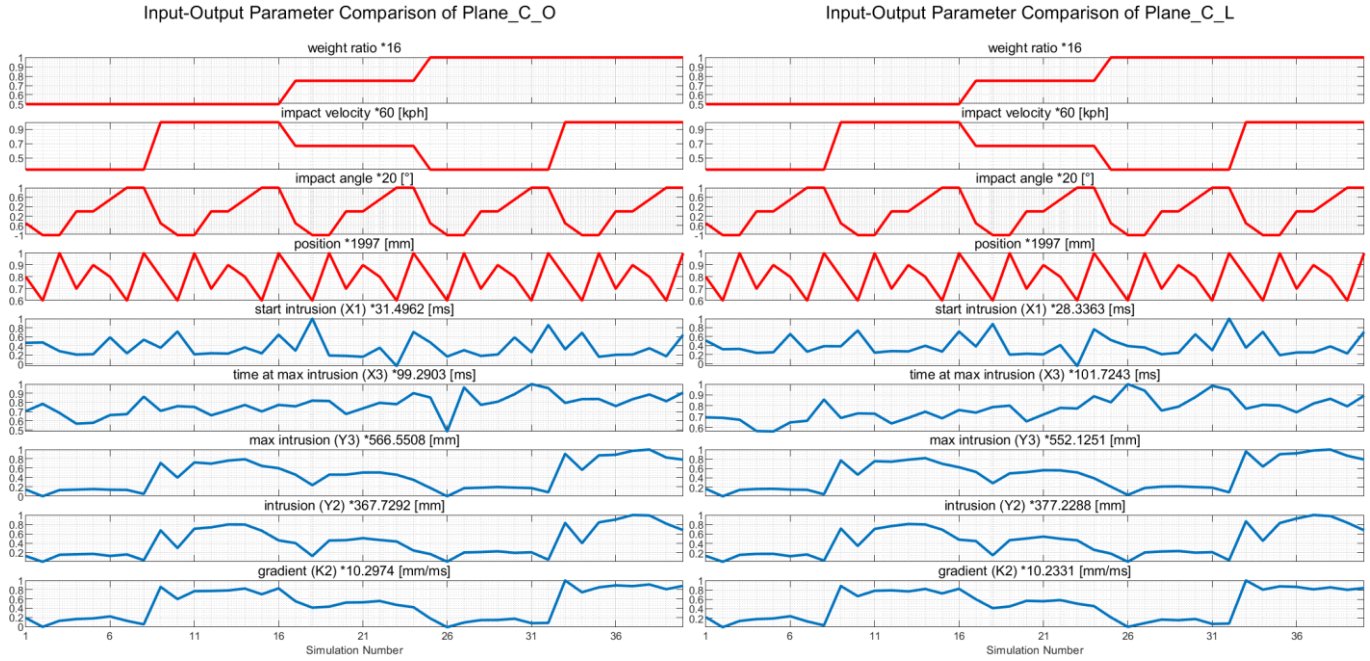
Input-Output Parameter Comparison of Plane_C_O
weight ratio *16
impact velocity *60 [kph]
impact angle *20 [°]
position *1997 [mm]
start intrusion (X1) *31.4962 [ms]
time at max intrusion (X3) *99.2903 [ms]
max intrusion (Y3) *566.5508 [mm]
intrusion (Y2) *367.7292 [mm]
gradient (K2) *10.2974 [mm/ms]
Simulation Number
Input-Output Parameter Comparison of Plane_C_L
weight ratio *16
impact velocity *60 [kph]
impact angle *20 [°]
position *1997 [mm]
start intrusion (X1) *28.3363 [ms]
time at max intrusion (X3) *101.7243 [ms]
max intrusion (Y3) *552.1251 [mm]
intrusion (Y2) *377.2288 [mm]
gradient (K2) *10.2331 [mm/ms]
Simulation Number

Appendix

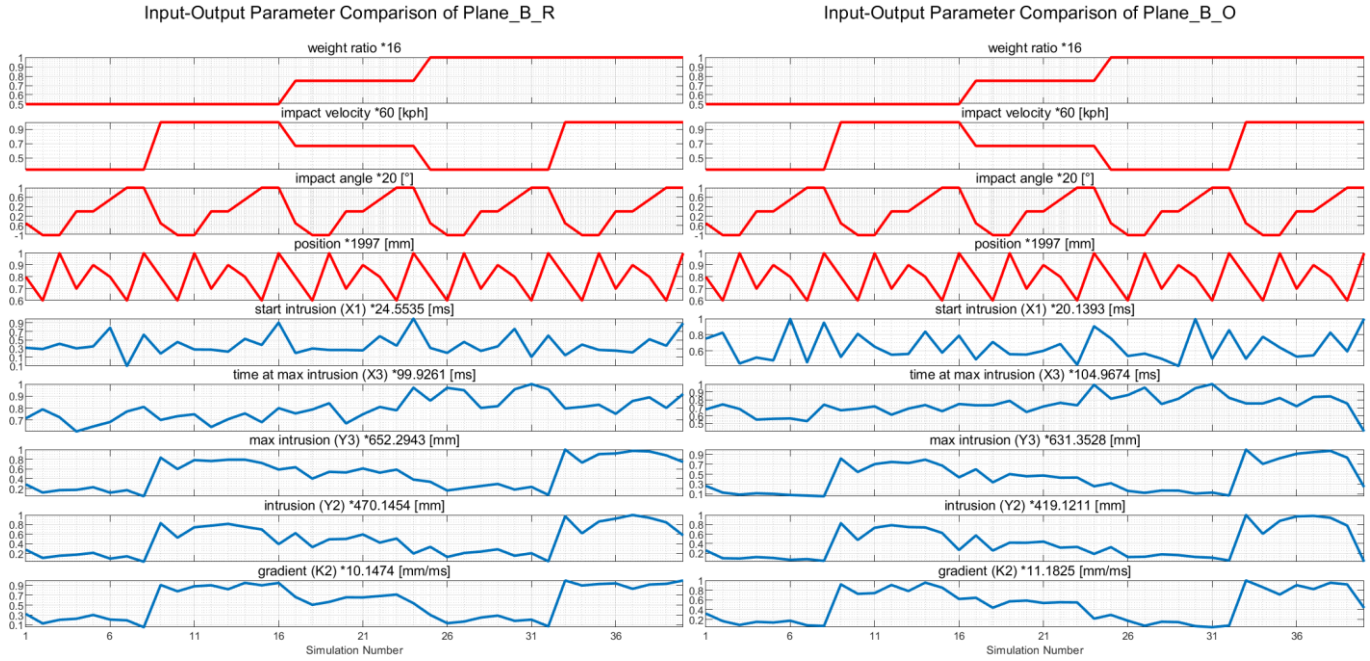
Input-Output Parameter Comparison of Plane_B_R
weight ratio *16
impact velocity *60 [kph]
impact angle *20 [°]
position *1997 [mm]
start intrusion (X1) *24.5535 [ms]
time at max intrusion (X3) *99.9261 [ms]
max intrusion (Y3) *652.2943 [mm]
intrusion (Y2) *470.1454 [mm]
gradient (K2) *10.1474 [mm/ms]
Simulation Number

Input-Output Parameter Comparison of Plane_B_O
weight ratio *16
impact velocity *60 [kph]
impact angle *20 [°]
position *1997 [mm]
start intrusion (X1) *20.1393 [ms]
time at max intrusion (X3) *104.9674 [ms]
max intrusion (Y3) *631.3528 [mm]
intrusion (Y2) *419.1211 [mm]
gradient (K2) *11.1825 [mm/ms]
Simulation Number

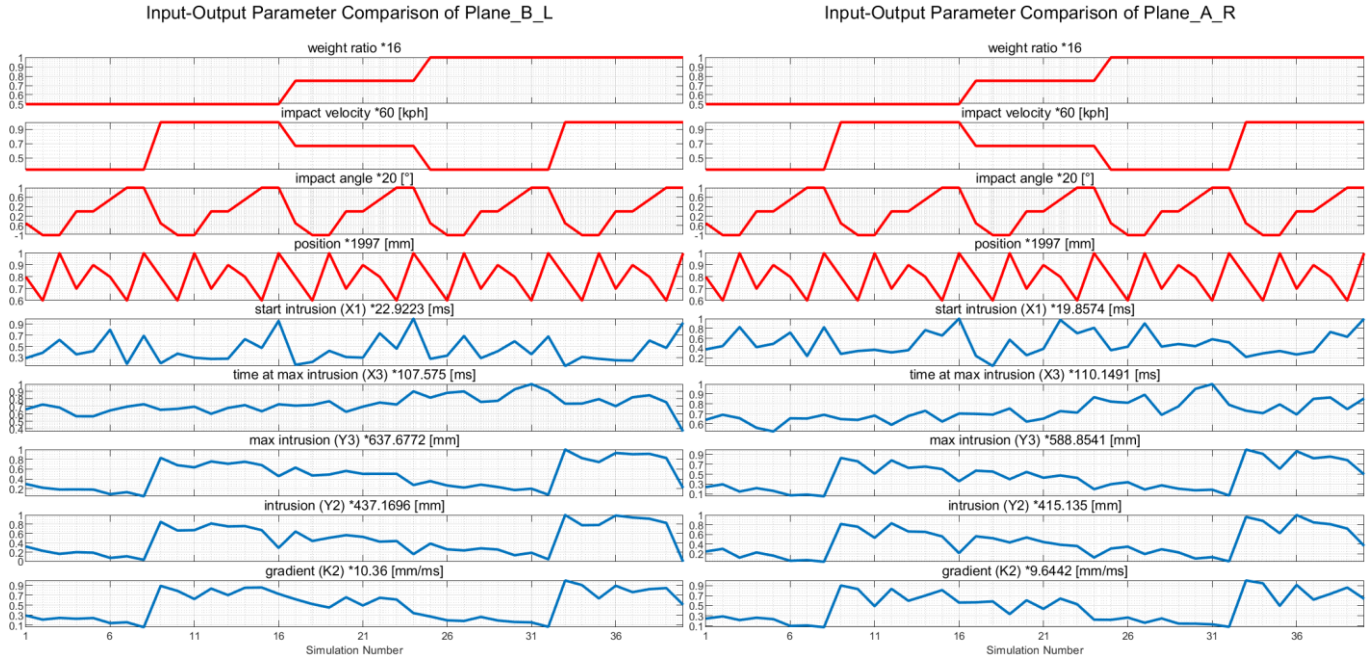
Input-Output Parameter Comparison of Plane_B_L
weight ratio *16
impact velocity *60 [kph]
impact angle *20 [°]
position *1997 [mm]
start intrusion (X1) *22.9223 [ms]
time at max intrusion (X3) *107.575 [ms]
max intrusion (Y3) *637.6772 [mm]
intrusion (Y2) *437.1696 [mm]
gradient (K2) *10.36 [mm/ms]
Simulation Number

Input-Output Parameter Comparison of Plane_A_R
weight ratio *16
impact velocity *60 [kph]
impact angle *20 [°]
position *1997 [mm]
start intrusion (X1) *19.8574 [ms]
time at max intrusion (X3) *110.1491 [ms]
max intrusion (Y3) *588.8541 [mm]
intrusion (Y2) *415.135 [mm]
gradient (K2) *9.6442 [mm/ms]
Simulation Number

Appendix

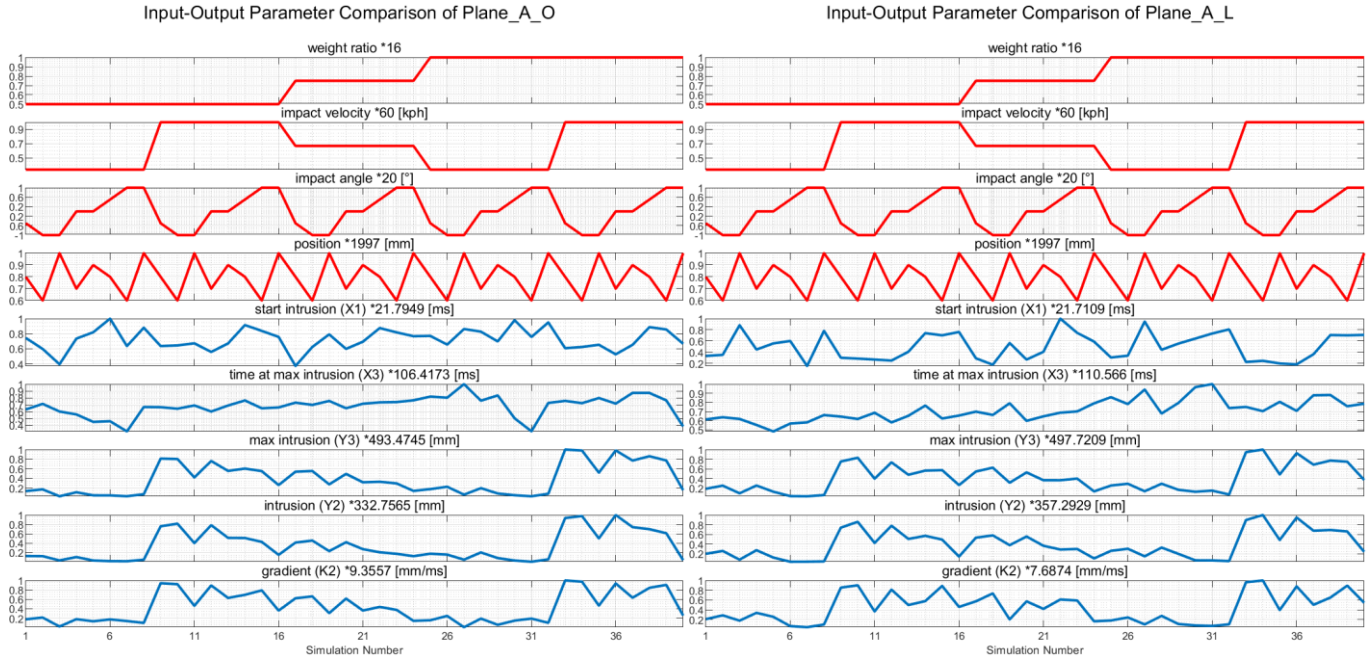
Input-Output Parameter Comparison of Plane_A_O
weight ratio *16
impact velocity *60 [kph]
impact angle *20 [°]
position *1997 [mm]
start intrusion (X1) *21.7949 [ms]
time at max intrusion (X3) *106.4173 [ms]
max intrusion (Y3) *493.4745 [mm]
intrusion (Y2) *332.7565 [mm]
gradient (K2) *9.3557 [mm/ms]
Simulation Number
Input-Output Parameter Comparison of Plane_A_L
weight ratio *16
impact velocity *60 [kph]
impact angle *20 [°]
position *1997 [mm]
start intrusion (X1) *21.7109 [ms]
time at max intrusion (X3) *110.566 [ms]
max intrusion (Y3) *497.7209 [mm]
intrusion (Y2) *357.2929 [mm]
gradient (K2) *7.6874 [mm/ms]
Simulation Number

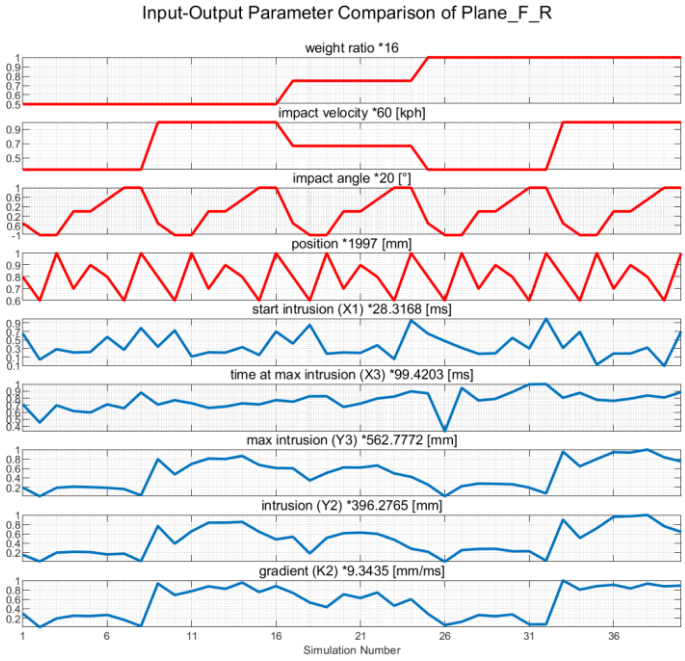
Input-Output Parameter Comparison of Plane_F_R
weight ratio *16
impact velocity *60 [kph]
impact angle *20 [°]
position *1997 [mm]
start intrusion (X1) *28.3168 [ms]
time at max intrusion (X3) *99.4203 [ms]
max intrusion (Y3) *562.7772 [mm]
intrusion (Y2) *396.2765 [mm]
gradient (K2) *9.3435 [mm/ms]
Simulation Number

A.5 Meta-model Selection

HRM

Table Appendix 2 Validation result for output X1 and X2 of the HRM types.

	Start of intrusion; X1					Time at maximum intrusion; X3				
	GPML	**Kriging**	**LSSVM**	**Rational**	**RBF**	**GMPL**	**Kriging**	**LSSVM**	**Rational**	**RBF**
A_L	0.569	0.610	0.533	0.603	0.558	0.838	0.704	0.850	0.861	0.811
A_O	1.018	1.043	1.023	0.979	1.050	1.074	1.436	1.101	1.404	1.200
A_R	0.516	0.813	0.504	1.314	0.499	0.762	0.576	0.774	0.759	0.715
B_L	0.424	0.449	0.435	0.897	0.413	0.779	0.716	0.776	0.895	0.735
B_O	0.890	0.944	0.912	0.887	1.008	1.078	0.865	1.067	1.040	0.997
B_R	0.634	0.667	0.636	0.894	0.620	0.887	0.666	0.888	0.974	0.833
C_V	1.472	1.609	1.497	2.415	1.533	1.088	1.000	1.091	1.335	1.021
C_L	1.960	14.272	1.950	1.948	2.015	1.083	0.887	1.105	1.293	1.057
C_O	1.688	2.952	1.683	1.631	1.772	1.125	1.400	1.130	1.006	1.052
C_R	0.682	0.960	0.667	1.259	0.685	1.066	1.139	1.072	1.100	1.067
D_L	0.588	0.477	0.597	0.728	0.578	0.941	0.709	0.884	0.986	0.814
D_O	0.453	0.414	0.469	0.912	0.404	0.769	0.589	0.758	0.762	0.676
D_R	0.454	0.412	0.448	0.920	0.404	0.960	0.629	0.931	1.021	0.842
E_L	0.555	0.372	0.552	0.926	0.507	0.958	0.763	0.953	1.081	0.878
E_O	0.485	0.610	0.481	1.120	0.455	0.872	0.589	0.877	2.188	0.823
E_R	0.745	0.819	0.743	1.420	0.715	0.979	2.800	1.009	1.079	0.939
F_L	1.252	1.967	1.259	1.353	1.310	1.074	5.200	1.085	1.190	1.011
F_O	1.608	0.372	1.645	2.968	1.782	1.059	1.003	1.078	1.135	1.007
F_R	1.387	1.934	1.411	2.585	1.561	1.141	1.112	1.167	2.195	1.103
Mean	0.915	1.668	0.918	1.356	0.940	0.975	1.199	0.979	1.174	0.925

Appendix

Table Appendix 3 Validation result for output Y2 and Y3 of the HRM types.

	Maximum intrusion; Y3					Intrusion at point 2; Y2				
	GPML	**Kriging**	**LSSVM**	**Rational**	**RBF**	**GPML**	**Kriging**	**LSSVM**	**Rational**	**RBF**
A_L	0.350	0.245	0.304	0.880	0.195	0.207	0.328	0.206	0.711	0.203
A_O	0.136	0.166	0.121	0.132	0.140	0.154	0.208	0.147	0.771	0.151
A_R	0.127	0.393	0.139	0.823	0.104	0.261	1.632	0.254	0.487	0.164
B_L	0.125	0.518	0.143	0.742	0.092	0.186	0.249	0.178	0.277	0.171
B_O	0.154	0.198	0.157	0.227	0.169	0.209	1.356	0.212	0.247	0.218
B_R	0.196	0.159	0.209	0.720	0.162	0.218	0.224	0.231	0.726	0.138
C_V	0.100	5.951	0.086	0.112	0.060	0.138	0.085	0.143	0.779	0.076
C_L	0.079	0.071	0.071	0.140	0.049	0.140	0.109	0.159	0.491	0.088
C_O	0.071	0.068	0.068	0.425	0.048	0.135	0.135	0.133	0.087	0.085
C_R	0.446	0.449	0.444	0.941	0.445	0.530	0.509	0.529	0.581	0.503
D_L	0.422	0.313	0.447	0.643	0.336	0.162	0.178	0.158	0.540	0.143
D_O	0.225	0.771	0.225	0.250	0.139	0.103	0.568	0.107	0.784	0.093
D_R	0.378	0.645	0.415	0.247	0.245	0.137	0.713	0.148	0.216	0.125
E_L	0.379	1.991	0.376	0.702	0.229	0.160	1.805	0.218	0.220	0.207
E_O	0.158	0.165	0.178	0.775	0.141	0.133	0.258	0.137	0.144	0.123
E_R	0.209	0.212	0.250	0.417	0.195	0.123	0.639	0.130	0.113	0.112
F_L	0.187	3.075	0.186	0.742	0.144	0.120	4.290	0.123	0.107	0.083
F_O	0.093	0.275	0.098	0.623	0.076	0.076	0.642	0.078	0.297	0.062
F_R	0.113	0.929	0.117	0.741	0.099	0.086	0.252	0.095	0.140	0.063
Mean	0.208	0.873	0.212	0.541	0.161	0.173	0.746	0.178	0.406	0.148

Table Appendix 4 Validation result for output K2 of the HRM types.

	Gradient at point 2; K2				
	GPML	**Kriging**	**LSSVM**	**Rational**	**RBF**
A_L	0.757	0.833	0.807	0.749	0.804
A_O	0.239	0.280	0.241	0.933	0.195
A_R	0.395	0.442	0.395	0.387	0.375
B_L	0.222	0.389	0.224	0.276	0.228
B_O	0.172	0.179	0.176	0.472	0.172
B_R	0.217	0.232	0.222	0.236	0.213
C_V	0.174	0.163	0.169	0.787	0.163
C_L	0.144	0.174	0.145	1.180	0.146
C_O	0.110	0.100	0.108	0.780	0.110
C_R	0.287	0.284	0.284	0.346	0.301
D_L	0.500	0.488	0.495	0.651	0.473
D_O	0.261	0.391	0.284	0.230	0.236
D_R	0.417	0.463	0.439	0.421	0.417
E_L	0.398	0.625	0.442	0.517	0.373
E_O	0.231	0.385	0.226	1.156	0.218
E_R	0.345	0.420	0.337	1.057	0.360
F_L	0.272	0.420	0.270	0.243	0.234
F_O	0.124	0.122	0.140	0.633	0.115
F_R	0.178	0.322	0.188	0.772	0.198
Mean	0.287	0.353	0.294	0.622	0.281

FRM

Table Appendix 5 Validation result for output X1 and X2 of the FRM types.

	Start of intrusion; X1					Time at maximum intrusion; X3				
	GPML	Kriging	LSSVM	Rational	RBF	GMPL	Kriging	LSSVM	Rational	RBF
A_L	0.757	0.833	0.751	0.864	0.703	1.064	0.829	1.019	1.329	1.034
A_O	1.148	1.059	1.121	1.020	1.167	1.085	0.895	1.084	0.659	1.039
A_R	0.713	1.478	0.607	0.819	0.646	0.963	0.811	0.936	0.905	1.066
B_L	0.623	0.795	0.651	1.037	0.688	1.169	1.120	1.078	1.362	1.101
B_O	1.040	1.084	1.169	14.103	1.099	1.044	31.062	0.990	1.696	1.108
B_R	0.676	0.926	0.699	1.066	0.734	1.299	1.244	1.300	1.458	1.165
C_V	0.991	2.586	0.949	1.356	0.880	1.240	1.067	1.076	1.071	1.189
C_L	2.155	2.954	2.148	2.605	1.794	1.697	1.084	1.685	1.615	1.636
C_O	2.486	1.049	2.385	2.929	1.964	1.304	1.279	1.365	1.682	1.336
C_R	1.994	1.978	2.247	2.188	1.900	1.524	1.028	1.527	1.434	1.202
D_L	0.738	0.813	0.753	1.159	0.761	1.350	0.739	1.297	1.452	1.335
D_O	0.700	0.984	0.679	1.189	0.629	1.252	0.689	1.194	1.076	1.219
D_R	0.755	0.704	0.730	1.259	0.682	1.314	0.748	1.253	1.402	1.212
E_L	0.690	0.882	0.684	1.604	0.798	1.184	0.968	0.990	1.211	1.087
E_O	0.867	1.302	0.795	1.459	0.687	1.333	1.020	1.336	1.059	1.323
E_R	1.290	1.461	1.024	1.591	1.089	1.219	0.909	1.038	1.248	1.260
F_L	1.675	0.561	1.284	2.195	1.701	1.327	1.243	1.612	1.287	1.607
F_O	1.971	2.534	2.327	1.526	2.109	1.505	27.968	1.441	1.191	1.244
F_R	2.378	0.772	2.256	2.751	1.980	1.601	0.837	1.587	1.590	1.380
Mean	1.245	1.303	1.224	2.248	1.159	1.288	3.976	1.253	1.301	1.239

Appendix

Table Appendix 6 Validation result for output Y3 and Y2 of the FRM types.

	Maximum intrusion; Y3					Intrusion at point 2; Y2				
	GPML	Kriging	LSSVM	Rational	RBF	GPML	Kriging	LSSVM	Rational	RBF
A_L	0.287	0.647	0.312	0.374	0.266	0.227	0.202	0.231	0.964	0.229
A_O	0.078	1.061	0.076	0.749	0.073	0.164	0.578	0.155	0.248	0.165
A_R	0.210	0.590	0.231	0.110	0.140	0.419	0.873	0.397	0.111	0.213
B_L	0.170	2.297	0.168	0.148	0.166	0.234	1.951	0.247	0.401	0.231
B_O	0.214	1.814	0.203	0.155	0.216	0.301	0.707	0.263	0.217	0.310
B_R	0.339	1.080	0.267	0.715	0.273	0.364	0.261	0.374	0.309	0.306
C_V	0.450	4.631	0.465	0.503	0.461	0.582	0.604	0.575	0.632	0.586
C_L	0.089	0.078	0.085	0.200	0.123	0.160	0.132	0.163	0.558	0.159
C_O	0.076	0.695	0.094	0.080	0.108	0.218	0.775	0.203	0.826	0.178
C_R	0.072	0.106	0.072	0.121	0.102	0.227	0.077	0.172	0.929	0.154
D_L	0.252	0.422	0.253	0.441	0.299	0.332	0.856	0.152	0.787	0.234
D_O	0.296	1.548	0.314	0.152	0.200	0.293	0.465	0.159	0.686	0.170
D_R	0.253	2.048	0.267	0.417	0.311	0.387	0.275	0.247	0.856	0.212
E_L	0.364	2.293	0.253	0.242	0.306	0.414	1.982	0.396	0.279	0.226
E_O	0.358	1.711	0.404	0.288	0.253	0.388	0.794	0.379	0.401	0.248
E_R	0.303	0.294	0.409	1.628	0.306	0.421	1.090	0.272	0.897	0.245
F_L	0.276	1.984	0.195	0.718	0.227	0.324	0.245	0.221	1.065	0.166
F_O	0.084	1.580	0.087	0.126	0.137	0.154	1.512	0.163	0.740	0.115
F_R	0.108	1.302	0.244	0.202	0.178	0.158	1.930	0.185	0.178	0.150
Mean	0.225	1.378	0.232	0.388	0.218	0.303	0.806	0.261	0.583	0.226

Table Appendix 7 Validation result for output X1 and X2 of the HFM types.

	Gradient at point 2; K2				
	GPML	Kriging	LSSVM	Rational	RBF
A_L	0.840	0.899	0.832	1.023	0.833
A_O	0.291	0.520	0.288	0.296	0.212
A_R	0.455	0.516	0.459	0.530	0.442
B_L	0.312	0.798	0.315	0.887	0.311
B_O	0.164	0.570	0.157	0.268	0.172
B_R	0.187	0.563	0.174	0.768	0.163
C_V	0.282	0.350	0.259	0.418	0.261
C_L	0.197	0.134	0.196	0.159	0.174
C_O	0.182	0.132	0.175	0.133	0.161
C_R	0.190	0.114	0.182	0.159	0.154
D_L	0.433	0.577	0.441	0.451	0.467
D_O	0.268	0.532	0.296	1.034	0.267
D_R	0.418	0.790	0.419	0.708	0.456
E_L	0.388	1.149	0.356	0.618	0.395
E_O	0.270	0.821	0.271	1.236	0.273
E_R	0.397	1.074	0.323	0.438	0.326
F_L	0.212	0.974	0.227	0.252	0.221
F_O	0.140	0.143	0.143	0.314	0.139
F_R	0.227	0.950	0.241	0.260	0.201
Mean	0.308	0.611	0.303	0.524	0.296

FM

Table Appendix 8 Validation result for output X1 and X2 of the FM types.

	Start of intrusion; X1					Time at maximum intrusion; X3				
	GPML	Kriging	LSSVM	Rational	RBF	GPML	Kriging	LSSVM	Rational	RBF
A_L	0.750	0.886	0.843	106.480	0.736	0.885	0.874	0.888	0.942	0.875
A_O	1.062	1.061	1.096	1.059	1.062	1.250	1.362	1.267	1.105	1.280
A_R	0.767	0.860	0.713	0.725	0.739	0.773	0.699	0.760	0.776	0.688
B_L	0.451	0.359	0.419	0.408	0.531	0.797	0.809	0.831	1.600	0.887
B_O	0.949	1.035	1.093	5.687	1.046	0.897	1.097	0.866	0.796	0.979
B_R	0.751	0.904	0.623	0.731	0.663	0.754	0.732	0.770	0.696	0.821
C_V	0.989	1.486	1.025	2.108	0.911	0.869	0.748	0.777	0.560	0.898
C_L	0.897	1.705	0.756	1.656	0.843	1.023	0.558	1.042	0.758	0.815
C_O	1.389	1.491	0.744	2.117	0.616	0.807	17.858	0.807	1.179	1.000
C_R	0.857	0.982	0.950	0.937	0.744	1.115	1.087	1.116	1.006	1.115
D_L	0.716	0.615	0.526	0.362	0.546	0.797	0.802	0.781	0.652	0.755
D_O	0.342	0.225	0.526	0.217	0.453	0.685	1.023	0.754	0.799	0.647
D_R	0.685	0.298	0.636	0.469	0.378	0.724	1.024	0.741	0.796	0.779
E_L	0.421	0.378	0.538	0.723	0.339	0.941	1.113	0.871	0.868	0.836
E_O	0.313	0.714	0.529	0.378	0.350	0.699	1.074	0.782	0.634	0.721
E_R	0.494	1.691	0.506	2.427	0.458	0.813	0.949	0.835	0.714	1.075
F_L	0.609	0.617	0.606	1.447	0.624	1.054	0.720	0.830	0.775	0.890
F_O	0.992	67.119	0.928	1.753	0.786	0.607	0.716	0.613	0.792	0.809
F_R	0.684	0.886	0.669	7.578	1.712	0.750	0.756	0.679	1.360	1.007
Mean	0.743	4.385	0.722	7.224	0.713	0.855	1.789	0.843	0.885	0.888

Appendix

Table Appendix 9 Validation result for output Y3 and Y2 of the FM types.

	Maximum intrusion; Y3					Intrusion at point 2; Y2				
	GPML	Kriging	LSSVM	Rational	RBF	GPML	Kriging	LSSVM	Rational	RBF
A_L	0.349	0.207	0.319	0.193	0.309	0.211	0.463	0.236	0.871	0.217
A_O	0.166	0.160	0.161	0.131	0.136	0.235	0.189	0.184	0.147	0.167
A_R	0.249	0.315	0.253	0.129	0.189	0.308	0.222	0.360	0.158	0.204
B_L	0.172	0.234	0.182	0.241	0.186	0.263	0.192	0.272	0.265	0.206
B_O	0.288	0.166	0.230	0.193	0.163	0.355	0.376	0.257	0.386	0.210
B_R	0.211	0.182	0.302	3.916	0.228	0.290	0.183	0.242	0.840	0.187
C_V	0.104	0.072	0.111	0.074	0.126	0.167	0.091	0.155	0.306	0.126
C_L	0.130	0.075	0.106	0.057	0.125	0.186	0.093	0.136	0.196	0.142
C_O	0.094	0.071	0.118	0.063	0.122	0.204	0.179	0.211	0.365	0.134
C_R	0.456	0.409	0.480	0.454	0.452	0.543	0.516	0.530	0.803	0.509
D_L	0.350	0.332	0.501	1.207	0.391	0.274	0.204	0.295	0.163	0.248
D_O	0.218	0.692	0.265	0.128	0.229	0.192	0.159	0.166	0.149	0.167
D_R	0.370	0.321	0.396	0.259	0.373	0.325	0.201	0.293	4.078	0.251
E_L	0.334	0.274	0.324	0.242	0.359	0.246	0.206	0.357	0.292	0.237
E_O	0.215	0.172	0.223	0.190	0.236	0.248	0.220	0.314	0.200	0.208
E_R	0.229	0.206	0.265	0.201	0.312	0.290	0.911	0.292	0.260	0.227
F_L	0.174	0.161	0.189	0.731	0.248	0.230	0.133	0.223	0.381	0.150
F_O	0.094	0.086	0.131	0.127	0.151	0.152	0.752	0.210	0.234	0.109
F_R	0.137	0.105	0.173	0.120	0.176	0.197	0.134	0.156	0.129	0.127
Mean	0.228	0.223	0.249	0.456	0.237	0.259	0.286	0.257	0.538	0.201

Table Appendix 10 Validation result for output K2 of the FM types.

	Gradient at point 2; K2				
	GPML	Kriging	LSSVM	Rational	RBF
A_L	0.860	0.974	0.881	0.813	0.892
A_O	0.212	0.242	0.234	0.294	0.220
A_R	0.466	0.364	0.475	3.557	0.454
B_L	0.292	0.244	0.303	0.572	0.300
B_O	0.154	0.564	0.160	0.332	0.155
B_R	0.205	0.196	0.291	0.280	0.245
C_V	0.159	0.221	0.159	0.193	0.143
C_L	0.150	0.142	0.156	0.139	0.138
C_O	0.170	0.101	0.166	0.184	0.116
C_R	0.261	0.256	0.260	0.357	0.262
D_L	0.572	0.668	0.545	0.740	0.500
D_O	0.336	0.534	0.326	0.281	0.271
D_R	0.574	0.490	0.418	0.559	0.450
E_L	0.417	0.439	0.528	0.549	0.437
E_O	0.236	0.232	0.247	0.310	0.253
E_R	0.435	1.101	0.473	0.338	0.370
F_L	0.353	0.250	0.475	4.964	0.332
F_O	0.152	0.169	0.162	0.214	0.149
F_R	0.245	0.223	0.273	0.153	0.205
Mean	0.329	0.390	0.344	0.780	0.310

A.6 Prediction Tool Validation

HRM

Table Appendix 11 Prediction tool validation of the HRM with the NRMSE.

Simulation:	1	2	3	4	5	6	7	8	9	10
weight ratio	0.86	1.41	1.39	0.91	1.15	1.05	1.21	1.39	1.53	0.92
impact velocity [kph]	23	55	22	49	31	52	31	33	44	26
impact angle [°]	-4	1	5	-6	7	11	14	19	-15	-17
position [mm]	1425	1678	1398	1499	1510	1891	1609	1457	1300	1250
A_L	0,798	0,884	0,506	0,803	0,412	0,278	0,055	0,846	-0,602	0,668
A_O	0,521	0,805	0,442	0,688	0,743	0,328	-0,167	0,690	0,098	0,769
A_R	0,761	0,949	0,698	0,873	0,539	0,411	0,163	0,879	-0,439	0,525
B_L	0,849	0,952	0,444	0,932	0,581	0,433	0,143	0,864	-0,197	0,312
B_O	0,582	0,863	0,435	0,846	0,626	0,579	0,341	0,738	-0,186	0,500
B_R	0,850	0,941	0,583	0,943	0,635	0,572	0,213	0,678	-0,145	0,542
C_A	0,723	0,923	0,633	0,741	0,636	0,552	0,192	0,399	0,051	-0,203
C_L	0,721	0,937	0,593	0,747	0,649	0,550	0,217	0,327	0,103	-0,286
C_O	0,691	0,937	0,675	0,707	0,717	0,569	0,277	0,367	0,124	-0,296
C_R	0,728	0,843	0,798	0,633	0,583	0,448	0,471	0,379	0,431	0,014
D_L	0,878	0,862	0,689	0,857	0,629	0,417	0,372	0,674	0,048	0,245
D_O	0,927	0,926	0,699	0,895	0,584	0,363	-0,021	0,810	-0,327	0,426
D_R	0,954	0,892	0,718	0,893	0,583	0,509	0,161	0,601	-0,135	0,022
E_L	0,931	0,902	0,684	0,948	0,591	0,554	0,169	0,690	-0,107	0,481
E_O	0,926	0,941	0,550	0,933	0,575	0,539	0,186	0,655	-0,241	0,422
E_R	0,864	0,951	0,668	0,867	0,640	0,595	0,195	0,638	-0,117	0,322
F_L	0,739	0,921	0,712	0,728	0,672	0,591	0,233	0,423	0,072	-0,170
F_O	0,735	0,923	0,712	0,712	0,720	0,578	0,254	0,393	0,143	-0,264
F_R	0,700	0,937	0,737	0,721	0,738	0,612	0,281	0,345	0,148	-0,337
mean	0,783	0,910	0,630	0,814	0,624	0,499	0,197	0,600	-0,067	0,194
variance	0,119	0,041	0,109	0,100	0,079	0,101	0,140	0,192	0,241	0,366

FRM

Table Appendix 12 Prediction tool validation of the FRM with the NRMSE.

Simulation:	1	2	3	4	5	6	7	8	9	10
weight ratio	0.86	1.41	1.39	0.91	1.15	1.05	1.21	1.39	1.53	0.92
impact velocity [kph]	23	55	22	49	31	52	31	33	44	26
impact angle [°]	-4	1	5	-6	7	11	14	19	-15	-17
position [mm]	1425	1678	1398	1499	1510	1891	1609	1457	1300	1250
A_L	0,623	0,851	0,494	0,838	0,624	0,616	0,535	-0,203	0,617	0,317
A_O	0,441	0,848	0,598	0,646	0,668	0,676	0,607	0,070	0,293	0,145
A_R	0,777	0,927	0,791	0,927	0,692	0,509	0,475	-0,192	0,664	0,581
B_L	0,879	0,906	0,710	0,900	0,897	0,437	0,505	0,016	0,726	0,632
B_O	0,577	0,832	0,528	0,836	0,835	0,599	0,560	0,004	0,596	0,529
B_R	0,854	0,917	0,688	0,844	0,840	0,506	0,487	0,132	0,761	0,348
C_A	0,799	0,924	0,603	0,864	0,724	0,638	0,373	0,163	0,420	0,185
C_L	0,768	0,931	0,535	0,810	0,714	0,623	0,390	0,129	0,199	0,429
C_O	0,737	0,931	0,590	0,756	0,755	0,633	0,458	0,206	0,244	0,351
C_R	0,788	0,832	0,882	0,658	0,770	0,615	0,669	0,457	0,456	-0,569
D_L	0,788	0,863	0,924	0,904	0,872	0,584	0,702	0,195	0,758	0,561
D_O	0,834	0,890	0,738	0,926	0,837	0,422	0,472	0,060	0,890	0,763
D_R	0,807	0,883	0,813	0,930	0,755	0,459	0,470	0,191	0,867	0,716
E_L	0,980	0,881	0,886	0,906	0,787	0,509	0,450	0,180	0,901	0,611
E_O	0,938	0,907	0,789	0,901	0,750	0,455	0,412	0,045	0,757	0,581
E_R	0,942	0,920	0,855	0,921	0,768	0,543	0,376	0,097	0,713	0,594
F_L	0,838	0,917	0,764	0,866	0,788	0,679	0,477	0,242	0,503	0,246
F_O	0,804	0,926	0,639	0,771	0,758	0,639	0,423	0,224	0,285	0,624
F_R	0,750	0,924	0,670	0,789	0,803	0,712	0,556	0,337	0,267	0,551
mean	0,785	0,895	0,710	0,842	0,770	0,571	0,495	0,124	0,575	0,431
variance	0,129	0,035	0,131	0,086	0,069	0,089	0,092	0,158	0,235	0,300

FM

Table Appendix 13 Prediction tool validation of the FM with the NRMSE.

Simulation:	1	2	3	4	5	6	7	8	9	10
weight ratio	0.86	1.41	1.39	0.91	1.15	1.05	1.21	1.39	1.53	0.92
impact velocity [kph]	23	55	22	49	31	52	31	33	44	26
impact angle [°]	-4	1	5	-6	7	11	14	19	-15	-17
position [mm]	1425	1678	1398	1499	1510	1891	1609	1457	1300	1250
A_L	0,685	0,786	0,550	0,742	0,559	0,690	0,540	-0,059	0,494	0,288
A_O	0,503	0,754	0,577	0,660	0,703	0,610	0,488	0,394	0,275	0,087
A_R	0,802	0,881	0,623	0,878	0,585	0,605	0,494	-0,074	0,538	0,573
B_L	0,768	0,873	0,547	0,947	0,721	0,525	0,463	0,095	0,687	0,620
B_O	0,572	0,734	0,399	0,776	0,694	0,667	0,518	0,100	0,598	0,426
B_R	0,874	0,869	0,566	0,944	0,692	0,518	0,475	0,210	0,665	0,249
C_A	0,722	0,856	0,432	0,773	0,585	0,588	0,360	0,215	0,415	0,434
C_L	0,684	0,860	0,377	0,736	0,586	0,580	0,359	0,169	0,583	0,334
C_O	0,456	0,898	0,488	0,542	0,567	0,644	0,498	0,433	0,558	0,403
C_R	0,751	0,811	0,680	0,588	0,475	0,587	0,459	0,378	0,390	0,125
D_L	0,714	0,753	0,697	0,791	0,702	0,670	0,713	0,466	0,789	0,718
D_O	0,757	0,826	0,665	0,830	0,653	0,485	0,364	0,156	0,818	0,726
D_R	0,730	0,765	0,717	0,843	0,673	0,497	0,526	0,377	0,794	0,675
E_L	0,827	0,801	0,690	0,916	0,663	0,534	0,511	0,331	0,741	0,433
E_O	0,840	0,858	0,534	0,938	0,613	0,494	0,455	0,121	0,652	0,395
E_R	0,553	0,881	0,639	0,655	0,569	0,628	0,530	0,378	0,686	0,364
F_L	0,679	0,835	0,566	0,723	0,631	0,622	0,434	0,264	0,428	0,453
F_O	0,751	0,837	0,542	0,700	0,627	0,588	0,366	0,222	0,563	0,742
F_R	0,497	0,807	0,515	0,516	0,559	0,657	0,528	0,484	0,541	0,612
mean	0,693	0,825	0,569	0,763	0,624	0,589	0,478	0,245	0,590	0,456
variance	0,122	0,049	0,100	0,132	0,066	0,064	0,084	0,166	0,148	0,195